UNIVERSITY OF ILORIN
FACULTY OF ENGINEERING AND TECHNOLOGY

1st FACULTY OF ENGINEERING AND TECHNOLOGY International Conference (FETiCON 2023)

Conference Proceedings

VOLUME II

THEME:

ADVANCES AND TECHNOLOGICAL INNOVATIONS IN NATION BUILDING AND ATTAINMENT OF SUSTAINABLE DEVELOPMENT GOALS

5th-7th June, 2023

NLNG Building, Faculty of Engineering & Technology,
University of Ilorin, Ilorin, Nigeria.

SPONSORS

PARTICIPANT COUNTRIES

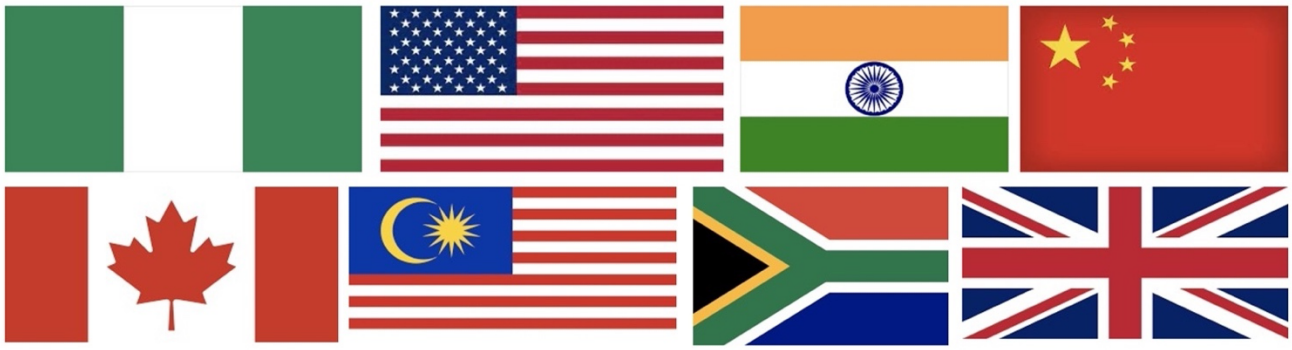

Table of Content

PAPER 14 – A SPACE VECTOR PULSE WIDTH MODULATED THREE PHASE INVERTER FOR AN IMPROVED SOLID-STATE TRANSFORMER DESIGN

Bashir Musa Umar[1], Jibril Yusuf [2], Boyi Jimoh[3], Abdullahi Bala Kunya[4], [5]Safia Aliyu, [6]Musa Mohammed

[1]Centre for Energy Research and Training, Ahmadu Bello University (A.B.U), Zaria Nigeria
[2, 3, & 4] Department of Electrical Engineering, A.B. U. Zaria, Nigeria

[*]Email: mambilla2000@yahoo.com

ABSTRACT
A Space Vector Pulse Width Modulation (SVPWM) technique is used for the implementation of a three phase DC-AC Voltage Source Converter (VSC). The VSC is used in design of an improved Solid-State Transformer (SST). Consequently, this paper discusses concept and operation of SVPWM as well as implementation of the technique to achieve a desired objective. VSC has been used to enable supply of variable voltages and frequency to AC drives and other areas of applications in the electric network. Several forms Pulse Width Modulation (PWM) Techniques to obtain variable voltage and frequency exist. Two of these PWM techniques are commonly used in the implementation of the VSC: SVPWM and Carrier-based PWM. Trend of use of SVPWM in the design of VSC is on increase due to its better utilization of DC bus and easier digital realization. Therefore, in this paper concept and implementation of SVPWM for VSC have been elucidated with the aid of MATLAB/Simulink environment. An LCL filter has been used in the design with the view to further mitigate harmonics. Performance of the VSC is evaluated in terms of Total Harmonic Distortion (THD).
KEYWORDS: *THD, SST SVPWM, VSC, LCL filter.*

1. INTRODUCTION

Voltage Source Converters (VSCs) are not mass-produced product. Therefore, they should be specifically designed for the applications they are used for. A VSC has been employing the use of Space Vector Pulse Width Modulation (SVPWM) scheme in its design this is to enable obtaining variable voltages and frequency for use in AC drives and other relevant areas of application. In this paper, a VSC is designed for implementation of an improved Solid-State Transformer (SST). SST has been investigated in recent years to either replace or work hand-in-hand with the conventional Low Frequency Transformer (LFT) (Ismail et al., 2022; Nondy & Nondy, 2021; Saju et al., 2020; Zhang et al., 2019). This is largely due to some advantages the SST posses relative to the LFT (Abu-Siada et al., 2018; Hannan et al., 2020; Londero et al., 2019; Mollik et al., 2022; Saju et al., 2020). These advantages include: It corrects Power Factor (PF); it can be used in both AC and DC systems; it controls both active and reactive power; it enables online communication in the event of fault and controls it etc. (Shafei et al., 2019; Tahir et al., 2019; Umar et al., 2020, 2021; Vaca-Urbano et al., 2020). However, the SST suffers some draw-backs which are: Less efficiency and reliability while compared to the LFT (Umar et al., 2020). In order to enhance efficiency of SST a designed SST is improved. To improve the SST, a SVPWM and an LCL filter are used in its design. The SVPWM is used particularly in the design of the DC-AC converter at the output stage of the SST. Consequently, the converter performance has greatly improved due to reduction of the THD and hence improves the performance of the SST. This paper describes VSC based on SVPWM; it further discusses THD obtained from the VSC. Schematic of SST is as shown in Fig.1.

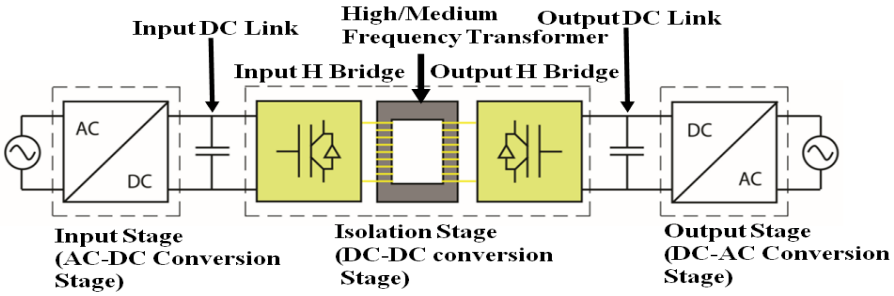

Fig. 1: Schematic of SST (Gajowik et al., 2017)

2. THEORETICAL ANALYSIS

2.1 Voltage source and current source converters

Active rectifiers employing use of VSC or CSC stand advantage both for traditional solutions such as the thyristor and for newer ones such as a chopper, due to the following (Banumathy & Veeraraghavalu, 2018):

i. Reduced number of power devices
ii. Capability of grid current control
iii. power factor correction

Voltage-sourced converter is a self-commuted converter that generates ac voltage from a dc voltage. VSC is often referred to as an inverter, even though it has the capable of bidirectional power flow. With a VSC, frequency of the output voltage, phase angle, and the magnitude can be controlled (Khan et al., 2021). In this type of converters the dc side voltage always has one polarity, and the power flow reversal takes place through reversal of dc current polarity. On DC side the voltage is supported by a capacitor. This capacitor should be capable to handle a sustained charge/discharge current that accompanies the switching sequence of the converter valves and shifts in phase angle of the switching valves without significant change in the dc voltage. The VSC connects HVAC and HVDC systems using devices suitable for high power electronic applications, such as MOSFETs and IGBTs (Khan et al., 2016). On the other hand in the CSC an inductor maintains the DC current constant. Schematic of VSC and CSC is as shown in Fig. 2.

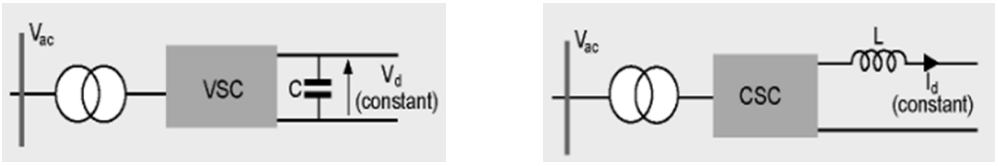

(i) VSC (ii) CSC

Fig. 2: Schematics of (i) VSC and (ii) CSC

The use of the VSC in the design of the converter is due to its: (i) higher Voltage handling capability, (ii) High power rating, (iii) Better output voltage waveform, (iv) and less electromagnetic interference (Taylor et al., 2013).

VSC is usually connected to the power system at th Point of Common Coupling (PCC) through phase reactors, which also serve as filter inductors to further mitigate harmonics (Nandhini & Sivaprakasam, 2020).

2.2 Principle of SVPWM

A three-phase system can be represented by two-phase system. The two-phase quantities are referred to as vector. Vectors are defined in a complex plane since they allow to use the property of vectorial rotation. The space vector modulation is meant to be a three-phase sinusoidal waveform with respect to time on the three axes that are displaced in time with respect to each other by 120° yielding a constant amplitude space vector that rotates at a constant speed. In the case of SVPWM technique, the two-level DC-AC converter contains two zero vectors and six active vectors to generate the reference voltage which gets sampled once for every sub-cycle T_s. The SVPWM employs the switching sequence which divides the zero vector time equally for the two zero states in every sub-cycle. The maximum control voltage, V_c obtained using SVPWM is given by the expression

$$V_c = \frac{V_{DC}}{\sqrt{3}} \tag{1}$$

Reference voltage V_{REF} in SVPWM is given as follows:

$$V_{REF} = \sqrt{V_d^2 + V_q^2} \tag{2}$$

Where the two-phase quantities, V_d and V_q in (2) are given as in the following expressions respectively.

$$V_d = \frac{2}{3}\left[V_{an} - {}^1\!/_2\,(V_{bn} - V_{cn})\right] \tag{3}$$

$$V_q = \frac{2}{3}\left[\frac{\sqrt{3}}{2}(V_{bn} - V_{cn})\right] \quad (4)$$

The angle between the two-phase quantities is calculated using the expression:

$$\theta = tan\sqrt{V_d / V_q} \quad (5)$$

In SVPWM, the reference vector V_{REF} is synthesized by two active vectors and two zero vectors as shown Fig. 7. The Fig. 7 shows the voltage vectors of two-level DC-AC converter with six sectors 1 to 6. For example in Sector I, V_{REF} is realized by applying vector V_1' for an appropriate duration of T_1, vector V_2' for an appropriate duration of T_2 and V_0 for remaining duration in a sub-cycle of T_s, based on volt-second balance principle.

$$V_{REF}T_s = V_1T_1 + V_2T_2 + V_0T_0 \quad (6)$$

$$T_s = T_1 + T_2 + T_0 \quad (7)$$

Where,
VREF is reference vector, Ts is duration of sub cycle, T1 and T2 are dwell times active vectors and T0 is dwell time of zero vectors.

The dwell times T0, T1 and T2 are respectively calculated using the expressions,

$$T_0 = T_s - (T_1 + T_2) \quad (8)$$

$$T_1 = \frac{V_{REF}}{V_{DC}} \frac{Sin(60-\theta)}{Sin60} T_s \quad (9)$$

$$T_2 = \frac{V_{REF}}{V_{DC}} Sin \frac{\theta}{Sin(60)} T_s \quad (10)$$

2.3 LCL filter

An LCL filter is used in the design of the DC-AC converter to mitigate harmonics. The use of LCL filters becomes attractive due to their reduced component dimensions. The parameters of the designed improved SST in which the DC-AC converter is used are as shown in Table 2.

Table 2: Parameters specifications for the Designed improved SST (Tahir et al., 2019)

SNo	parameter	Value
1	Rating, S	200kVA
2	Input AC voltage, V_{1RMS}	11kV
3	Output AC voltage, V_{2RMS}	Variable
4	Output DC voltage, V_{2DC}	500V
5	Grid Frequency (F_o)	50Hz

Parameters of the filter are calculated as follows: The capacitance of the filter capacitor, C_f was calculated to be 46mF using the expression (Dursun & Dosoglu, 2018) :

$$C_{f2} = \frac{0.05 \cdot P_0}{V_{1phRMS} \cdot \omega_g} \quad (11)$$

Unity power factor was achieved therefore, Real power (P) = Apparent power (S). P_o which was a per phase power output of the SST was obtained by dividing the rated power of the SST in Table 3.1 by three (3). Also the phase

voltage V_{ph} was obtained by dividing V_{1RMS} in Table 2 by square root of 3. ω_g is the angular frequency at the grid side given as:

$$\omega_g = 2\pi F_o \tag{12}$$

Where F_o is the grid frequency.

Switching frequency, F_{sw} was selected to be 25kH. The resonance frequency which is the natural frequency where a medium vibrates at the highest amplitude denoted by 'F_r' was calculated by dividing the F_{sw} by 10. F_r was obtained to be 2.5 kHz.

The phase grid current i_{gph} was calculated to be 10.49A using the expression:

$$i_{gphRMS} = \frac{P_o}{V_{1phRMS}} \tag{13}$$

Peak I_{gph} that is $i_{gphp}$was obtained by multiplying I_{gphRMS} by square root of 2. It was obtained to be 14.84A.

The load resistance, R_L was calculated to be 605.21Ω by substituting V_{1php} and i_{gphp} in the following expression.

$$R_L = \frac{V_{1php}}{i_{gphp}} \tag{14}$$

Therefore, R_L value of 700Ω was considered for the design.

The $i_{gphp\ (sw)}$ that is the i_{gphp} during switching was calculated by multiplying i_{gphp} by the allowable percentage of 0.3 (0.3%). $i_{gphp\ (sw)}$ was calculated to be 0.044A.

The phase input voltage during switching [$V_{1phRMS\ (sw)}$] was calculated to be 5.72kV by multiplying V_{1phRMS} by 90% allowable voltage during switching.

Minimum inductance of the filter inductor (L_{min}) was calculated using the expression (Dursun & Dosoglu, 2018):

$$L_{min} = \frac{V_{1phRMS(sw)}}{i_{gphp\ (sw)} \cdot \omega_{sw}\ (1-\frac{\omega_r^2}{\omega_{sw}^2})} \tag{15}$$

ω_{sw} and ω_r were calculated as 157. 08 kHz and 15.71 kHz respectively using the expressions:

$$\omega_{sw} = 2\pi F_{sw} \tag{16}$$

$$\omega_r = 2\pi F_r \tag{17}$$

The L_{min} was obtained to be 0.84H. Therefore, $L_1 = L_2 = L_{min}/2$ which was equal to 420mH. Therefore, 500mH was considered for the design of the converter.

The maximum voltage drop at the filter inductor V_{Lmax} was calculated by multiplying V_{1php} by 20%. V_{Lmax} was obtained as 1796.29V.

The Quality factor, Q of the filter was calculated using the expression:

$$Q = R_L\sqrt{\frac{C}{L}} \tag{18}$$

However, because the designed filter was an LCL filter the resultant inductance (L_r) of the filter was calculated using the expression:

$$L_r = \frac{L_1^2}{2L_1} \tag{19}$$

L_r was calculated to be 0.297H. 300mH was used. And L was equal to L_r in all the related equations.

Therefore, the Quality factor, Q_o was obtained to be 6460.70. The Damping factor ξ_o was calculated to be 7.73 using the following expression.

$$\xi_o = \frac{1}{2Q} \tag{20}$$

The cut-off frequency was calculated to be 51.93Hz. The obtained parameters of the filter were as indicated in Table 3. Schematic of the designed LCL filter was as shown in Fig. 3.

Table 3: Parameters of the Designed three phase input LCL Filter

SN	Parameter	Calculated value
1	Load resistance, R_L	700Ω
2	Capacitance, C_{f2}	23mF
3	Inductance, L_{o1}	500mH
4	Cut-off frequency, F_{co}	51.93Hz
5	Quality factor, Q_o	6460.70
6	Damping factor, ξ_o	7.73

Designed LCL filter schematic of per phase model is as shown in Fig. 3.

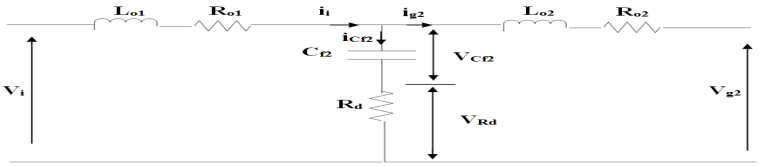

Fig. 3: Designed LCL filter per-phase model

Considering Fig. 3, the per phase state space model of the designed LCL is derived as follows:

$$\begin{cases} \dfrac{d_{i_i}}{dt} = \dfrac{1}{L_{o1}}\left[v_i - v_{c_{f2}} - R_d\left(i_i - i_{g2}\right) - R_{o1}i_i\right] \\ \dfrac{d_{g2}}{dt} = \dfrac{1}{L_{o2}}\left[v_{v_{C_{f2}}} + R_d\left(i_i - i_{g2}\right) - v_{g2} - R_{o2}i_{g2}\right] \\ \dfrac{d_{v_{c_{f2}}}}{dt} = \dfrac{i_i - i_{g2}}{C_{f2}} \end{cases} \tag{21}$$

Therefore, the state space equation of the designed three phase output LCL filter per-phase model is as follows:

$$\begin{bmatrix} \frac{d_{i_i}}{dt} \\ \frac{d_{i_{g2}}}{dt} \\ \frac{d_{v_{c_{f2}}}}{dt} \end{bmatrix} = \begin{bmatrix} -\frac{R_{o1}+R_d}{L_{o1}} & -\frac{R_d}{L_{o1}} & -\frac{1}{L_{o1}} \\ \frac{R_d}{L_{o2}} & -\frac{R_{o2}+R_d}{L_{o2}} & \frac{1}{L_{o2}} \\ \frac{1}{C_{f2}} & -\frac{1}{C_{f2}} & 0 \end{bmatrix} \begin{bmatrix} i_i \\ i_{g2} \\ v_{c_{f2}} \end{bmatrix} + \begin{bmatrix} \frac{1}{L_{o1}} & 0 \\ 0 & -\frac{1}{L_{o2}} \\ 0 & 0 \end{bmatrix} \begin{bmatrix} v_i \\ v_{g2} \end{bmatrix} \tag{22}$$

Therefore, the state space equation of designed three phase LCL filter model is derived considering Fig.4 as follows:

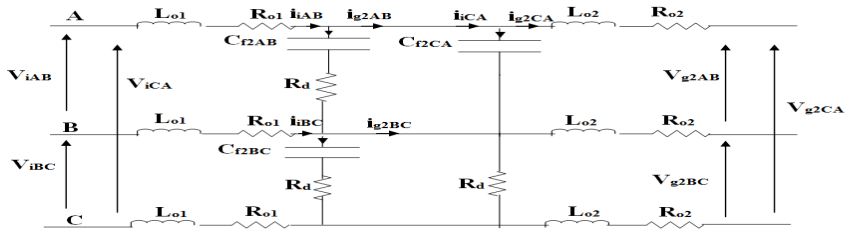

Fig. 4: Designed three phase output LCL filter model

where $i_{g2} = [i_{g2AB}\ i_{g2BC}\ i_{g2CA}]^T$, $v_{g2} = [v_{g2AB}\ v_{g2BC}\ v_{g2CA}]^T$, $v_{cf2} = [V_{Cf2AB}\ V_{Cf2BC}\ V_{Cf2CA}]^T$, $i_i = [i_{iAB}\ i_{iBC}\ i_{iCA}]^T$, and $v_i = [V_{iAB}\ V_{iBC}\ V_{iCA}]^T$.

$$\begin{bmatrix} \frac{d_{i_i}}{dt} \\ \frac{d_{g2}}{dt} \\ \frac{d_{v_{cf2}}}{dt} \end{bmatrix} = \begin{bmatrix} -\frac{R_{o1}+R_d}{L_{o1}}I_{3X3} & -\frac{R_d}{L_{o1}}I_{3X3} & -\frac{1}{L_{o1}}I_{3X3} \\ \frac{R_d}{L_{o2}}I_{3X3} & -\frac{R_{o2}+R_d}{L_{o2}}I_{3X3} & \frac{1}{L_{o2}}I_{3X3} \\ \frac{1}{3C_{f2}}I_{3X3} & -\frac{1}{3C_{f2}}I_{3X3} & 0I_{3X3} \end{bmatrix}_{9X9} \begin{bmatrix} i_i \\ i_{g2} \\ v_{c_{f2}} \end{bmatrix}_{9X1} + \begin{bmatrix} \frac{1}{L_{o1}}I_{3X3} \\ -\frac{1}{L_{o2}}I_{3X3} \\ 0_{3X3} \end{bmatrix}_{9X1} \begin{bmatrix} v_{g2} \\ v_i \end{bmatrix}_{9X1} \quad (23)$$

Simulink model of the designed three phase DC-AC converter is as shown in Fig. 5. Schematic of the designed DC-AC converter model is as shown in Fig. 6.

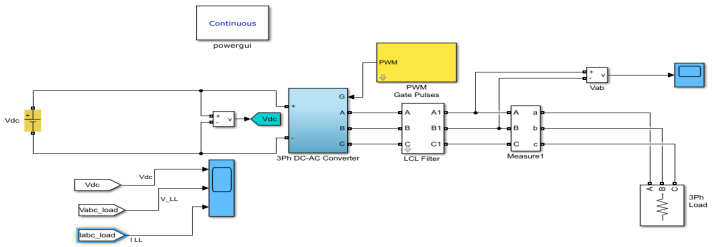

Fig. 5: Simulink model of the designed DC-AC converter

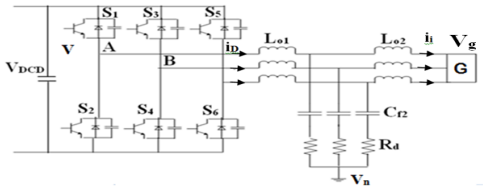

Fig. 6: Schematic of the designed Three Phase DC-AC converter for analysis

Vector representation of the SVPWM is presented in Fig.7. The active states divide equally the space vector plane into six sectors as shown in Fig. 7. The switching states of the six active and two null vectors are as presented in Table 4.

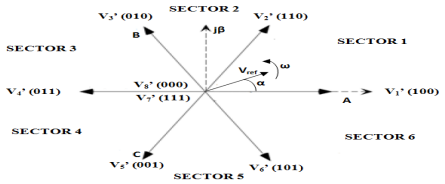

Fig. 7: Vector representation of the SVPWM

Table 4: Switching states corresponding to space vectors

SN	Switching gate			Line-Neutral Voltage			Line-Line Voltage		
	A	B	C	V_{AN}	V_{BN}	V_{CN}	V_{AB}	V_{BC}	V_{CA}
1	0	0	0	0	0	0	0	0	0
2	1	0	0	$2/3V_{DC}$	$-1/3V_{DC}$	$-2/3V_{DC}$	V_{DC}	0	$-V_{DC}$
3	1	1	0	$1/3V_{DC}$	$1/3V_{DC}$	$-2/3V_{DC}$	0	V_{DC}	$-V_{DC}$
4	0	1	0	$-1/3V_{DC}$	$2/3V_{DC}$	$-1/3V_{DC}$	$-V_{DC}$	V_{DC}	0
5	0	1	1	$-2/3V_{DC}$	$1/3V_{DC}$	$1/3V_{DC}$	$-V_{DC}$	0	V_{DC}

6	0	0	1	$-1/3V_{DC}$	$-1/3V_{DC}$	$2/3V_{DC}$	0	$-V_{DC}$	V_{DC}
7	1	0	1	$1/3V_{DC}$	$-2/3V_{DC}$	$1/3V_{DC}$	V_{DC}	$-V_{DC}$	0
8	1	1	1	0	0	0	0	0	0

A rotating space vector V (t) in complex rotation is given by:

$$V(t) = \frac{2}{3}\left[V_A + V_B e^{j\left(\frac{2}{3}\right)\pi} + V_C e^{-j\left(\frac{2}{3}\right)\pi}\right] \quad (24)$$

Therefore, considering (14), the output phase voltage in switching state 100 is given as:

$$V_A(t) = \frac{2}{3}V_{DC} \quad (25)$$

$$V_B(t) = -\frac{1}{3}V_{DC} \quad (26)$$

$$U_C(t) = -\frac{1}{3}V_{DC} \quad (27)$$

Therefore:

$$V_1' = \frac{2}{3}\left[\frac{2}{3}V_{DC} - \frac{1}{3}V_{DC}e^{j\left(\frac{2}{3}\right)\pi} - \frac{1}{3}V_{DC}e^{-j\left(\frac{2}{3}\right)\pi}\right] \quad (28)$$

$$\Rightarrow V_1' = \frac{2}{3}V_{DC}e^{j0} = V_1' = \frac{2}{3}V_{DC} \quad (29)$$

Therefore, for all the six active vectors, the voltage is calculated using the expression:

$$V_N' = \frac{2}{3}V_{DC}e^{j(N-1)\frac{\pi}{3}} \quad (30)$$

For N = 1, 2, 3…6

Considering Fig. 6 the State space equation of the designed DC-AC converter was derived as thus,

$$\begin{cases} L_{o1}\frac{di_D}{dt} = V_{DCD} + V - V_{C_{f2}} - V_{R_d} - V_n \\ C_{f2}\frac{dV_{C_{f2}}}{dt} = i_D - i_g \\ L_{o2}\frac{di_g}{dt} = V_{C_{f2}} + V_{R_d} + (V_n - V'_n)1 - V_g \end{cases} \quad (31)$$

Where,

i_D, i_g, V_{Cf2}, and V_g, were DC-AC converter side current voltage, grid side current vector, outfut LCL filter capacitor voltage vector and grid voltage vector respectively and were given as:

$i_D = [i_A \;\; i_B \;\; i_C]$, $ig = [i_{gA} \;\; i_{gB} \;\; i_{bC}]$, $V_{cf2} = V_{cf2A} \;\; V_{cf2B} \;\; V_{cf2C}]$ and $V_g = [V_{gA} \;\; V_{gB} \;\; V_{gC}]$.

Also,

V was the Control signal vector given as

$V = [V_A \;\; V_B \;\; V_C]$, V_n and V'_n were voltages at the neutral points and 1 was a column vector defined as [1 1 1].

Considering (31), the neutral point voltages were derived as thus,

$$V_n = \frac{V_{DCD}}{3}(V_A + V_B + V_C) - \frac{1}{3}\left(V_{Cf2A} + V_{Cf2B} + V_{Cf2C}\right) \quad (32)$$

$$V_n' = \frac{V_{DCD}}{3}(V_A + V_B + V_C) - \frac{1}{3}\left(V_{gA} + V_{gB} + V_{gC}\right) \quad (33)$$

Assuming that the grid voltages are balanced (i.e $V_{Cf2A} + V_{Cf2B} + V_{Cf2C} = 0$ and $V_{gA} + V_{gB} + V_{gC} = 0$), therefore, the expression for the neutral voltages were reduced to:

$$V_n = V_n' = \frac{V_{DCD}}{3}(V_A + V_B + V_C) \tag{34}$$

The expression for the three phase DC-AC converter became:

$$\begin{cases} L_{o1}\frac{di_D}{dt} = V_{DCD} + V - V_{C_{f2}} - V_{R_d} - V_n \\ C_{f2}\frac{dV_{C_{f2}}}{dt} = i_D - i_g \\ L_{o2}\frac{di_g}{dt} = V_{C_{f2}} + V_{R_d} - V_g \end{cases} \tag{35}$$

(35) can be re-written as a discrete state-space model. Thus,

$$x_i(k+1) = Ax_i(k) + Bu_1(k) + DV_1(k) + EV_n(k) \tag{36}$$

$$y_i(k) = Hx_i(k) \tag{37}$$

Where,

$x_i(k) = (i_{Ai} \quad u_i \quad i_{gi})$ is the state- space vector, H is the output matrix defined as H = (1 0 0)

3. MATERIALS AND METHODS/METHODOLOGY/EXPERIMENTAL PROCEDURE

MATLAB 2022Ra environment was used in the design of the DC-AC Simulink model. The FFT analysis was carried out using the same software. The DC-AC was design to compose of LCL filter which was mathematical designed as shown earlier, the Converter itself. IGBTs were used to in the design of the active converter. SVPWM was used to control the signal supplied to the power electronics switches to align with the input and output signals requirements.

4. RESULTS AND DISCUSSION

The Simulink model of the designed three phase DC-AC converter is simulated on MATLAB environment.
The line to line output voltage of the DC-AC converter was 545V as presented in Fig. 8. Also, phase output voltage of the designed DC-AC converter was found to be 324V as shown in Fig. 9. In both waveforms, nearly pure sinusoidal waveforms were achieved.

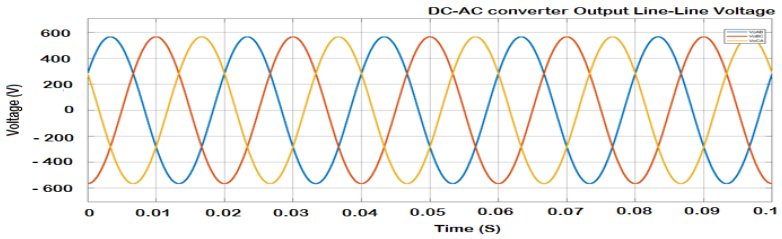

Fig. 8: Output line to line voltage of the DC-AC converter

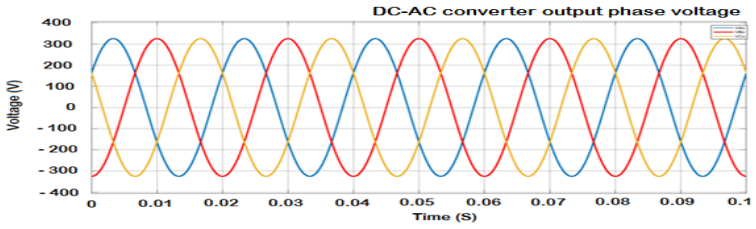

Fig. 9: Output phase voltage of the DC-AC converter

THD of the DC-AC converter was obtained to be 1.23% as presented in Fig.10. This value was well within the IEEE 519, 2012 THD standard limits.

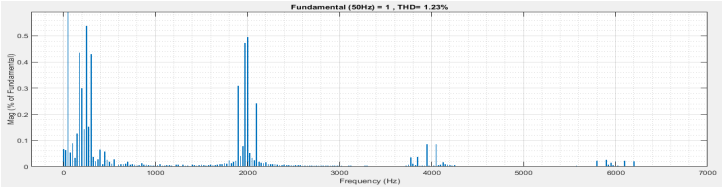

Fig. 10: DC-AC converter FFT analysis result

5. CONCLUSION

A three phase DC-AC active converter has been designed. The converter design was achieved with a reduced THD that corroborate to the IEEE 519, 2012 THD standard limit. The achievement was as a result of use of three phase LCL filter to further mitigate harmonics and SVPWM that provided more efficient control.

ACKNOWLEDGEMENT

The Authors acknowledged the grant offered to them by Sanaa da Ilimi Foundation to undertake the whole work on improvement of an SST.

REFERENCES

Abu-Siada, A., Budiri, J., & Abdou, A. (2018). Solid State Transformers Topologies, Controllers, and Applications: State-of-the-Art Literature Review. *Electronics*, *7*(298), 1–18. https://doi.org/10.3390/electronics7110298

Banumathy, J. R., & Veeraraghavalu, R. (2018). High Frequency Transformer Design and Optimization using Bio-inspired Algorithms. *Applied Artificial Intelligence*, *00*(00), 1–20. https://doi.org/10.1080/08839514.2018.1506969

Dursun, M., & Dosoglu, M. K. (2018). LCL Filter Design for Grid Connected Three-Phase Inverter. *ISMSIT 2018 - 2nd International Symposium on Multidisciplinary Studies and Innovative Technologies, Proceedings*, *3*, 2018–2021. https://doi.org/10.1109/ISMSIT.2018.8567054

Gajowik, T., Sobol, C., Stynski, S., & Malinowski, M. (2017). Post-fault operation of hybrid DC-DC converter for Solid-State Transformer. *Proceedings IECON 2017 - 43rd Annual Conference of the IEEE Industrial Electronics Society*, *2017-Janua*, 5373–5379. https://doi.org/10.1109/IECON.2017.8216931

Hannan, M. A., Ker, P. J., Lipu, M. S. H., Choi, Z. H., Rahman, M. S. A., Muttaqi, K. M., & Blaabjerg, F. (2020). State of the art of solid-state transformers: Advanced topologies, implementation issues, recent progress and improvements. *IEEE Access*, *8*, 19113–19132. https://doi.org/10.1109/ACCESS.2020.2967345

Ismail, A., Abdel-Majeed, M. S., Metwly, M. Y., Abdel-Khalik, A. S., Hamad, M. S., Ahmed, S., Hamdan, E., & Elmalhy, N. A. (2022). Solid-State Transformer-Based DC Power Distribution Network for Shipboard Applications. *Applied Sciences*, *12*(4), 2001. https://doi.org/10.3390/app12042001

Khan, A. A., Cha, H., & Kim, H. (2016). Double Step-Down AC-AC Converters with High Frequency Isolation. *2016 IEEE 8th International Power Electronics and Motion Control Conference (IPEMC-ECCE Asia)*, 1–6.

Khan, S., Rahman, K., Tariq, M., Hameed, S., & Basem Alamri Babu, T. S. (2021). Solid-State Transformers: Fundamentals, Topologies, Applications, and Future Challenges. *Sustainability*, *14*(319), 1–20. https://doi.org/10.1016/j.amc.2004.08.041

Londero, R. P., De Mello, A. P. C., & Da Silva, G. S. (2019). Comparison between conventional and solid state transformers in smart distribution grids. *2019 IEEE PES Conference on Innovative Smart Grid Technologies, ISGT Latin America 2019*, 1–6. https://doi.org/10.1109/ISGT-LA.2019.8895327

Mollik, M. S., Hannan, M. A., Reza, M. S., Abd Rahman, M. S., Lipu, M. S. H., Ker, P. J., Mansor, M., & Muttaqi, K. M. (2022). The Advancement of Solid-State Transformer Technology and Its Operation and Control with Power Grids: A Review. *Electronics (Switzerland)*, *11*(17). https://doi.org/10.3390/electronics11172648

Nandhini, E., & Sivaprakasam, A. (2020). A Review of Various Control Strategies Based on Space Vector Pulse Width Modulation for the Voltage Source Inverter. *IETE Journal of Research*, *0*(0), 1–15. https://doi.org/10.1080/03772063.2020.1754935

Nondy, R. K., & Nondy, P. (2021). *Solid State Transformer (SST) For Smart Application in Power System*. *x*.

Saju, N., Jegathesan, V., & Aiswarya, K. P. (2020). Solid state transformers: An emerging trend in power quality improvement. *International Journal of Engineering Research and Technology*, *13*(5), 900–908.

Shafei, A. El, Ozdemir, S., Altin, N., Jean-pierre, G., & Nasiri, A. (2019). A High Power High Frequency Transformer Design for Solid State Transformer Applications. *8th International Conference on Renewable Energy Research and Applications*, *May 2021*, 904–909. https://doi.org/10.1109/ICRERA47325.2019.8996515

Tahir, U., Abbas, G., Glavan, D. O., Balas, V. E., Farooq, U., Balas, M. M., Raza, A., Asad, M. U., & Gu, J. (2019). Design of three phase solid state transformer deployed within multi-stage power switching converters. *Applied Sciences (Switzerland)*, *9*(17). https://doi.org/10.3390/app9173545

Taylor, P., Liserre, M., Blaabjerg, F., & Aquila, A. D. (n.d.). *Step-by-step design procedure for a grid-connected three-phase PWM voltage source converter*. *March 2013*, 37–41. https://doi.org/10.1080/00207210412331306186

Umar, B. M., Jibril, Y., Boyi, J., Kunya, Abdullahi Bala Maiwada, Yusuf Abubakar Aliyu, S., & Mohammed, M. (2021). Review of Solid-State Transformer in Electric Power System. *Nternational Conference on Electrical Engineering Applications (ICEEA'2020)*, 274–278.

Umar, B. M., Yusf, J., Jimoh, B., Kunya, A. B., Maiwada, Y. A., Aliyu, S., & Mohammed, M. (2020). Glance Into Solid-State Transformer Technology : A Mirror For Possible Research Areas. *Journal of Applied Materials and Technology*, *2*(1), 1–13.

Vaca-Urbano, F., S. Alvarez-Alvarado, M., A. Recalde, A., & Moncayo-Rea, F. (2020). Solid-State Transformer for Energy Efficiency Enhancement. In *Research Trends and Challenges in Smart Grids*. IntechOpen. https://doi.org/10.5772/intechopen.84345

Zhang, J., Liu, J., Zhong, S., Yang, J., Zhao, N., & Zheng, T. Q. (2019). A Power Electronic Traction Transformer Configuration with Low-Voltage IGBTs for Onboard Traction Application. *IEEE Transactions on Power Electronics*, *34*(9), 8453–8467. https://doi.org/10.1109/TPEL.2018.2889107

PAPER 18 – INFLUENCE OF STATOR SLOT NUMBER ON THE PERFORMANCE OF AN ELECTRICAL MACHINE

C.C. Awah[1*]

[1]Department of Electrical and Electronic Engineering, Michael Okpara University of Agriculture, Umudike, Nigeria.
[*]Email: ccawah@ieee.org

ABSTRACT
The influence of stator slot number on the performance of a given double stator permanent magnet machine was investigated in this study. The considered permanent magnet (PM) machines are classified as: Type I and Type II, having 6 stator slots and 12 stator slots, respectively. Finite element analysis (FEA) is adopted in the result estimations. It is observed that an increase in the number of stator slots result to enhanced machine performances such as: higher induced voltage and torque outputs. Torque pulsations in the machine are significantly reduced by doubling the slot number; this reduction is in the ratio of 6:1, for the Type I and Type II machines. Nevertheless, Type I machine has higher machine efficiency at low operating speed than its Type II counterpart. Additionally, Type I machine exhibits superior speed range than Type II machine. The investigated machine types would be suitable in low speed direct-drive applications. By doubling the slot number of the analyzed machine from six (6) to twelve (12), its output torque and induced voltage increased by 34.5 % and 31.7 %, respectively, at rated speed and load conditions. Consequently, output power of the machine also increased by 36.4 %.

KEYWORDS: Concentrated windings, Double stator, Efficiency, Loss, Slot number, Torque.

1. INTRODUCTION

The stator slot number of a given electrical machine is vital in predicting the output performance of the machine. Wang *et al*, (2008) clearly stated that slot number and pole number grouping of an electric machine would greatly influence its output performance, particularly the resulting winding factors. If the slot number of a given permanent magnet (PM) machine is doubled; then, the resulting magnetomotive force (MMF), electromotive force (EMF) and average torque values of the machine would be enhanced correspondingly, as established in (Wang *et al*, 2014a). In contrast, the resulting outcome of doubling the stator slot number of a particular machine would be a function of the machine's level of flux-leakage and fringing effects, coupled with the kind of machine configuration (Zhang *et al*, 2009). The impact level of this slot number difference on the overall electromagnetic performance of a given double stator permanent magnet (DSPM) machine is considered and presented in this current study.

The studies in Xu *et al*, (2010) and Zhang *et al*, (2012) reveal that if the ratio of pole to slot number of flux-switching permanent magnet (FSPM) machine is decreased by half i.e. a concurrent reduction in both the machine's pole and slot number; then, there would be a corresponding higher average torque, lower torque ripple, enlarged magnetic flux density, improved efficiency and increased self-inductance value; however, with consequent reduction on the machine's field-weakening potential. Additionally, the generated flux-linkage value of the machine with reduced pole to slot ratio would be significantly increased, as presented in Tang *et al*, (2013).

The investigated machine types in this current study have double stator and double air gap structures, owing to the usual merits of double stator electrical machines over the single stator ones, as highlighted and proved in Jiang et al, (2021) and Zhao et al, (2022). These numerous advantages of double airgap and double stator machine are re-emphasized in Ding et al, (2023). Nevertheless, the investigation in Ullah et al, (2022) reveal that double rotor machines can outperform its double stator equivalents; however, with increased manufacturing complexity and higher electromagnetic losses. Moreover, Su et al, (2018) showed that when magnets are mounted on the rotor of FSPM machine, it would produce superior electromagnetic performance(s), in addition to better thermal management capacity (Zhang et al, 2009) than its equivalent stator mounted magnet counterpart; though, with inferior overall machine efficiency.

Wang *et al*, (2014b) proved that the iron loss value of a PM machine would increase if its slot number is doubled; however, with a resultant decrease in eddy loss value. The obtained loss results in Wang *et al*, (2014b) are in consonant

with the predicted loss values in this present investigation, shown in the last part of Section 3 of this study. Furthermore, the amount of unbalanced magnetic force on the rotor of a given machine would also largely depend on its slot and pole number arrangement, as proved in Zhu *et al*, (2013).

Essentially, effect of doubling the stator slot number on the overall performance of a given double stator electric machine is analyzed and presented in this current investigation. The background of study with its relevant literature is presented in Introduction, the adopted method and materials are presented in Section 2 of this study, the predicted results and conclusion are provided in Section 3 and Section 4, respectively.

2. MATERIALS AND METHODS

Predicted results in this study are estimated using finite element analysis (FEA) approach; MAXWELL-2D software is applied in this analysis. The considered machines are classified as: Type I and Type II, having six (6) stator slots and twelve (12) stator slots, respectively with each in either of the two stator parts (inner and outer stators). The coils of both inner and outer stator slots are joined in series for improved overall performance, in each of the machine categories. The compared machine types are kinds of FSPM machine; with double stator structures. The magnets are mounted in the inner stators in such a way, that the closest magnets would always have opposite polarities to each other. The implemented models of the compared machine types are shown in Figure 1. Similarly, the basic machine parameters and employed materials are listed in Table 1.

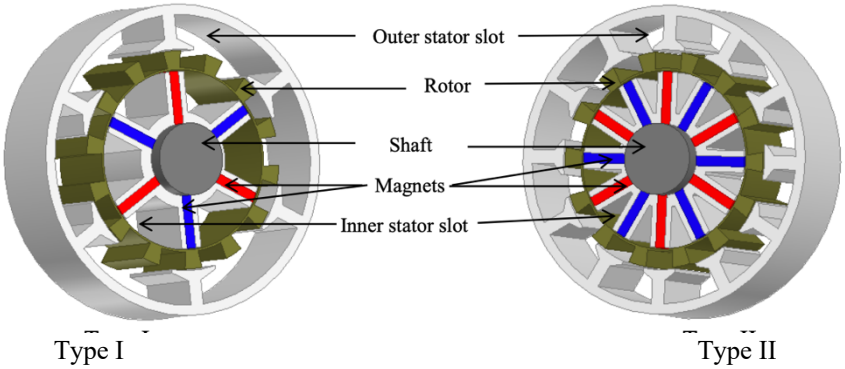

Figure 1: Compared machine models

Table 1: Basic machine parameters and values

Parameter	Value	
Machine Type	Type I	Type II
Inner stator slot number	6	12
Outer stator slot number	6	12
Number of coils per phase	2	4
Number of turns per coil	36	18
Spokes of magnet	6	12
Output power (P_o) at base speed	274.83 W	431.82 W
Maximum speed (n_m)	16000 rpm	8200 rpm
Base speed (n_b)	2800 rpm	2900 rpm
Direct-axis inductance	0.275 mH	0.167 mH
Constant power ratio (CPR)	5.71	2.83
Total number of turns/phase	72	
Rotor pole number	14	
Applied current	15 A	
Air-gap length	0.5 mm	
Stack length	25 mm	
Machine outer radius	45 mm	
Coil factor	0.6	
Core material	M330–35A	
Coil material	Copper	

Grade of magnet	N38SH

The constant power ratio (CPR) of the analyzed machine is calculated as ratio of the maximum feasible speed (n_m) to its base speed (n_b), during field-weakening operation mode. The CPR expression is given in Eq. (1). This CPR ratio; Eq (1) is an indirect benchmark for measuring a machine's field-weakening capability (Hua *et al*, 2006). The predicted torque ripple (T_r) of the analyzed machine types is calculated using Eq. (2).

$$CPR = \frac{n_m}{n_b} \tag{1}$$

Estimated efficiency of the investigated machine types is mathematically expressed in Eq. (3), as implemented in Awah, (2022) and Jung *et al*, (2023).

$$T_r = \frac{T_{\max} - T_{\min}}{T_{avg}} \tag{2}$$

Where: T_{max}, T_{min} and T_{avg} is the maximum, minimum and average torque, respectively (Yu *et al*, 2023).

$$\eta = \frac{P_o}{P_o + P_i + P_{pm} + P_{cu}} \times 100\% \tag{3}$$

Where: P_o is the output power, P_i is the core or iron loss, P_{pm} is the eddy current loss due to the magnets and P_{cu} is the copper loss.

3. RESULTS AND DISCUSSION

The magnetic field vectors of the compared machines are presented in Figure 2. It is observed that the magnetic fields are more pronounced in Type II machine, and this feature would have positive impact towards the electromagnetic output of the machine, in terms of higher flux generation and consequent electromagnetic torque production. Also, the generated voltage of the compared machine types is shown in Figure 3(a) and (b). Again, Type II machine is seen to have higher voltage value than its Type I counterpart. The three-phase voltage waveforms of Type II machine seem to be more sinusoidal and symmetrical than that of Type I machine; the resulting fast Fourier transform (FFT) harmonic contents of the compared machines are provided in Figure 3(c). Meanwhile, the enormous non-fundamental harmonic elements of Type I machine would be detrimental to smooth operation of the machine, as highlighted in (Xu *et al*, 2010) and (Zhou and Zhu, 2014). Note that the generated voltage of Type I machine is only about 68.3% of its Type II equivalent.

Consequently, the generated electromagnetic torque value of Type I machine is much lower than that of Type II machine, as shown in Figure 4(a). The produced average torque of the machines as a function of applied copper loss is presented in Figure 4(b). It is worth noting that Type II machine has both larger electromagnetic torque and higher average torque than its compared Type I counterpart. The number of ripple in Type II machine is also doubled per electric cycle, since this feature would depend upon the machine's stator number and pole number arrangements, as inferred from Kwon *et al*, (2018).

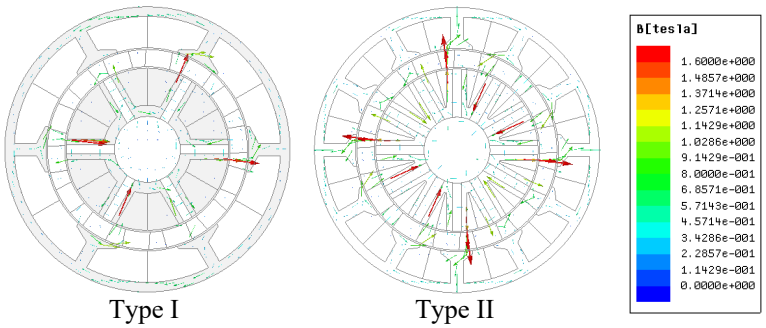

Type I Type II

Figure 2: Magnetic vector contours, on open-circuit

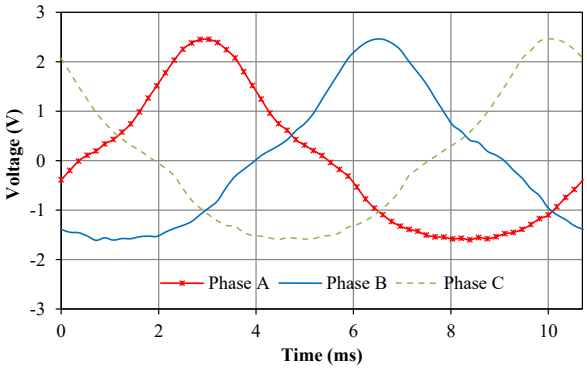

(a) Type I

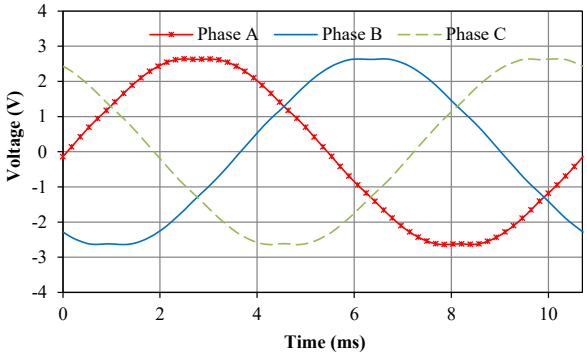

(b) Type II

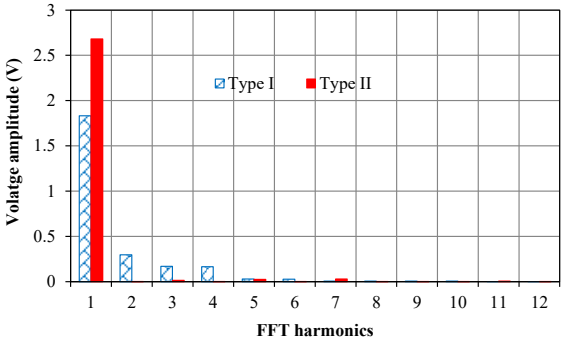

(c) Harmonic spectra

Figure 3: Comparison of induced voltage.

Furthermore, the torque-speed curves of the compared machine types are presented Figure 5. Obviously, Type I machine has wider speed coverage than Type II machine; albeit, with lower output torque value. It is worth mentioning that the speed of the compared machines would be largely dependent upon the machine's direct-axis inductance, as well as on the flux linkage contribution owing to the magnets, as highlighted in Wang *et al*, (2023). Hence, Type I machine would naturally have better field-weakening ability than Type II machine, considering their respective maximum speed and base speed plus their predicted direct-axis inductance values, given in Table 1.

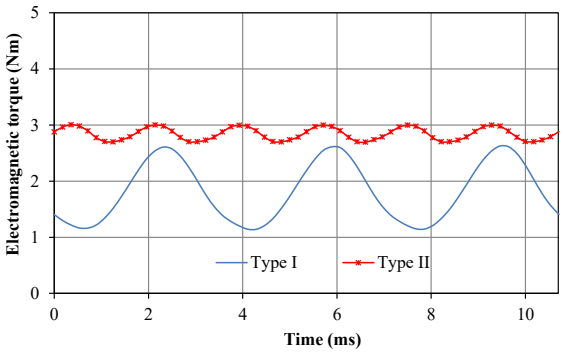

(a) Electromagnetic torque at constant copper loss condition

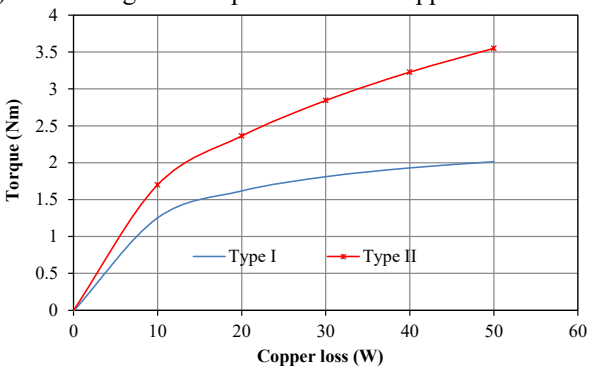

(b) Average torque

Figure 4: Torque comparisons.

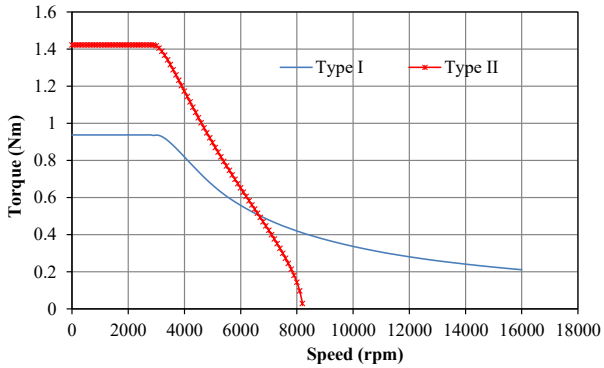

Figure 5: Torque-speed comparisons at rated current, 22.9 V

Figure 6 shows the static torque outlines and torque ripple values of the investigated machine types. Type II machine has a more uniform and symmetric waveform compared to that of Type I machine category. The uneven distribution of Type I static torque waveform could be attributed to its high unwanted harmonic contents; consequently, the resultant torque ripple value of Type I machine is noticeably higher than that of its corresponding Type II machine, as revealed in Figure 6(b). It is important to note that torque ripple amplitude of an electrical machine is a direct consequence of its harmonic contents, as highlighted in Owen *et al*, (2010).

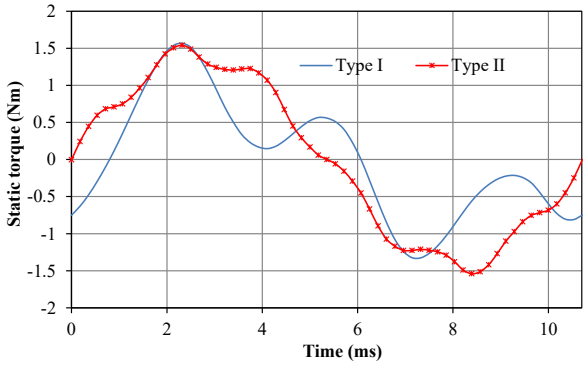

(a) Static torque

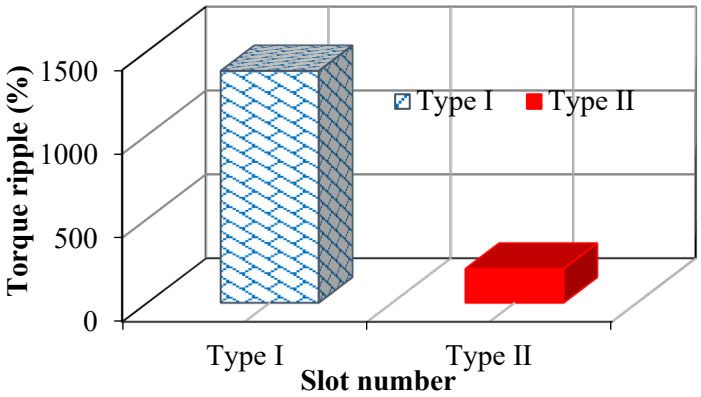

(b) Torque ripple

Figure 6: Static torque and torque ripple comparisons at 15 A.

Although, Type I machine has higher eddy current loss and stator iron loss than the Type II machine, as shown in Figure 7(a) and (b); it has lower rotor iron loss than Type II machine, as shown in Figure 7(c). The predicted loss results are in conformity with the obtained loss results presented in Wang *et al*, (2014b). Meanwhile, Type I machine has better efficiency than Type II equivalent, at lower operating speed. Nevertheless, the Type II machine category exhibits superior efficiency potential at high working speed, compared to Type I machine; as depicted in Figure 8. Moreover, enhanced machine efficiency could be realized from an electric machine by implementing newly developed soft magnetic core materials, which certainly reduces a machine's overall loss value or through appropriate segmentation of the applied magnet material (Chen *et al*, 2020).

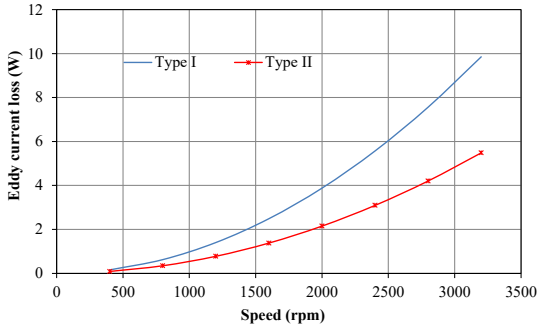

(a)

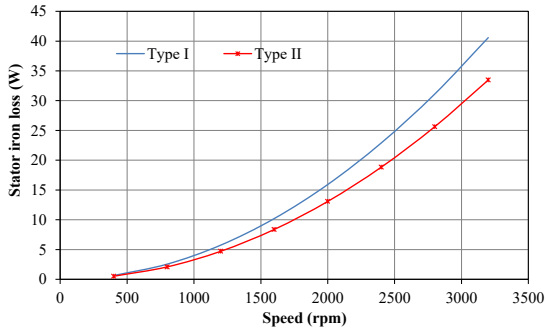

(b)

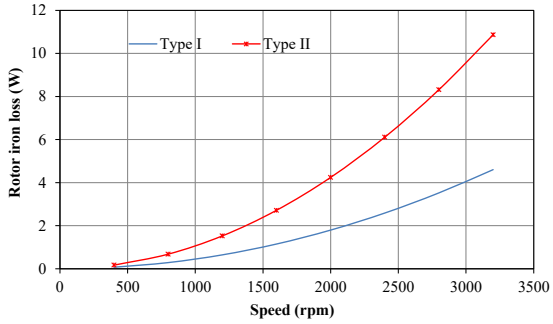

(c)

Figure 7: Loss comparisons.

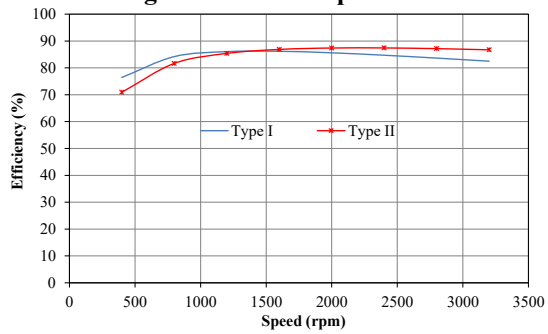

Figure 8: Comparison of efficiency.

4. CONCLUSION

Influence of stator slot number on the performance of a given double stator permanent magnet machine is analyzed and compared in this study. The increased number of slots in this investigation yielded higher induced-voltage value, larger output torque, lower undesirable harmonic contents, lower torque ripple value and evenly-distributed voltage and static torque waveforms, amongst other merits. Type I machine exhibits higher potential for high speed machine applications, as well as better efficiency at low working speed compared to Type II machine category. The investigated machine types would be suitable in low speed high torque direct-drive applications. About 34.5 % and 31.7 % increase is realized in the torque and induced-voltage magnitudes of the investigated machine, by doubling the slot number from six (6) to twelve (12), under normal working conditions. The obtained output power of the machine increased from 283.81W to 431.82 W, as a result of the slot number increase.

REFERENCES

Awah, C.C. (2022). Loss and efficiency comparisons of permanent magnet machine having double stator structure. Nigerian Journal of Engineering, 29(2): 33–39.

Chen, Q.; D. Liang; S. Jia, Q. Ze and Y. Liu. (2020). Analysis of winding MMF and loss for axial flux PMSM with FSCW layout and YASA topology. IEEE Transactions on Industry Applications, 56(3): 2622–2635.

Ding, Z.; C. He; C. Feng and J. Yang. (2023). A new dual stator permanent magnet machine based on field modulation theory. Sustainability, 15(1): 281.

Hua, W.; M. Cheng; Z.Q. Zhu, D. Howe. (2006). Design of flux-switching permanent magnet machine considering the limitation of inverter and flux-weakening capability. Paper presented at IEEE Industry Applications Conference Forty-First IAS Annual Meeting. Tampa, USA, pp. 2403–2410: IEEE.

Jiang, M; W. FU, and S. Niu. (2021). Design and analysis of a novel dual-airgap dual permanent magnet vernier machine, IEEE Access, 9: 57188-57197.

Jung, W.; H. Lee; Y. Lee, S. Kim, J. Lee and J. Choi. (2023). Analysis and comparison of permanent magnet synchronous motors according to rotor type under the same design specifications. Energies, 16(3): 1306.

Kwon, J.; J. Lee; W. Zhao and B. Kwon. (2018). Flux-switching permanent magnet machine with phase-group concentrated-coil windings and cogging torque reduction technique. Energies, 11(10): 2758.

Owen, R.L.; Z.Q. Zhu; A.S. Thomas, G.W. Jewell and D. Howe. (2010). Alternate poles wound flux-switching permanent-magnet brushless AC machines. IEEE Transactions on Industry Applications, 46(2): 790–797.

Siddiqi, M.R.; T. Yazdan; J. Im, M. Humza and J. Hur. (2021). Design and analysis of a dual airgap radial flux permanent magnet vernier machine with yokeless rotor. Energies, 14(8): 2311.

Su, P.; W. Hua; Z. Wu, Z. Chen, G. Zhang, M. Cheng. (2019). Comprehensive comparison of rotor permanent magnet and stator permanent magnet flux-switching machines. IEEE Transactions on Industrial Electronics, 66(8): 5862–5871.

Tang, Y.; E. Ilhan; J.J.H. Paulides and E.A. Lomonova. (2013). Design considerations of flux-switching machines with permanent magnet or dc excitation. Paper presented at 15th European Conference on Power Electronics and Applications (EPE). Lille, France, pp. 1–10: IEEE.

Ullah, W.; F. Khan and S. Hussain. (2022). A comparative study of dual stator with novel dual rotor permanent magnet flux switching generator for counter rotating wind turbine applications, IEEE Access, 10: 8243–8261.

Wang, J.; K. Atallah; Z.Q. Zhu and David Howe. (2008). Modular three-phase permanent-magnet brushless machines for in-wheel applications. IEEE Transactions on Vehicular Technology, 57(5): 2714–2720.

Wang, K.; Z.Q. Zhu and G. Ombach. (2014a). Synthesis of high performance fractional-slot permanent-magnet machines with coil-pitch of two slot-pitches. IEEE Transactions on Energy Conversion, 29(3): 758–770.

Wang, K.; Z.Q. Zhu; G. Ombach, M. Koch, S. Zhang and J. Xu. (2014b). Electromagnetic performance of an 18-slot/10-pole fractional-slot surface-mounted permanent-magnet machine. IEEE Transactions on Industry Applications, 50(6): 3685–3696.

Xiao, Y.; Z.Q. Zhu; G.W. Jewell, J. Chen, Di Wu and L. Gong. (2021). A novel spoke-type asymmetric rotor interior permanent magnet machine. IEEE Transactions on Industry Applications, 57(5): 4840–4851.

Xu, W.; J. Zhu; Y. Zhang, Y. Wang, Y. Li and J. Hu. (2010). Flux-switching permanent magnet machine drive system for plug-in hybrid electrical vehicle. Paper presented at 20th Australian Universities Power Engineering Conference. Christchurch, New Zealand, pp. 1–6: IEEE

Yu, Y.; Y. Pan; Q. Chen, Y. Hu, J. Gao, Z. Zhao, S. Niu and S. Zhou. (2023). Multi-objective optimization strategy for permanent magnet synchronous motor based on combined surrogate model and optimization algorithm. Energies, 16(4): 1630.

Zhang, J.; M. Cheng; Z. Chen and W. Hua. (2009). Comparison of stator-mounted permanent-magnet machines based on a general power equation. IEEE Transactions on Energy Conversion, 24(4): 826–834.

Zhang, Y.; W. Hua, M. Cheng, X. Li (2012). Comprehensive comparison of novel stator surface-mounted permanent magnet machines. Paper presented at IEEE International Conference on Electrical Machines. Marseille, France, pp. 589–594: IEEE.

Zhao, J.; Y. Wang, J. Li and H. Hu. (2022). Comparative study on torque performance of five-phase single-stator and double-stator permanent magnet synchronous motors. CES Transactions on Electrical Machines and Systems, 6(1): 46–52.

Zhou, Y.J. and Zhu, Z.Q. (2014). Comparison of wound-field switched-flux machines. IEEE Transactions on Industry Applications, 50(5): 3314–3324.

Zhu, Z.Q.; M.L.M. Jamil and L.J. Wu. (2013). Influence of slot and pole number combinations on unbalanced magnetic force in PM machines with diametrically asymmetric windings. IEEE Transactions on Industry Applications, 49(1): 19–30.

PAPER 60 – EXPERIMENTAL PROCESS OPTIMIZATION AND GC-MS CHARACTERIZATION OF BIOACTIVE ANTIOXIDANT EXTRACT PRODUCTION FROM HYPTIS SUAVEOLENS LEAVES

Aguele, Felix Osarumhense[1], Oke, Emmanuel Olusola[1*], Abam, Fidelis I.[2]

[1]Department of Chemical Engineering, Michael Okpara University of Agricultture, Umudike (MOUAU), Nigeria.
[2]Department of Mechanical Engineering, University of Calabar, Nigeria.

*Email: oke.olusola@mouau.edu.ng

ABSTRACT

Previous studies documented the biological and antioxidant activities of phenolic bioactive extract (phytochemical) from Nigerian Hyptis suaveolens leaves. However, optimization of solid-liquid extraction of the process for possible scale-up process design is seldom reported in the literature. Therefore, this investigation presents process optimization and characterization of bioactive extract recovery from Hyptis suaveolens leaves. Solid-liquid extraction experiment was designed at ranging extraction time (30 - 70 min), temperature (60 -75 oC) and substrate/solvent ratio (0.4 – 0.8 g/100ml) using Box-Benken Design (BBD) in Response Surface Methodology (RSM) of Design Expert software V13 with Total Phenolic Content (TPC), Total Flavonoid Content (TFC), and extraction yields as dependent variables. BBD desirability algorithm was used to perform optimum conditions that optimized TPC, TFC and extraction yield. At the optimized process conditions of 61.28 mins, 62.74 oC and 0.58 g/100ml, the extract obtained gave TPC (33.055 mg GAE/g d.w.), TFC (7.151 mg QE/g d.w.) and yield (18.203%). The Gas Chromatography - Mass Spectroscopy (GC-MS) analysis of extracts recovered was observed to have a wide array of compounds, dominated by methyl esters (about 43%), ethyl-oleate (about 16%), acids (about 13%) and many other components at lower levels. The Fourier Transform Infra-Red (FT-IR) analysis indicated the presence of functional groups, which are attributable to antioxidants.

KEYWORDS: Optimization, Bioactive, Antioxidant, Extraction, Hyptis suaveolens, GC-MS

1. INTRODUCTION

Hyptis suavoelens (L. Poit) is an essential medicinal plant also known as bush tea, belonging to the family lamiaceae (Umedum et al., 2014). The plant has been reported to be traditionally utilized as an antisplasmoidic against diarrhea and colds (Singh et al., 2011) while the leaves are used to repel mosquitoes (Vongsombath et al., 2012) due to the presence of bioactive compounds in the plant. Extraction process is the crucial step to adequate utilization of the bioactive compounds (Kamarudin *et al.,* 2020). However, the efficiency of the extraction process highly depends on the extraction techniques adopted (Aybastier et al., 2013). Due to the simplicity and efficiency of the heat assisted extraction (HAE) technique, it has been employed by researchers for the extraction of bioactive compounds from different plant materials (Ekezie et al., 2017; Oke et al., 2022). Jovanovic *et al.,* (2023) reported the extraction and optimization of bioactive compounds from *Gentiana asclepiadea* L. Bankova et al., (2021) inferred that the HAE process gave high product yield with reduced process time and solvent consumption than the traditional extraction techniques. The efficiency of the extraction process is determined by the process parameters such as extraction time, temperature and substrate/solvent ratio (Alara *et al.*, 2018a). The solubility and diffusion rate of the phenolic compounds in a plant is influenced by the extraction temperature (Santos et al., 2012) while the mass transfer of bioactive compound during extraction is product of the extraction time (Oke et al., 2020). Simultaneous evaluation of multiple responses in a process is an essential feature of the response surface methodology (RSM) as it mathematically depicts the interaction effects of the process parameters as well as the optimal values for the process (Ibrahim and Elkhidir, 2011; Azahar et al., 2017). Therefore, the RSM technique was employed to study the interaction effects of extraction time, temperature and substrate/solvent ratio on the Total Phenolic Content (TPC), Total Flavonoid Content (TFC), and extraction yield of *Hyptis suaveolens* leaves extract. Identification of the bioactive antioxidants of the

leaves extract was quantified through GC-MS and FT-IR analysis to determine the functional group present in the extract.

2. METHODOLOGY

2.1 Plant materials and Chemical Reagent

The fresh plant material (Hyptis sauveolens) was obtained from some botanical gardens in Ogbomosho, Oyo State, Nigeria. Other reagents and chemicals such as Gallic acid, Folin–Ciocalteu, ethanol and anhydrous sodium carbonate, quercetin, chlorogenic acid, cafeic acid, sodium hydroxide, aluminum chloride, potassium acetate, and rutin samples used in this study were analytical grade products of Sigma-Aldrich, Germany. They were obtained from various reliable chemical vendors and were used as obtained, without modification. Distilled water was obtained from Chemistry department laboratory, Michael Okpara University of Agriculture, Umudike, Nigeria.

2.2 Preparation of Substrate and Extraction

The fresh materials (*Hyptis suaveolens* leaves) were plucked off the plant stems, washed, and dried in an aerated environment shaded from direct sun light, at a temperature of about 30^{o}C for six (6) days. The dried leaves were ground to obtain fine particles and to enhance effective extraction. The ground material was then preserved properly in a compartment at 4^{o}C before extraction was done. The extraction was done in a water bath, using appropriate solvent mixture and parameters according to the design. The parameters ranges were time (30 – 70 min), temperature (60 – 75 ^{o}C) and substrate/solvent (S/L) (0.4 – 0.8 g/100ml). The extracts were filtered using Whatman filter paper No 1, evaporated and properly preserved at 4^{o}C for further analyses. The yield was calculated using Equation 1.

$$Yield = \left(\frac{\text{Mass of Bioactive Extracts obtained}}{Mass\ of\ dried\ ground\ leaves\ used}\right) \times 100\% \quad \text{---------- 1}$$

2.3 Determination of Total Phenolic Content (TPC)

The TPC of Hyptis suaveolens extract was determine, using Folin-Ciocalteu's (FC) phenol reagent, adopting the procedure described by Alara and coworkers with slight modifications (Alara et al., 2018a). A small volume of distilled water was taken and topped up to 1 ml by adding 100 µl of extract. Next, 0.2 ml of the FC reagent was then added, thoroughly mixed and incubated in the dark at room temperature for 5 minutes. Then 0.6 ml of 0.2 mM of Na_2CO_3 solution was added and incubation was again done at room temperature in the dark for a period of 120 minutes. Then the absorbance was measured at 765 nm with a UV–VIS Spectrophotometer (Hitachi U-1800, Japan). Using different concentration solutions of gallic acid (50–500 mg/ml), a standard calibration curve was prepared. TPC was then expressed as mg gallic acid equivalents per gram of dried weight sample (mg GAE/g d.w.). The TPC of the extracts were then obtained using Equation. The analyses were done in triplicate and water was used as the blank.

$$TPC = \frac{Concentration\left(\frac{mg}{ml}\right) \times solvent\ volume\ used\ (ml)}{Weight\ of\ dried\ sample\ (g)} \quad \text{---------- 2}$$

2.4 Determination of Total Flavonoid Content (TFC)

To determine the TFC in the Hyptis suaveolens leaves extract, the methodology previously reported by other researchers was adopted with a little modification (Alara et al., 2018). 100 µL of 2% $AlCl_3$ solution was added to 100 µL of the Hyptis suaveolens extract, mixed vigorously and then kept at room temperature for 60 minutes. The absorbance was measured at 420 nm using a UV-vis Spectrophotometer (Hitachi U-1800, Japan). The quercetin acid standard calibration curve was preparred using different concentration solution of quercetin acid (50 - 500 mg/l). Then, the concentration of TFC in the extract was calculated with equation of line $y = 10.39x + 0.305$, $R^2 = 0.9941$ (where y is the absorbance at 510 nm and x is the concentration of TFC from the calibration curve), TFC was determined using Equation 3, and results were reported as quercetin equivalent in milligram per gram of dried weight sample (mg QE/g d.w.).

$$TFC = \frac{Concentration\left(\frac{mg}{ml}\right) \times solvent\ volume\ used\ (ml)}{Weight\ of\ dried\ sample\ (g)} \quad \text{----------} \quad 3$$

2.5 Experimental Design and Analysis

The extraction parameters were studied using three-factor, three-level box benhken design (BBD) of response surface methodology (RSM) in design expert software V13, which gave 17 experimental runs. The parameters studied include time (minutes), temperature (ºC) and substrate/solvent ratio (g/100ml). The experimental design is presented in Table 1. Second order polynomial equations were used to study the relationships between the process parameters and the responses of TPC, TFC and extract yield, as expressed in equations 3, 4 and 5, respectively.

2.6 GC-MS Analysis

The Hyptis suaveolens leaves extract was subjected to GC-MS investigation for constituent profiling. The Gas Chromatography equipment (Agilent 6890 series) equipped with HP-5MS column mass spectrometer was used. The procedure described previously by Kulkarni and coworkers (Kulkarni et al., 2015) was adapted. During the analytical operation, the initial column temperature of 30 ºC was raised to 300 ºC at a rate of 10 °C /5min. High purity helium flowing at 1.0ml/min was used as carrier gas. Compounds identification was done in accordance with the retention time and integral area of peaks. Based on the NIST library search, the similarity of compounds match with > 70% are listed.

2.7 FT-IR Analysis

FT-IR analysis was employed to characterize the extract obtained from Hyptis suaveolens. The procedures reported in previous researches were adapted (Alara et al., 2018b; Kumar and Thampi, 2015). The Hyptis suaveolens extract was subjected to spectrophotometer infrared scanning (Agilent Technologies, Cary 630 FTIR), employing wave number in the region between 4000-650cm^{-1}, which registered the characteristic peaks during the tests. The detected characteristic peak values and their functional groups of the FT-IR were recorded. The IR chart was used to interpret the infrared absorption frequencies of functional groups spectra obtained for the extract.

Table 1: Summary of Experimental Design Factors and levels

Factors	**Level**		
	-1	**0**	**+1**
A: Extraction Temperature (ºC)	60	67.50	75
B: Extraction Time (minutes)	30	50	70
C: Substrate/Solvent ratio (S/L) (g/100ml)	0.4	0.6	0.8

3. RESULTS AND DISCUSSION

3.1 Experimental result and model fittings

The extraction experiment for the *Hyptis suaveolens* leaves comprised three process parameters: extraction temperature, time, and substrate/solvent ratio (S/L) resulting in 17 experimental runs using the BBD design. The experimental values of the TPC, TFC, and extraction yield at various extraction conditions are presented in Table 2. The TPC values varied from 19.45 to 43 gGAE/100g d.w., while the TFC varied from 4.75 to 11.17 gQE/100g d.w and the extract yield varied from 12 to 27%. The obtained optimal values of the bioactive compound were similar to the values obtained by Sanou *et al.,* (2023) from *Hibiscus sabdariffa* L. The experimental data subjected to multiple regression analysis depicted a second-order polynomial equation for each of the responses, TPC (equation 4), TFC (equation 5), and extract yield (equation 6).

$$\mathbf{TPC} = +34.40 - 2.34A + 0.8238B - 7.81C + 2.00AB + 3.06AC - 2.02BC - 5.42A^2 - 4.25B^2 + 0.3850C^2 \quad (4)$$

$$\textbf{TFC} = +6.27 - 1.05A - 0.6350B - 0.6875C + 1.12AB - 0.5950AC - 2.03BC + 0.9260A^2 + 1.49B^2 + 0.5260C^2 \quad (5)$$

$$\textbf{YIELD} = +21.40 + 2.75A + 2.75B + 1.75C + 4.25AB + 0.7500AC - 1.25BC - 1.58A^2 - 2.58B^2 + 2.43C^2 \quad (6)$$

The statistical significance of the regression models was depicted by the ANOVA models in RSM and presented in Table 3. The quadratic models showed a significant p-value of <0.0001, 0.0012, and 0.0118 for the TPC, TFC, and yield respectively at a 95% ($p<0.05$) level of significance. The lack of fit of the models; TPC (0.0531 gGAE/100g d.w.), TFC (0.3313 gQE/100g d.w), and yield (0.1163) were not statistically significant confirming the fitness of the models and their relationship with the process parameters (Kamarudin *et al.,* 2020). The high coefficient of determination (R^2) values of 0.9835 gGAE/100g d.w. (TPC), 0.9456 gQE/100g d.w. (TFC), and 0.8907 (yield) corroborated the efficiency of the model equations for accurate predictions of the bioactive antioxidants whereas the agreement between the actual and predicted values of the models were indicated by the adjusted R^2 values (Mushtaq *et al.,* 2015).

Table 2: Experiment result

Run	Temp	Time	S/L	TPC	TFC	YIELD
1	75	50	0.4	33.16	8.25	25
2	67.5	30	0.8	24.24	10.87	23
3	67.5	50	0.6	33.98	5.83	23
4	67.5	70	0.8	23.04	4.75	26
5	67.5	50	0.6	34.47	7.12	22
6	60	30	0.6	29.33	11.17	17
7	75	30	0.6	19.68	6.67	12
8	67.5	30	0.4	34	7.75	14
9	67.5	50	0.6	35.06	5.63	19
10	60	70	0.6	25.79	8.45	14
11	67.5	50	0.6	33.32	6.59	22
12	75	50	0.8	21.84	5.25	27
13	60	50	0.4	43	9	19
14	75	70	0.6	24.13	8.43	26
15	60	50	0.8	19.45	8.38	18
16	67.5	70	0.4	40.88	9.75	22
17	67.5	50	0.6	35.17	6.17	21

Table 3: ANOVA model fittings of the bioactive antioxidants

	TPC	TFC	YIELD
F-value	46.45	13.52	6.34
p-value	< 0.0001	0.0012	0.0118
Std. Dev.	1.4	0.6672	2.24
Mean	30.03	7.65	20.59
C.V. %	4.66	8.72	10.89
R^2	0.9835	0.9456	0.8907
Adjusted R^2	0.9624	0.8756	0.7502
Predicted R^2	0.7778	0.4919	-0.3361
Adeq Precision	21.4512	12.815	8.4308
Lack of fit	0.0531	0.3313	0.1163

3.2 Influence of the process parameters on the bioactive antioxidants

The combined effects of the process parameters on the bioactive antioxidants of *Hyptis suaveolens* leaves were depicted with the 3-D modelling of the RSM (Figures 1a-i). Figure 1a indicated that increase in temperature decreases the TPC value while increase in extraction time increases the TPC. Increasing the temperature and S/L ratio decreased the TPC as shown in Figure 1b, while Figure 1c indicated that increase in S/L ratio decreased the TPC and increase in time increased the TPC. Increase in extraction temperature surges heat activation which enhances the diffusion rate of soluble phenolic compounds from substrates, however beyond the certain heat threshold, thermal lability may occur which reduces the TPC yield (Rosello-Soto *et al.,* 2019). This finding concurred to the report of Kamarudin *et al.,* (2020) on the extraction of phenolic compounds from *Eleutherine bulbosa.* In Figure 1d, increase in extraction time decreased the TFC but increase in temperature elevated the TFC. Prolonged time exposure of flavonoid to heat, thermally degrades the bioactive compound, reducing its yield, however, increasing temperature improves the solubility of flavonoids (Chen *et al.,* 2007). Increasing the temperature decrease the TFC value whereas increase in the S/L ratio increased the TFC (Figure 1e). Due to the solubility of bioactive compounds in polar solvents, increasing the S/L ratio simultaneously increased the TFC yield (Bahtar and Annisa, 2018). Figure 1f showed that increase in extraction time and S/L ratio increased the TFC yield. Increasing the extraction time and temperature increase the extract yield (Figure 1g). Similarly Figure 1h indicated that increase in temperature and S/L ratio increased the extract yield and Figure 1i depicted a simultaneous increase in yield as the extraction time and S/L ratio increase.

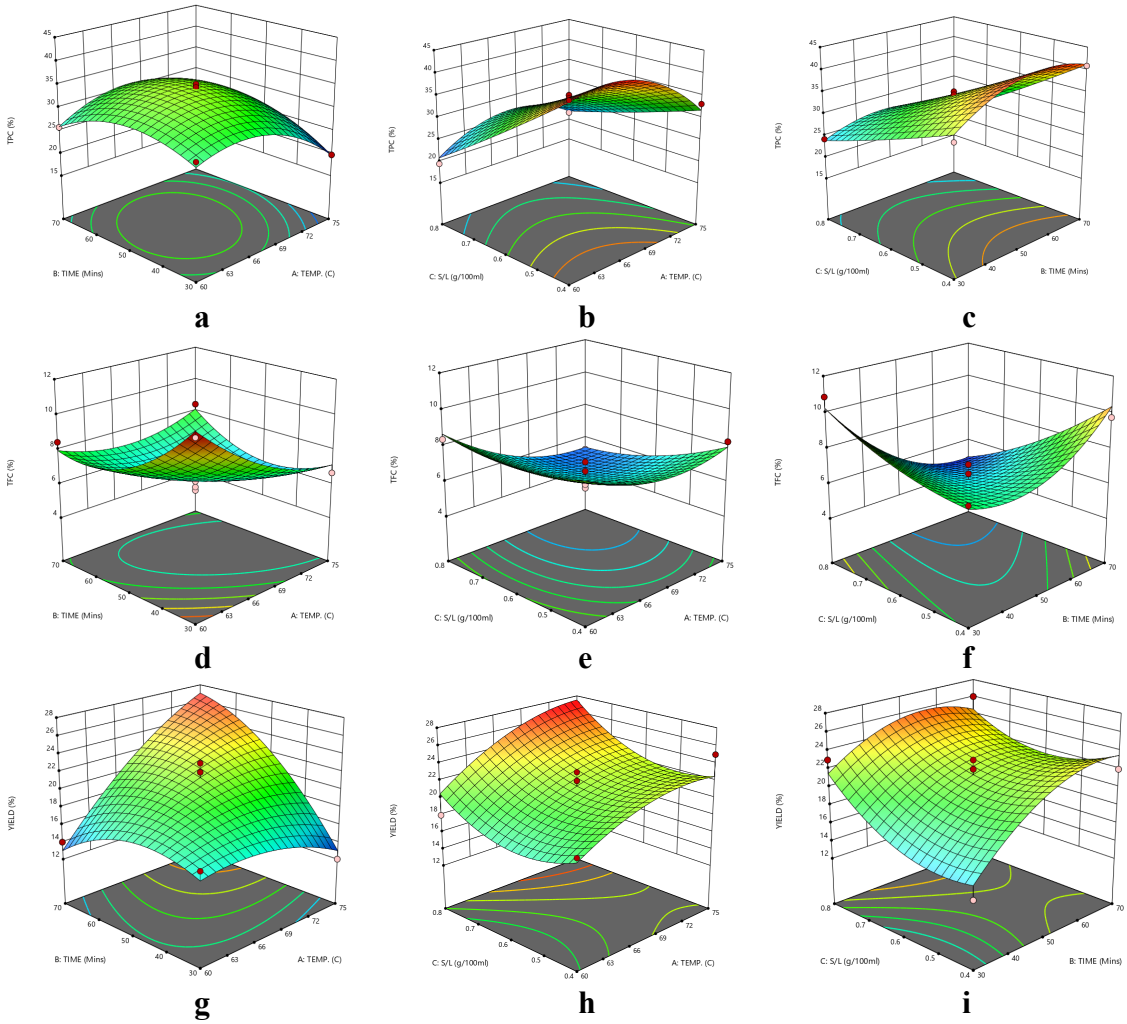

Figure 1: Effect of extraction time, temperature and substrate/solvent ratio on TPC (a-c), TFC (d-f) and yield (g-i)

3.3 Optimization studies of the bioactive antioxidants

Numerical optimization tool of Response Surface Methodology in Design Expert version 13 was used for optimizing the process parameters of the extraction process. The optimization was conducted "in the range" of the process parameters and responses. The optimization plot (Figure 2) depicted the optimal responses at the varied optimal process conditions. The optimal value of 33.055 mg GAE/100 g dw, 7.151 mg QE/100 g d.w and 18.203% were obtained for the TPC, TFC and yield respectively at optimal temperature of 62.74 ^{0}C, 61.28 minutes and S/L ratio of 0.58 g/100 ml at desirability value of 1. This inferred the agreement between the experimental and predicted values at confidence interval of 1%.

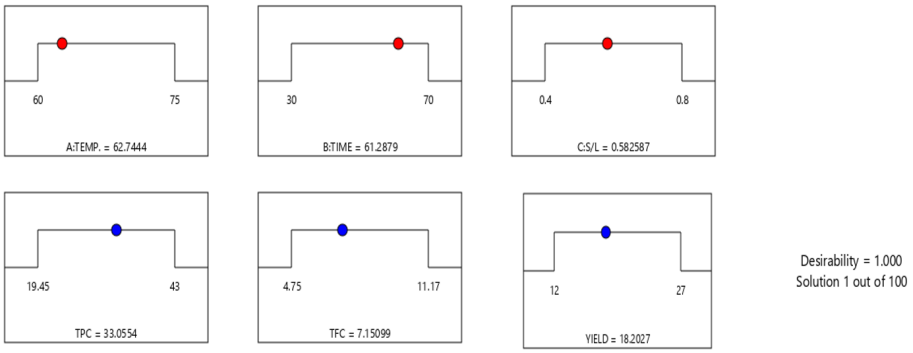

Figure 2: Optimization of the bioactive antioxidants extraction process

3.4 Characterization of *Hyptis suaveolens* leaves extract

The extract from *Hyptis suaveolens* leaves was characterized using Fourier Transform Infra-Red (FTIR) and Gas Chromatography – Mass Spectrograph (GC-MS). The GC-MS analysis of extracts recovered (Figure 3) was observed to have a wide array of compounds, dominated by methyl esters (about 43%), ethyl-oleate (about 16%), acids (about 13%) and many other components at lower levels. The identification of the functional group in the *Hyptis suaveolens* leaves using FT-IR (Figure 4) indicated strong peaks at 3339.7 cm^{-1} , 2974.4 cm^{-1}, 1043.7 cm^{-1} and 879.7 indicating the presence of O-H (hydroxyl group), CH_3 (lipid), C-O (lipid) and C-C (alkane) respectively. Other functional groups showed medium to weak peaks, indicating the presence of compounds, such as secondary alcohol, alkene, and amino compounds. These bioactive compounds were attributable to antioxidants and are responsible for the pharmacological activities of the plant extracts (Pakkirisamy *et al.,* 2017).

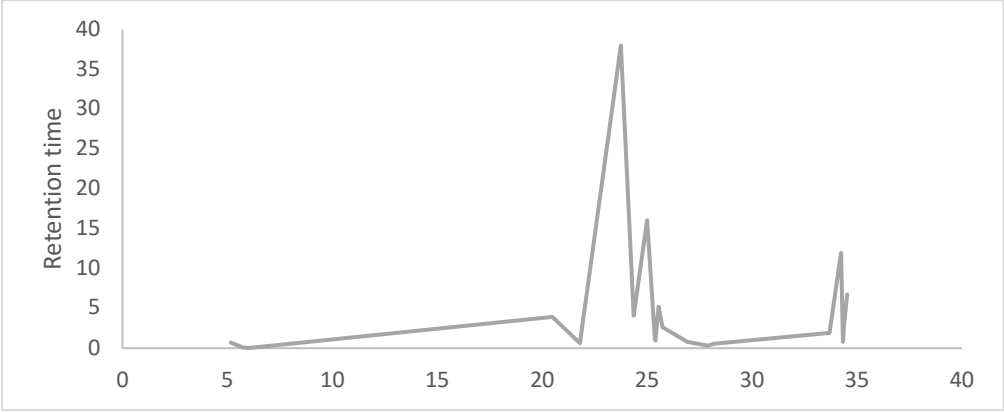

Figure 3: GC-MS spectrograph of *Hyptis suaveolens* leaves extract

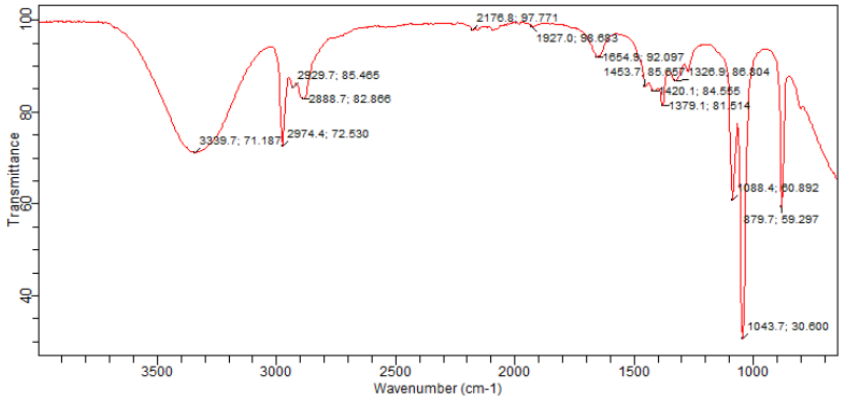

Figure 4: FT-IR analysis of the *Hyptis suaveolens* leaves extract

4. CONCLUSION

The conventional heat assisted extraction of bioactive antioxidants from the leaves of Hyptis suaveolens plants indicated optimal values of 33.055 mg GAE/g d.w., 7.151 mg QE/g d.w. and 18.203% for the TPC, TFC and yield respectively, at optimized process conditions of 61.28 minutes, 62.74 ºC and 0.58g/100ml. The GC-MS analysis indicated that the *Hyptis suaveolens* leaves extract is dominated by methyl esters (about 43%), ethyl-oleate (about 16%), acids (about 13%) and many other components with lower values. The FT-IR analysis indicated the presence of functional groups, which are attributable to antioxidants.

REFERENCES

Alara, O. R., Abdurahman, N. H., & Ukaegbu, C. I. (2018a). Soxhlet extraction of phenolic compounds from Vernonia cinerea leaves and its antioxidant activity. *Journal of Applied Research on Medicinal and Aromatic Plants*, *11*, 12-17.

Alara, O. R., Abdurahman, N. H., Mudalip, S. K. A., and Olalere, O. A. (2018b). Characterization and effect of extraction solvents on the yield and total phenolic content from Vernonia amygdalina leaves. *Journal of Food Measurement and Characterization*, *12*(1), 311-316.

Azahar, N.F., Gani, S.S.A., Mokhtar, N.F.M., (2017). Optimization of phenolics and flavonoids extraction conditions of Curcuma Zedoaria leaves using response surface methodology. Chem. Central J. 11 (1), 96.

Bankova V, Trusheva B, Popova M (2021) Propolis extraction methods: a review. J Apic Res 60(5):734–743

Ekezie FGC, Sun DW, Cheng JH (2017) Acceleration of microwaveassisted extraction processes of food components by integrating technologies and applying emerging solvents: a review of latest developments. Trends Food Sci Technol 67:160–172

Ibrahim, H.M., Elkhidir, E.E., (2011) Response surface method as an efficient tool for medium optimisation. Trends Appl. Sci. Res. 6 (2), 121–129.

Jovanovic, M. S., Milutinovic, M., Lazarevic, Z., Mudric, J., Matejic, J., Kitic, D. and Savikin, K. (2023). Heat- and microwave-assisted extraction of bioactive compounds from Gentiana asclepiadea L. underground parts: Optimization and comparative assessment using response surface methodology. Journal of Applied Research on Medicinal and Aromatic Plants (2023): 10048

Jesus, N. Z. T., Falcão, H. S., Lima, G. R. M., Caldas Filho, M. R. D., Sales, I. R. P., Gomes, I. F., ... & Batista, L. M. (2013). Hyptis suaveolens (L.) Poit (Lamiaceae), a medicinal plant protects the stomach against several gastric ulcer models. *Journal of ethnopharmacology*, *150*(3), 982-988.

Kamarudin, A. A., Esa, N. M., Saad, N. and Sayuti, N. H. (2020). Heat assisted extraction of phenolic compounds from Eleutherine bulbosa (Mill.) bulb and its bioactive profiles using response surface methodology. Industrial Crops & Products 144 (2020) 112064

Kulkarni, A., Govindappa, M., Ramachandra, Y.L., Koka, P., (2015). GC-MS analysis of methanol extract of Cassia fistula and its in vitro anticancer activity on human prostate cancer cell line. Indo. Am. J. Pharm. Res. 5, 937–944.

Kumar, S. N. and Thampi, N. (2015,) Phytochemical screening and characterization of the bioactive compounds from the leaves of Hyptis suaveolens and Spathodea campanulata J. Chem. Pharm. Res., 7(7):840-850

Li, R., Tang, G., Liu, X., Li, J., Wang, D., & Ji, S. (2020). An ethnopharmacological review of Hyptis suaveolens (L.) Poit. *Tropical Journal of Pharmaceutical Research*, *19*(7), 1541-1550.

McNeil, M., Facey, P., & Porter, R. (2011). Essential oils from the Hyptis genus-a review (1909-2009). *Natural Product Communications*, *6*(11), 1934578X1100601149.

Mushtaq, M., Sultana, B., Bhatti, H. N. and Asghar, M. (2015). RSM based optimized enzyme-assisted extraction of antioxidant phenolics from underutilized watermelon (Citrullus lanatus Thunb.) rind. J Food Sci Technol (August 2015) 52(8):5048–5056

Oke, E. O., Adeyi, O., Okolo, B. I., Ude, C. J., Okhale, S. E., Otolorin, J. A., Nnabodo, D., Ajala, O. O., Anyanwu, A. S. and Okorie, U. D. (2022). Polyphenolic Extract Recovery from Azadirachta indica Leaves via Green Microwave-Assisted Extraction Technology: GA-ANFIS Prediction, Cuckoo Search Algorithm Optimization and ASPEN-Based Scale-Up Techno-economics. Process Integration and Optimization for Sustainability

Oke, E. O., Adeyi, O., Okolo, B. I., Adeyi, J. A., Ayanyemi, J., Osoh, K. A. and Adegoke, T. S. (2020). Phenolic compound extraction from Nigerian Azadirachta Indica leaves: Response surface and neuro-fuzzy modelling performance evaluation with Cuckoo Search multi-objective optimization

Pakkirisamy M., Kalakandan S. K. and Ravichandran K. (2017) Phytochemical Screening, GC-MS, FT-IR Analysis of Methanolic Extract of *Curcuma caesia* Roxb (Black Turmeric). Pharmacog J. 9(6):952-6.7

Roselló-Soto, E., Martí-Quijal, F. J., Cilla, A., Munekata, P. E., Lorenzo, J. M., Remize, F., Barba, F. J. (2019). Influence of temperature, solvent and pH on the selective extraction of phenolic compounds from Tigernuts by-products: triple-TOF-LC-MS-MS characterization. Molecules 24(4), 797.

Raja, N., Jeyasankar, A., Venkatesan, S. J., & Ignacimuthu, S. (2005). Efficacy of Hyptis suaveolens against lepidopteran pests. *Current Science*, *88*(2), 220-222.

Sanou, A., Konate, K., Kabakde, K., Dakuyo, R., Bazie, D., Hemayoro, S. and Dicko, M. H. (2023). Modelling and optimisation of ultrasound-assisted extraction of roselle phenolic compounds using the surface response method. Scientific Reports 13: 358

Santos, D.T., Veggi, P.C. and Meireles, M.A.A. (2012) Optimization and economic evaluation of pressurized liquid extraction of phenolic compounds from jabuticaba skins, J. Food Eng. 108 (3): 444–452

Singh, V., Shrivastava, G. and Shukla, S. (2011). Mosquito repellent activity of essential oils of *Hyptis suavoelens*. Journal of Pharmacy Research. 4(8):2778–2779.

Umedum, N. L., Ugochukwu, N. and Ifeoma, P. U. (2014). The efficacy of *Hyptis suavoelens*: A review of its nutritional and medicinal applications. European Journal of Medicinal plants. 4(6):661–674.

Xu, D. H., Huang, Y. S., Jiang, D. Q., & Yuan, K. (2013). The essential oils chemical compositions and antimicrobial, antioxidant activities and toxicity of three Hyptis species. *Pharmaceutical Biology*, *51*(9), 1125-1130.

Vongsombath, C., Palsson K. and Bjork L. A, (2012). Mosquito (Diptera: Culicidae) Repellency Field Tests of Essential Oils from Plants Traditionally used in Laos. Journal of Medical Entomology. 49(6):1398–1404.

PAPER 67 – EXPERIMENTAL STUDY OF THE PRESSURE DROP AND FLOODING IN A ROTATING PACKED BED

Usman Garba[1,2] , David Rouzineau[1] , Michel Meyer[1]

[1]Chemical Engineering Laboratory, University of Toulouse, CNRS, INPT, UPS, Toulouse, France
[2]Usmanu Danfodiyo University Sokoto, Nigeria
[*]Email: usman.garba@udusok.edu.ng

ABSTRACT
Embedded processes require compactness, low energy consumption, and insensitivity to gravity. Centrifugal processes respond to the last characteristic. Centrifugal force is used instead of the gravitational force with almost zero sensitivity to variations in the gravitational force. We studied a rotating packed bed (RPB) as a gas/liquid contactor for absorption. We focused our attention on the hydrodynamic behavior of this device. Previous studies on RPB flooding and operating limits dwelled on virtual observations and pressure drop variations. However, physical visualizations are subjective because RPB pressure drop variations are too inconsistent to be used to determine the upper operating limit during RPB operations. A robust quantitative method of obtaining RPB flooding limits based on the flow rate of the ejected liquid, supported by visual observation and pressure drop measurement, was presented. The aim was to identify, with greater accuracy, RPB hydrodynamic characteristics and provide a more standard method of identifying same.

KEYWORDS: Rotating packed bed, pressure drop, Flooding, Gas/liquid contactor, hydrodynamics,

1. INTRODUCTION

Reliance on gravitational force makes conventional packed columns for separation processes such as distillation and absorption to have unimpressive sizes and physical footprints which makes them uneconomical, especially where space and weight are (Adekola et al., 2012; Hilpert & Repke, 2021). The operating ranges of non-rotating, conventional, packed bed columns (PBCs) are limited by gravitational and frictional forces acting in opposite directions on the down-flowing liquid and the gas flowing from the bottom of the column. A RPB, also called HIGEE (High g) contactor, is a compact process intensification equipment in which a combination of sizeable allowable gas and liquid flowrates is achieved by superimposing gravitational force with centrifugal force. In RPBs, the higher gravitational force factor employable raises the combined operating range of the throughputs in addition to their flexibility due to the additional degree of freedom offered by the rotation speed (Groß et al., 2018).

A fundamental aspect of the modeling, design, optimization, and implementation of pilot-scale and subsequent scale-up of RPBs is the clear understanding of the principles of its hydrodynamics via accurate prediction of the pressure drops and upper operating limits (Hendry et al., 2020; Neumann, et al., 2017a). Also, (Zhang et al., 2020) observed that the mass transfer performance and efficiency of an RPB, as reflected by its gas pressure drop, is closely linked to its hydrodynamic characteristics, operating costs, and energy requirements. Hydrodynamic characteristics such as the pressure drop of an RPB are a useful index in measuring its resistance and consequent energy consumption (Liu et al., 2018). Many studies were carried out to evaluate the influence of pressure drop in many RPB operations with empirical and semi-empirical models established (Jiao et al., 2010; Singh et al., 1992). RPB hydrodynamic parameters extensively reported in the literature include liquid holdup (Burns et al., 2000; Burns & Ramshaw, 1996), gas pressure drop (Neumann et al., 2017b; Pyka et al., 2022), liquid dispersion (Burns & Ramshaw, 1996; Xie, 2019) and, flooding (Hendry et al., 2020; Lockett, 1995). Although extensive research has been conducted and documented using RPBs, with many of its applications explored at the industrial scale, its design approach is still case-specific. It thus requires improvements (Neumann, et al., 2017a).

This work presents a robust quantitative method of obtaining RPB upper operating limit based on the flow rate of the ejected liquid, supported by visual observation and pressure drop measurements. This was achieved by connecting a hydrocyclone to the gas outlet. In addition, a comprehensive pressure drop behavior and flooding for a countercurrent water-air system and a single-block stainless steel wire mesh packing using a double jet nozzle for the liquid inlet

were used to study the hydrodynamics of the pilot-scale RPB. The aim was to improve further the understanding of RPB hydrodynamics for design, scale-up, and energy conservation purposes.

The relatively high rotation speeds of RPBs combined with the size of the equipment make it possible to implement forces more than 100 times greater than gravity, greatly intensifying the transfer phenomena between phases (Pan et al., 2017). Rapid contact surface replacement in RPBs allows for high effective surface area packings of 2000 to 5000m^2/m^3 (Pan et al., 2017). This allows for higher mass transfer characteristics: gas-liquid interfacial area, gas-side and liquid-side volumetric mass transfer coefficients, and height of transfer unit (Cheng & Tan, 2011; Zhang et al., 2011). Also, this allows for the same separation performance in RPB to have much more flexible and compact equipment with a wider operating range than a gravity column used for absorption (L. L. Zhang et al., 2011). Overall, compared to conventional gravity columns, for a comparable processing capacity and efficiency, a RPB offers rotation as an extra degree of freedom, serves as the foundation of modular plants, and is more miniaturized with higher flexibility and energy efficiency (Neumann et al., 2018). The characteristics mentioned above make RPBs emblematic equipment for process intensification. Consequently, RPBs have been employed for various purposes in diverse fields such as separation processes, synthesis, and preparation of micro and nano-particles, petroleum products processing, biodiesel production, medical sciences, and pollution control (Hilpert & Repke, 2021; Neumann et al., 2018; L. L. Zhang et al., 2011).

A conventional, single-stage RPB is shown in Figure 1. It comprises of a casing surrounding a rotor mounted on a shaft and rotated by a motor. The rotor is a motor-driven, ring-shaped cylinder that encloses an annular packing mounted on either a horizontal or a vertical shaft. In countercurrent operation mode, gas is introduced into the outer periphery of the packing from the casing. The liquid is usually introduced into the center (or "eye") of the rotor via the liquid inlet through a stationary set of nozzles (liquid distributor) into the packing from the top of the RPB. After its transformation by centrifugal shear forces, the liquid flows in the form of rivulets, droplets, or films as determined by the rotation speed (Burns et al., 2000). The casing wall finally collects it and flows downwards under gravity, leaving the casing via the liquid outlet.

As equipment for efficient multi-phase mixing and mass transfer, (Yuan et al., 2022) identified RPB packing as its core component. Because of its excellent mass transfer characteristics, stainless steel wire mesh is commonly used as RPB packing (Chen et al., 2006). Conventional packed beds have constant cross-sections. Thus, their packing pores are nearly wholly filled throughout the column during flooding, causing a noticeable, steep rise in pressure drop.

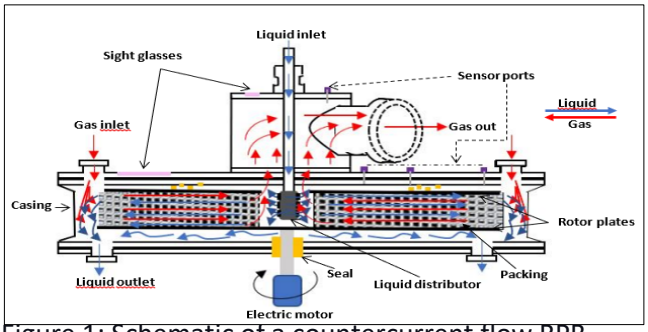

Figure 1: Schematic of a countercurrent flow RPB

However, due to the rotor geometry, RPB packings have variable cross-sections. The centrifugal forces are lowest at the center (eye) of the rotor. Hence, RPB flooding occurs in the eye from where the liquid is ejected. Consequently, pressure drop variations during flooding in RPBs are not consistent as the sole indicator of flooding. (Neumann et al., 2017a), and Lockett (Lockett, 1995) also reported that in contrast to conventional columns, for RPBs, no sharp inflection in the total pressure drop or the holdup of the liquid with the gas velocity was observed during flooding. The procedure for visually determining the upper operating limit is to neutralize two operating variables and manipulate the third one (Groß et al., 2018). Therefore, it is possible to carry out two procedures to reconfirm the results. The speed of the rotor and the liquid flow rate may be set to a constant value then the gas flow rate gradually increases until an excessive splash of the liquid is observed in the eye of the rotor. Allowing the gas flow rate to increase beyond the upper operating limit will cause the liquid to accumulate in the eye of the rotor. (Groß et al., 2018;

Neumann et al., 2017b) recommended the use of a combination of visual and quantitative approaches to adequately study the flow behavior in RPBs, while (Groß et al., 2018) observed that due to observed inconsistencies, the use of physical and visual observations and the measurement of pressure drop variations alone are not sufficiently adequate to predict flooding behavior in RPBs. (Burns et al., 2000) used liquid holdup, while (Hendry et al., 2020) measured the flow rate of entrained liquid from the eye of the rotor to identify the upper operating limits in RPBs.

2. MATERIALS AND METHODS/METHODOLOGY/EXPERIMENTAL PROCEDURE

The experimental setup is shown in Figure 2. The RPB was a pilot-scale RPB 500 from ProCeller® located at the Laboratoire de Génie Chimique (LGC) in Toulouse (France). The RPB was a single-stage, vertical rotor type with a casing diameter of 0.676m, an inner rotor diameter of 0.160m, and an outer rotor diameter of 0.500m. The packing was a conventional, multi-layered, single-block, stainless steel wire mesh with an axial height of 0.040m, a specific surface of 2400 m^2/m^3, and a porosity of 86%. Visual observation was possible using two inspection glasses placed directly above the eye of the rotor and another on the casing (Figure 3a). To aid the systematic collection and subsequent measurement of ejected water from the eye of the rotor during flooding, a hydrocyclone was connected to the gas outlet. A countercurrent air-water system was used for all the experiments. The rotation speed of the rotor was selected and auto-controlled via a variable frequency drive. The liquid was pumped to the RPB using a peristaltic pump and controlled with a valve. The liquid flow rate was measured with a panel-type rotameter and sprayed from the center of the RPB using a dual nozzle, flat fan liquid distributor. The liquid was recirculated to the feed tank using a bypass line. An air supply from the general laboratory compressor was used. The gas was introduced into the outside of the RPB into the casing through twin gas inlets and leaves after passing through the packing via the gas outlet. While the liquid sprays outwards from the center of the packing to its periphery. A pressure sensor connected to a pressure transmitter was placed across the two points to measure the pressure drop between the packing periphery and the gas outlet. Pressure drop was measured in real time by interfacing the sensor to a computer using a data acquisition system.

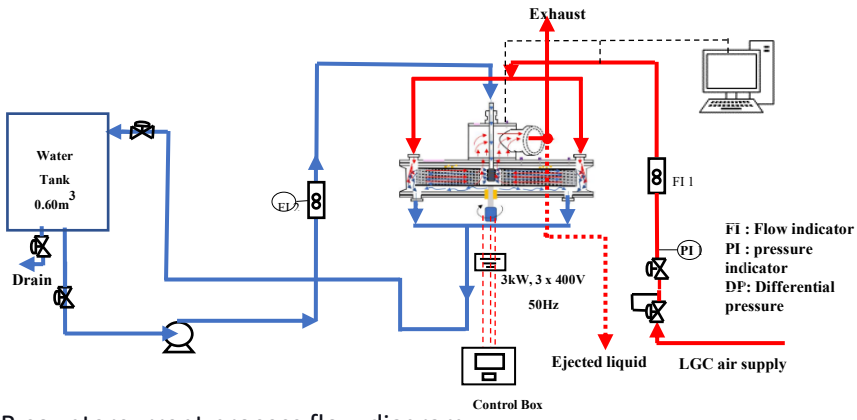

Figure 2: RPB countercurrent process flow diagram

The range of operating parameters studied was: gas flow rate (V_G), 0-400Nm^3/h; liquid flow rate (V_L), 0-0.75m^3/h and rotation speed 0-1500 revolutions per minute (RPM). Each experimental run was for 5 minutes. In the dry pressure drop measurements, the frictional pressure drop was first measured by passing air at 100Nm^3/h through the stationary rotor and then measuring the pressure drop. The experiment was repeated by increasing the airflow rate in steps of 50Nm^3/h. The same procedure was repeated with the rotor at various rotation speeds. Next, the effect of the rotation speed was investigated, initially via the centrifugal pressure drop. Without liquid and gas flow, the rotor was set to an initial speed of 100 rpm. The rotation speed was subsequently changed stepwise. The effect of rotation speed was further investigated by varying the rotation speed at constant gas flow rates. For the wet pressure drop, rotation speeds and liquid flow rates were kept while the gas flow rate was increased stepwise. This was followed by another set of experiments during which the gas flow rate and rotation speed were kept constant while the liquid flow rate was increased. The liquid flow rate and rotation speed were kept constant to determine the upper operating limit. In contrast, the gas flow rate was increased stepwise until the first drops of water were observed from the gas outlet according to the arrangement shown in Figure 3e. This point was taken as the upper operating limit of the RPB at the prevailing combination of operating factors. The reduction in rotation speed was continued gradually, with the amount

of ejected water measured at each step after attaining a steady state of operation. Flooding points of the RPB operations were determined by visual observation of excessive water splashing at the RPB eye, with or without a sharp increase in pressure drop. The volume of water ejected at each step change of the gas flowrate was collected and measured using a measuring cylinder, and the flooding point was taken following the recommendation of (Hendry et al., 2020) when,

$$flowrate\ of\ ejected\ liquid \geq 8\%\ liquid\ flowrate \quad (1)$$

3. RESULTS AND DISCUSSION

Figure 4(a) shows that dry pressure drop increases with increased rotor speed. A slow increase in pressure drop was obtained at low rotational speeds from 100 to 550 RPM. Above 600 RPM, a rapid and almost linear increase in pressure drop was obtained. This phenomenon may be due to the greater need to overcome the pressure drop caused by rotation (centrifugal head) at higher rotational speeds, which consequently causes the air in the rotor and between it and the casing to rotate. The dry bed average increase in pressure drop per unit increase in rotation speed in the range investigated was 0.75Pa/rpm. This shows that centrifugal pressure contributes significantly to the total dry-packing pressure drop. Figure 4(b) also shows a substantially linear increase in pressure drop with increasing gas flow rate. The effects of gas inertia and friction primarily cause this. On average, Figure 4(b) shows that the average increase in pressure drop per unit increase in gas flow rate was 4.11Pa/Nm^{3}h^{-1} within the operating range investigated.

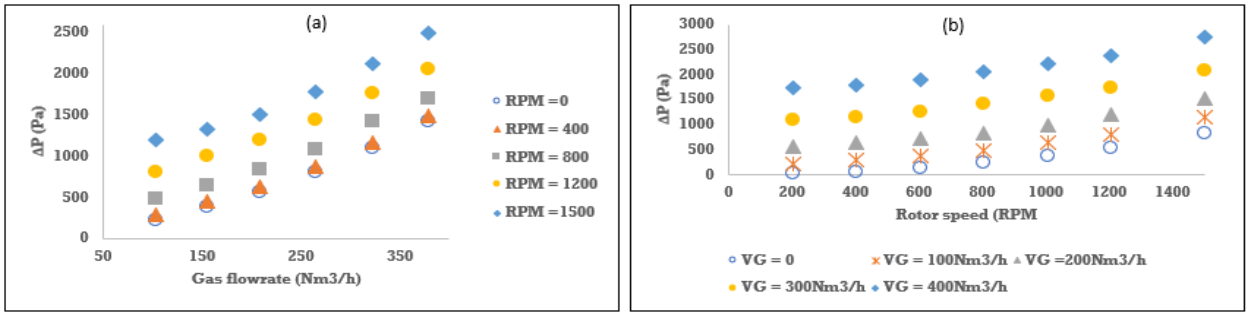

Figure 3: Dry bed pressure drop (a) effect of rotation speed (b) effect of gas flowrate

By comparing Figures 4(a) and (b), it can be seen that based on the sensitivity analysis mentioned above, the gas flow influences the dry pressure drop of the RPB more than the rotational speed. It can be deduced from figures 4(a) and (b) that the range of dry pressure drops (20-2800Pa) in this work was comparable to the range obtained by (Liu et al., 2018) for the same range of rotation speed and comparable gas loads. The result is also comparable to that of (Neumann, Hunold, Skiborowski, et al., 2017) of 20-750Pa for similar rotation speed, RPB, and packing characteristics but using a lower gas flow rate of 15-60m^3/h. For the irrigated bed, Figures 5(a) and (b), as well as Figure 6(a), showed that the trend of the pressure drop variation was almost the same as that of the dry bed, with the pressure increasing with an increase in rotational speed and with the gas flow. (W. Zhang et al., 2020) identified the wetting of the packing surface, which affects the frictional pressure drop, and the blockage of the packing pores by the liquid to the passage of gas as the two principal contributors to the rise in pressure drop in wet RPBs. Figure 6(b) indicates the lower effect of liquid flow rate on the overall pressure drop in RPBs. For example, for a gas flow of 350Nm^3/h, the 50% increase in liquid flow rate from 0.3 to 0.6m^3/h produces small changes in the pressure drop with the increase in the speed of rotation, showing that the effect of the gas flow in the RPB is more than that of the liquid flows. This phenomenon is more visible when we represent this at constant rotational speeds with a variation of the gas flow (Figure 5a) or a variation of the liquid flow (Figure 5(b)). These results confirm the trends described by the reports of (Groß et al., 2018; Neumann, Hunold, Groß, et al., 2017). Additionally, in terms of liquid loading loads and gas capacities, it can be deduced that the ranges of the wet pressure drops in Figures 6(a) and (b) are comparable to the findings of (Liu et al., 2018).

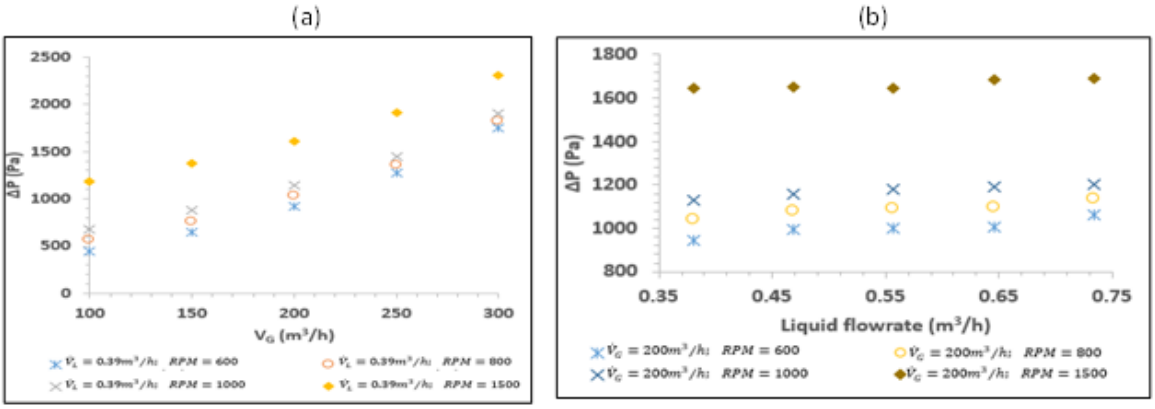

Figure 4 (a)Dry pressure drop increases with increased rotor speed. (b) Average increase in pressure drop per unit increase in gas flow rate.

Figure 4 (a) shows that the flooding data follows a typical RPB equipped with a vertical axis pressure drop variation curve with rotation speed at constant gas and liquid flow rates, as highlighted by (Neumann, Hunold, Groß, et al., 2017). A lowering of centrifugal pressure drop is obtained at a decrease from the maximum rotation speeds. At the same time, liquid accumulation in the eye causes only slight increases in frictional pressure drop. Further decrease in the rotation speed will cause an accumulation of liquid in the eye of the rotor, which leads to an increase in the frictional pressure drop and a sharp increase in the total pressure drop.

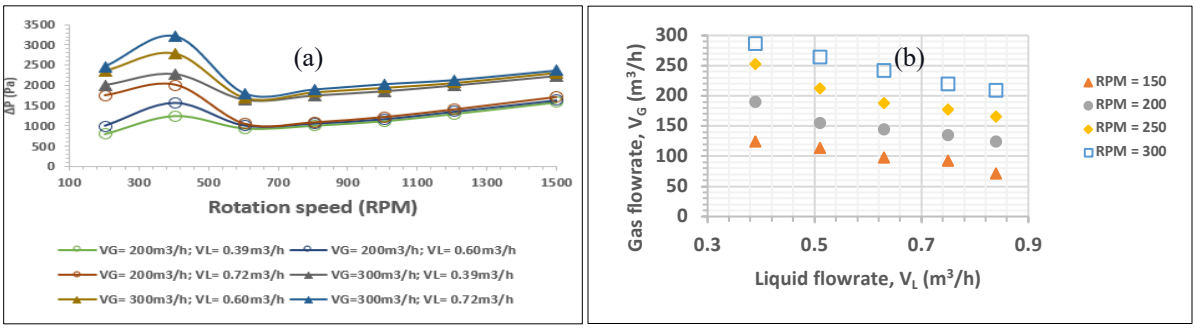

Figure 5 (a) Effect of rotation speed at constant gas and liquid flow rates (b) upper operating points.

As the rotation speed is further decreased, rapid ejection of liquid from the eye of the rotor to the gas outlet is obtained due to the acceleration of the liquid droplets. The pressure drop increases significantly, and the presence of water is visually observable in the rotor eye. Figure 6(b) shows the upper operating limits of the system investigated. At a constant rotation speed, the gas flow rate at which the ejection of liquid droplets was observed and decreased with an increased liquid flow rate. Regular operation of the RPB without liquid ejection and possible high-pressure drops, which increase power consumption, is obtained by operating the RPB below the indicated points. The operating limit at a given condition can be improved by increasing the rotation speed from the given point. Based on a range of liquid loads and the gas capacity factor at the inner radius of the RPB, the trends and ranges of these operating limits are comparable to the results of (Groß et al., 2018).

4. CONCLUSIONS

This paper focused on furthering the understanding of the upper operating limits of RPBs as an essential aspect of its design, modeling, scale-up, and use for the intensification of mass transfer processes. The gas pressure drop of a pilot-scale RPB equipped with stainless steel wire mesh packing for an air-water system using a twin-nozzle liquid distributor was explored. A robust approach to determine RPB operating limits based on quantifying the volume of liquid ejected from the eye of the rotor was explored. The operating limits for RPBs are influenced mainly by the three operational parameters: gas flow rate, liquid flow rate, and rotational speed in that order.

ACKNOWLEDGMENT

This work was conducted under support funding from the Overseas Scholarship Scheme (OSS) of the Petroleum Technology Development Fund (PTDF), Nigeria (Grant Number: PTDF/ED/OSS/PHD/UG/1543/19).

REFERENCES

Adekola L., Meihong W., Peter S, O. O. (2012). Demonstrating full-scale post-combustion CO2 capture for coal-fired power plants through dynamic modelling and simulation. *Fuel*, *101*, 115–128.

Burns, J. R., Jamil, J. N., & Ramshaw, C. (2000). Process intensification: Operating characteristics of rotating packed beds - determination of liquid hold-up for a high-voidage structured packing. *Chemical Engineering Science*, *55*(13), 2401–2415. https://doi.org/10.1016/S0009-2509(99)00520-5

Burns, J. R., & Ramshaw, C. (1996). Process intensification: Visual study of liquid maldistribution in rotating packed beds. *Chemical Engineering Science*, *51*(8), 1347–1352. https://doi.org/10.1016/0009-2509(95)00367-3

Chen, Y. S., Lin, F. Y., Lin, C. C., Tai, C. Y. Der, & Liu, H. S. (2006). Packing characteristics for mass transfer in a rotating packed bed. *Industrial and Engineering Chemistry Research*, *45*(20), 6846–6853. https://doi.org/10.1021/ie060399l

Cheng, H. H., & Tan, C. S. (2011). Removal of CO2 from indoor air by alkanolamine in a rotating packed bed. *Separation and Purification Technology*, *82*(1), 156–166. https://doi.org/10.1016/j.seppur.2011.09.004

Groß, K., Neumann, K., Skiborowski, M., & Górak, A. (2018). Analysing the operating limits in high gravity equipment. *Chemical Engineering Transactions*, *69*, 661–666. https://doi.org/10.3303/CET1869111

Hendry, J. R., Lee, J. G. M., & Attidekou, P. S. (2020). Pressure drop and flooding in rotating packed beds. *Chemical Engineering and Processing - Process Intensification*, *151*(March), 107908. https://doi.org/10.1016/j.cep.2020.107908

Hilpert, M., & Repke, J. U. (2021). Experimental Investigation and Correlation of Liquid-Side Mass Transfer in Pilot-Scale Rotating Packed Beds. *Industrial and Engineering Chemistry Research*, *60*(14), 5251–5263. https://doi.org/10.1021/acs.iecr.1c00440

Jiao, W. Z., Liu, Y. Z., & Qi, G. S. (2010). Gas pressure drop and mass transfer characteristics in a cross-flow rotating packed bed with porous plate packing. *Industrial and Engineering Chemistry Research*, *49*(8), 3732–3740. https://doi.org/10.1021/ie9009777

Liu, X., Jing, M., Chen, S., & Du, L. (2018). Experimental study of gas pressure drop in rotating packed bed with rotational-stationary packing. *Canadian Journal of Chemical Engineering*, *96*(2), 590–596. https://doi.org/10.1002/cjce.22936

Lockett, M. J. (1995). Flooding of rotating structured packing and its application to conventional packed columns. *Chem. Eng. Res. Des.*, *73*, 379–384.

Neumann, K., Gladyszewski, K., Groß, K., Qammar, H., Wenzel, D., Górak, A., & Skiborowski, M. (2018). A guide on the industrial application of rotating packed beds. *Chemical Engineering Research and Design*, *134*, 443–462. https://doi.org/10.1016/j.cherd.2018.04.024

Neumann, K., Hunold, S., Groß, K., & Górak, A. (2017a). Experimental investigations on the upper operating limit in rotating packed beds. *Chemical Engineering and Processing: Process Intensification*, *121*(August), 240–247. https://doi.org/10.1016/j.cep.2017.09.003

Neumann, K., Hunold, S., Skiborowski, M., & Górak, A. (2017b). Dry Pressure Drop in Rotating Packed Beds - Systematic Experimental Studies. *Industrial and Engineering Chemistry Research*, *56*(43), 12395–12405. https://doi.org/10.1021/acs.iecr.7b03203

Pan, S. Y., Wang, P., Chen, Q., Jiang, W., Chu, Y. H., & Chiang, P. C. (2017). Development of high-gravity technology for removing particulate and gaseous pollutant emissions: Principles and applications. *Journal of Cleaner Production*, *149*, 540–556. https://doi.org/10.1016/j.jclepro.2017.02.108

Pyka, T., Koop, J., Held, C., & Schembecker, G. (2022). Dry Pressure Drop in a Two-Rotor Rotating Packed Bed. *Industrial & Engineering Chemistry Research*. https://doi.org/10.1021/acs.iecr.2c02500

Singh, S. P., Counce, R. M., Wilson, J. H., Villiers-Fisher, J. F., Jennings, H. L., Lucero, A. J., Reed, G. D., Ashworth, R. A., & Elliott, M. G. (1992). Removal of Volatile Organic Compounds from Groundwater Using a Rotary Air Stripper. *Industrial and Engineering Chemistry Research*, *31*(2), 574–580. https://doi.org/10.1021/ie00002a019

Xie, P. (2019). *Hydrodynamics and Mass Transfer of Rotating Packed Beds for CO 2 Capture*. *February*.

Yuan, Z.-G., Wang, Y.-X., Liu, Y.-Z., Wang, D., Jiao, W.-Z., & Liang, P.-F. (2022). Research and development of advanced structured packing in a rotating packed bed. *Chinese Journal of Chemical Engineering*, *49*, 178–186. https://doi.org/10.1016/j.cjche.2021.12.023

Zhang, L. L., Wang, J. X., Xiang, Y., Zeng, X. F., & Chen, J. F. (2011). Absorption of carbon dioxide with ionic liquid in a rotating packed bed contactor: Mass transfer study. *Industrial and Engineering Chemistry Research*, *50*(11), 6957–6964. https://doi.org/10.1021/ie1025979

Zhang, W., Xie, P., Li, Y., Teng, L., & Zhu, J. (2020). Hydrodynamic characteristics and mass transfer performance of rotating packed bed for CO2 removal by chemical absorption: A review. *Journal of Natural Gas Science and Engineering*, *79*(March), 103373. https://doi.org/10.1016/j.jngse.2020.103373

PAPER 81 - EFFECTS OF AERO-ENGINE DEGRADATION ON SPECIFIC FUEL CONSUMPTION AT VARYING AMBIENT AND TURBINE INLET TEMPERATURES

I.O. OTAIKU[1], I. K. ADEGUN[2]

International Aviation College, Ilorin, Kwara State and Kwara State University
Department of Mechanical Engineering, University of Ilorin, Ilorin, Nigeria
Corresponding Author: olaoluwa.otaiku@gmail.com. +23460520474.

ABSTRACT

The paper presents the effects of aero-engine degradation on specific fuel consumption at varying ambient temperature and turbine inlet temperature. The ambient and turbine inlet temperatures were varied using analytically developed equations. These parameters with the specific fuel consumption, were modelled to determine the performance of the engine at each instance. A 4- stage compressor and a single stage turbine were investigated for 0 to 10% area reduction of the blades. Increase in degradation and margin to permanent failure were examined. The ranges of ambient and turbine inlet temperatures and TIT considered were 295 to 325 K and 1083-1245 K respectively. specific fuel consumption against ambient and turbine inlet temperatures, mass flow rate and net power produced at each level of blade degradation were plotted. Results showed that for undegraded compressor blades, the changes in the ambient did not have significant effect on the compressor's exit temperature. However, at 8% blade degradation, the effect was noticeable and became risky at 10%, where the exit temperature seemed to be increasing beyond tolerable temperature of the material. It was also observed that SFC increased with increasing TIT. The results predict that margin to permanent failure of the engine would occur at 10% compressor's blade degradation when the SFC would have risen to 0.5 kg/kWh, ABT (315 K), TIT (1100 K) and fuel flow rate at 0.4 kg/s. In conclusion, to prevent complete engine-out, the revolution per minute of the engine at these conditions should be reduced to 80% and landing procedures initiated.

KEYWORDS: Specific fuel consumption (SFC), ambient temperature (ABT), turbine inlet temperature (TIT) and surface area degradation.

1. INTRODUCTION

The interpretation of the degraded engine performance has been reported by De Castro-Cros et al. (2023) that SFC is one of the parameters to depict an engine nearing an end to active service life cycle. Therefore over-fuelling during different phases of flight especially climb for a degraded engine could cause high temperature and thermal shock which is undesirable at such phase because it increases the fatigue due to centrifugal stress on the engine and can accelerate the deteriorating operation of the compressor close to the choking condition or surge (Kolias et al., 2021). If no remedy is quickly applied at the instance of transient or dynamic condition, compressor operating condition will move the engine from large to very small margin to surge that can result to complete flame out and badly damaged engine (ATSB, 2014). The aim of this study is therefore to carry out an analytical modelling by developing equations for the rate of change of SFC during the engine degradation relative to varying ambient and turbine inlet conditions.

1.1.Turbomachinery of the Compressor and the Turbine

Deterioration of aero-engine gas turbine blades affects their exit angles, length and other parameters of the blade profile which will definitely result to increase in unexpected losses. It has been reported by Otaiku and Adegun (2021); Kurzke, J.; Halliwell (2018); Alexiou (2020); Aungier (2003) and Zhang et al. (2020) that the main influence of degradation appears around the optimum incidence angles. If the leading edge of the blades experience above 10.04 mm crack or fracture according to AMM (P & W 2014), there will be increase in flow of air/gas thereby over building up the pressure within the control volume above the specified range (choked condition) and causing a progressive turbulent flow and negatively affecting the work output and efficiency of the engine. As long as this new condition persists, the rotational speed of the driving shaft will definitely reduce performance until the process eventually move from turbulent flow to separation of flow around the degraded blades (Hendricks 2016) with significant loss in aerodynamic property of the airfoil blade. It should be noted at this point that in the compressor section, ambient air temperature plays a vital role in the exit temperature of the compressor. So, at higher ambient temperature for a degraded blades in the compressor, the greater the compression ratio and the more the fuel being consumed at the combustion section due to reduction in the effective (pressure) surface area of the blades and blockages according to

Otaiku and Adegun (2023). For an ideal engine, by assuming a constant temperature rise across all the stages in the compressor, the ambient temperature ranges do not significantly affect the compressor exit temperature when the aforementioned condition apply. But in cases of engine degradation, where the temperature per stage depends on the condition of the blades per stage, then one can expect a paradigm shift of the general assumption and determination of effect of ambient temperature on degraded blades per stage in the compressor and turbine is imperative. reason why this study is carried out.

1.2 Literature Review

Singh et al. (1999) presented a model and sample calculations for the deterioration of three different single stage compressors. The presented model included the effects of increased roughness and tip clearance due to erosion, resulting to losses and poor performance of the engine. However, they omitted the amount or percentages of surface area reduction due to reducing length of the blades that cause the losses. This gap has been adequately covered in this study.

De Castro et al. (2023) carried out experimental study of the performance of the compressor at the degraded condition, their results showed how there is need to install autoencoder on the engine to help to define an indicator of the compressor behaviour in long-term performance. They analysed the condition and performance of a gas turbine after a maintenance operation using two different autoencoder architectures. Their results showed that there is need to install a fuel flow control system to maintain the fuel flow schedule such that the engine will not run into risky operating conditions due to change in fuel flow and increase in SFC for a degraded engine (e.g. where the compressor working line would cross the surge margin). Goeing et al. (2020); Srinival et al. (2018) and Xin et al. (2019) explained that the effect of compression ratio on compressor work is similar to turbine work. As the work increased with increase in the compression ratio, it was expected that the ambient temperature also increased. A low ambient temperature produced high air density and a high gas turbine compressor work and output power and also a higher SFC.

Bayona-Roa et al. (2019); Liu et al. (2021) and Egorov et al. (2018) carried out experimental and numerical work on degraded blades' performance of the aero-engine with variation in ambient temperature as a function of compressor work output thereby significantly affecting the thermal efficiency of the engine. As the ambient temperature increased, the thermal efficiency decreased. This was because, the air mass flow rate inlet to compressor increased with decrease of the ambient temperature. Their result showed that at 90% design speed, the losses in efficiency and pressure ratio were high due to fractured area or the blade surface. It was also noticed that there was a reduction in efficiency of 22% as compared to that of on design configuration. Also, findings showed the total pressure, efficiency and the mass flow rate at the near stall condition at 80% design speed, as compared to the design point parameters. This study has clearly brought out that the margin to surge in the compressor stage was any speed less than 85% of the design speed.

Foorozan et al. (2015) explained that the compressor and turbine mass flow rates varied similarly to the fuel consumption rate. That is, the transient response that existed in the compressor as the blade deteriorated, caused the mass flow to reduce and fuel flow becoming higher thereby consuming more than necessary.

2. THEORETICAL ANALYSIS

For a given speed of a degraded compressor and turbine, higher temperature and an increased axial velocity component will emerge because of reduced pressure. The equation for such pressure is as shown in Equation 1:

$$p=\rho RT \quad (1)$$

Inlet conditions, such as total inlet pressure, total inlet temperature (ambient temperature), inlet Mach number, and the inlet flow angle are calculated as given in Equations 2 and 3. The Inlet static pressure, inlet static temperature and inlet speed of sound can be found using isentropic relationships as shown in Equations 4-7 (Cohen et al., 1996; Farokhi, 2013 and Saravanamuttoo et al., 2009)).

$$P_t = P_1\left(1+\frac{\gamma-1}{2}M^2\right)^{\frac{\gamma}{\gamma-1}} \quad (2)$$

$$T_t = T_1\left(1+\frac{\gamma-1}{2}M^2\right)^{\frac{\gamma}{\gamma-1}} \quad (3)$$

Where Pt is the inlet total pressure, Tt is the inlet total temperature, P1 is inlet static pressure, T1 is inlet static temperature, γ is the specific heat ratio, and M is the inlet Mach number which is usually < 1.

The relative velocity VR of the flow over the blade, inlet speed of sound and the Mach number relationship are as given in Equations 4-6.

$$V_R = Ma \quad (4)$$

$$a = \sqrt{\gamma RT} \quad (5)$$

$$V_R = M\sqrt{\gamma RT} \quad (6)$$

The mass flow of air/gas in the compressor and turbine is as given in Equation 7.

$$\dot{m}_a = \rho AV \quad (7)$$

From the first law of thermodynamics and the Euler turbine equations, the work done W, enthalpy h, absolute velocity V and the relative total temperature ratio are as shown in Equations 8 -9. Also, from the Euler turbine equation, work in terms of wheel speed, relative velocity, and absolute velocity is as given in Equation 9.

$$W = \left(h_2 + \frac{V_2^2}{2}\right) - \left(h_1 + \frac{V_1^2}{2}\right) \quad (8)$$

$$W = \frac{1}{2}[(U_2^2 - U_1^2) - (V_{R2}^2 - V_{R1}^2) - (V_2^2 - V_1^2)] \quad (9)$$

where h_1 and h_2 are enthalpy at the inlet and exit respectively, V_1 and V_2 are absolute velocity at the inlet and exit, respectively. Where U_1 and U_2 are wheel speed at the inlet and exit, respectively. If we set equations 8 and 9 as equal to each other, the absolute velocities cancel out. From the velocity triangles as presented by Farokhi, (2013) and Saravanamuttoo et al., (2009) the stagnation temperature at the compressor or turbine can also be obtained from Equation 10.

$$T_t = T_1 - \frac{U^2}{2c_p}\left\{\frac{\Delta h}{U^2} + 1 - 2R_n\right\} \quad (10)$$

3. METHODOLOGY

The thermodynamic and Euler equations as shown in the previous section were further remodified to suit the assumptions made in this study. The new equations developed is derived from the fundamental equations and key parameters such as SFC, mass and fuel flow rates, engine efficiency and power at different shaft speed were obtained as analytical data and further plotted for explicit presentation. This is also shown in the Appendix A.

3.1. Preliminary Assumptions

a. Ideal gas properties and Sea level static (SLS) conditions for compressible fluid were considered and the compression and the expansion are adiabatic and isentropic.

b. Rate of change of density equals zero.

c. Axial directional flow was considered (x-direction).

d. NACA 65-(18)10 model was adopted for developed blade models.

e. 0 to 10% reduction in original blade area was assumed to be radial for rotating condition and elongation or blade fracture was vertically from the tip to the hub.

f. The heating value of the fuel is 43MJ/kg.

The degraded blade region is as shown in Figure 1 b and c.

3.1.1. Governing Equations

The unsteady 3-D flow of compressible fluid in compressor and turbine sections can be converted to 1-D to form the conservation of mass and energy as shown in Equations 11 a, b and 12.

3.1.2. Conservation of Mass

$$\frac{\partial \rho}{\partial t} + \frac{\partial}{\partial t}\rho u + \frac{\partial \rho}{\partial t}\rho v + \frac{\partial \rho}{\partial t}\rho w = 0 \quad 11a$$

$$\frac{\partial \rho}{\partial t} + \nabla.(\rho V) = 0 \quad 11b$$

Where velocity field vector in v and w = 0

Conservation of Energy

$$\frac{\partial \rho e}{\partial t} + \nabla.(\rho e V) \quad 12$$

3.1.3. Determination of Damaged Blade Surface Area

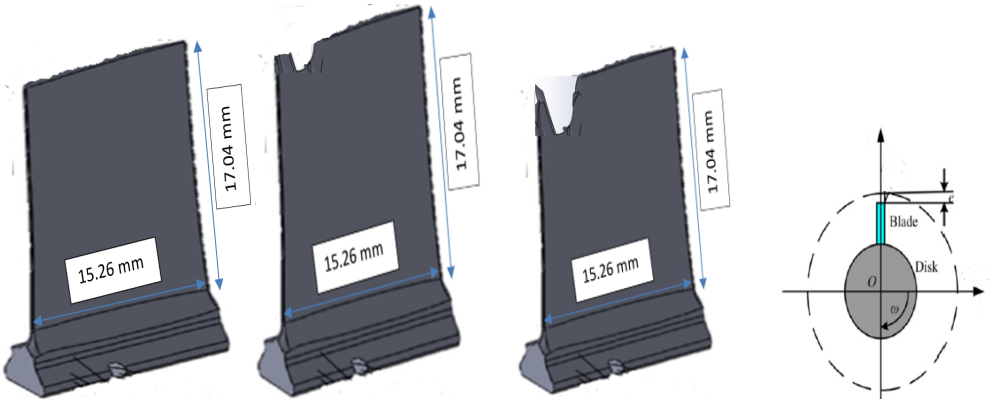

a. 0% undegraded blade b. 8% degraded blade and c. 10% degraded blade. d. Blade on the turbine disk.

Figure 1: Blade Specimen

3.2 Rotating Blade (without degradation or 0%).

The Figure 1 d shows the mounted blade on the disk and as given in the assumption, the radius of the blade with changing length is as shown in Equations 13 and 14.

radius at the tip $r_0^i = \frac{1}{2} l_0(t) + r_0(t)$ 13

- radius at the root $r_h = r_0(t)$ 14

3.2.1. Rotating Blade (8 to 10% degradation in surface area)

The new radius at the tip of the leading edge after fracture or break away is obtained from Equation 15.

$$r_{new}^i = \pi \left(\frac{1}{2}\bar{l}_{new} + r_0\right)^2 \quad 15$$

Based on the assumptions earlier stated and equations 11 a, b and 12, other fluid characteristics flowing around the rotating blades (0-10%) were derived as shown in Equations 16-17.

Note: The blade parameters were obtained by the empirical calculations and used for its development using SOLIDWORKS 20.

3.3. Derived analytical equation for the fluid

The law of conservation of mass from Equation 11 yields the mass flow rate, so for rotational transient conditions in x- direction (AL-Luhaibi and Tariq (2014)),

$$\dot{m}_{in} = \dot{m}_{out} = \rho\, V_{a1}\, \pi \left(\frac{1}{2}\bar{l}_{new} + r_0\right)^2 = \rho V_{a2}\, \pi \left(\frac{1}{2} l_0(t) + r_0(t)\right)^2 \quad 16$$

Multiplying linear velocity u with Equations 11 and 12 yields conservation of momentum is equal to conservation of energy rate

$$(\dot{\rho}ue + \rho\dot{u}e)V = (\dot{\rho}u + \rho\dot{u})V \quad 17$$

Also, derived equations for net power $\dot{W}$ and Torque τ are derived from Equation 17 to yield Equation 18

$$\dot{W} = P_t - P_c = \tau\omega = \dot{m}(U_1\Delta V_{\alpha 2} - U_2\Delta V_{\alpha 1}) \quad 18$$

3.4 Effect of density change on pressure change

General equations shown in Equations 1-7 for mass, density, pressure, temperature and Mach number are further modified to form Equations 19 -20 as required for this study.

- $$\rho = \frac{P_1\left(1+\frac{\gamma-1}{2}M^2\right)^{\frac{\gamma}{\gamma-1}}}{R\left(T_1\left(1+\frac{\gamma-1}{2}M^2\right)^{\frac{\gamma}{\gamma-1}}\right)} \quad 19$$

Mass flow rate for changing density and pressure with degraded blades

$$\dot{m_a} = \frac{P_1\left(1+\frac{\gamma-1}{2}M^2\right)^{\frac{\gamma}{\gamma-1}}}{R\left(T_1\left(1+\frac{\gamma-1}{2}M^2\right)^{\frac{\gamma}{\gamma-1}}\right)}\pi\left(\frac{1}{2}\bar{l}_{new} + r_0\right)^2 M\sqrt{\gamma RT_1\left(1+\frac{\gamma-1}{2}M^2\right)^{\frac{\gamma}{\gamma-1}}} \quad 20$$

3.5 Specific Fuel Consumption for degraded compressor and turbine blades

From Kolias et al. (2021); Henrique et al. (2020); Foroozan et al. (2013) Kurzke (2011); Saravarramutto (2014) and Farokhi (2013), SFC for the degraded sections is as given in Equation 21.

$$SFC = \frac{3600\,x\,m_f}{\dot{W}_{net}} \quad 21$$

$$\eta_{th} = \frac{\dot{W}_{net}}{LCV.m_f} \quad 22$$

From Equations 16 and 21 and based on the assumptions considered, Equation 23 was derived for change in Specific Fuel Consumption of the degraded engine as ambient and turbine inlet also change as $SFC =$

$$\left\{300 * \frac{mf}{c_p * \pi\rho_i V_{zi}\left[1+\frac{1}{\left(1+\frac{r_t}{r_h}\right)}\right]}\right\}/(T_1 + T_3 - (T_2 + T_4)) \quad 23$$

3.6. Thermal Efficiency

One other key parameter that should not be ignored is the thermal efficiency for the degraded engine. So combining Equations 16, 18 and 20, Equation 24 is obtained for thermal efficiency.

$$\eta_{th} = \frac{c_p * \pi\rho_i V_{zi}\left[1+\frac{1}{\left(1+\frac{r_t}{r_h}\right)}\right]}{LCV.m_f} \quad 24$$

Compressor: Ambient temperatures T_1 (288 to 343K), exit temperatures T_2 = 535 to 560 K. Turbine: Turbine Inlet Temperature was set between T_3 (1093 to 1245 K), exit temperatures T_4 = 870 to 1100 K.

4.0. RESULTS AND DISCUSSION

4.1.1. Compressor Section

The compressor section comprised a 3-stage axial, single stage centrifugal with rotor speed of 38,100 RPM and air pressure ratio of 7.7. The total inlet and outlet pressure, inlet and exit temperatures were 101325 Pa and 759937.5 Pa (shown in Figure 2), 298 to 325 K and 560-563 K from the entire compressor which will be presented graphically in

the next session. A typical value for the exit temperature of compressors is 560K as validated from Bela (2018) for a steady state compressor operation as represented in this study with 0% degradation. **T**emperature rise per stage was obtained to be 1.77 K and assumed to be constant across each stage. Taking the inlet total pressure as 101325 Pa for the damaged and undamaged blades, the compressor exit pressure for 8% and 10% reductions in surface areas were 8 MPa and 10 MPa with overall compressor ratio dropping from 7.7 to approximately 3.16 as shown in Figures 2, 3 and 4.

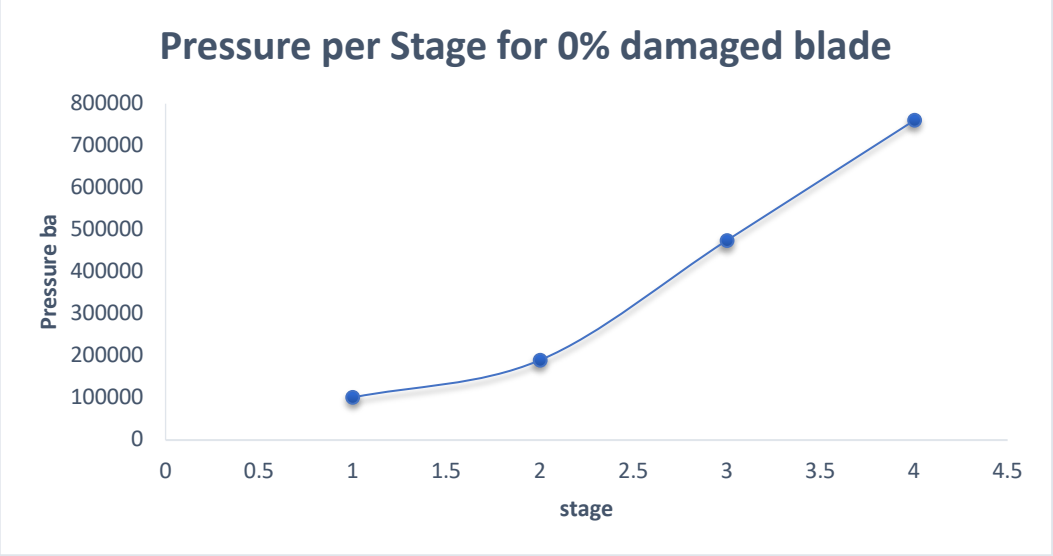

Figure 2: Pressure increase per stage for 0% degradation.

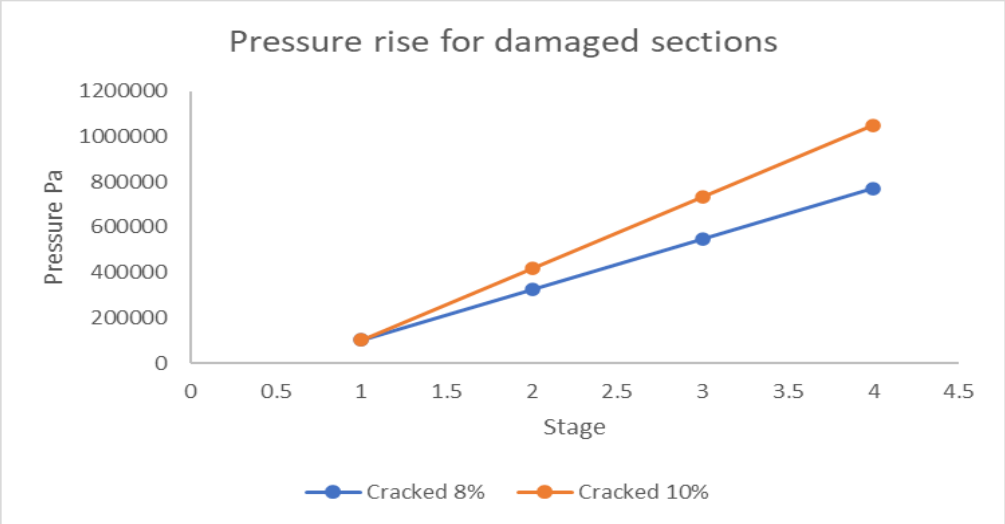

Figure 3: Pressure increase per stage for 8 and 10% degradation.

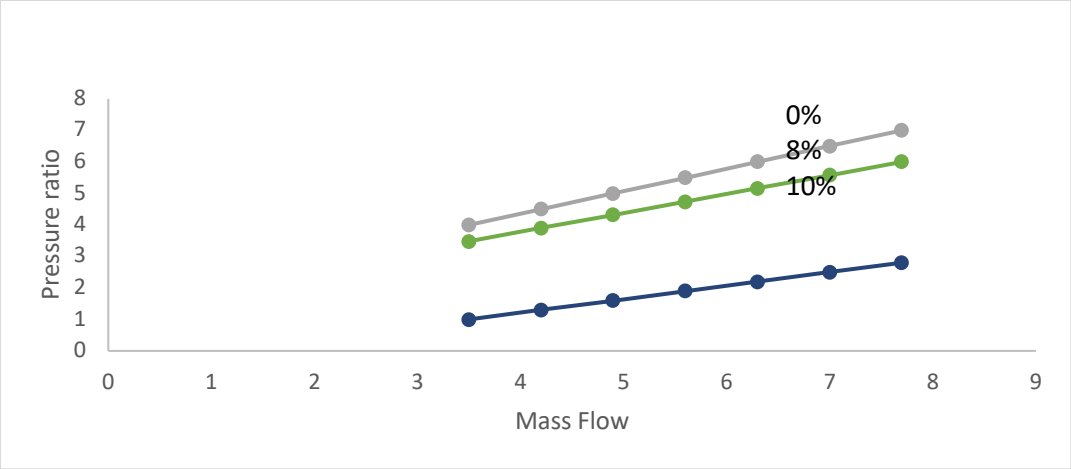

Figure 4: Pressure ratio vs mass flow rate

4.2. Effect of Change in Ambient Temperatures

Effect of ambient temperature on undegraded and degraded 4- stage compressor is as shown in Figures 5-6. For 0% degradation, the compressor exit temperature was obtained as approximately 563 K according to Figure 5 as validated from Bela (2018) which has earlier been mentioned. Particular attention is paid to the performance of the compressor as regards to actual temperature that was expected from the undegraded and degraded as shown in Figures 6 a and b respectively. The expected performance is that all the stages of the compressor and the turbine were working at their optimum efficiency point at design surge margins. But in the event of noticeable degradation, all the stages will start to work at off optimum surge margins and lower than design efficiency (Otaiku and Adegun, 2023 and De-Castro et al., 2023). Also, the losses will increase as the flow increases. However, if the degradation of the turbine section leads to material removal as been studied here and presented experimentally by Otaiku and Adegun, (2023), especially in the rotor area, the flow capacity increases for any given pressure ratio. Leading edge degradation in the turbine especially causes a shift in the distribution of pressure ratios i.e., a larger portion of the overall pressure ratio is consumed by the gas generator turbine (Bayona-Roa et al. (2019);Xin et al. (2019); Rahman and Whidborne (2008); Bonet and Pilidis(2013); Saravanamuttoo et al. (2009); Kurz et al. (2019); Cruz-Manzo et al. (2020); Kauth et al. (2019) and Goeing et al. (2020); Saravanamuttoo et al. 2009; Kurz et al. 2019). This causes a shift in the corresponding turbine inlet temperature to higher ambient temperatures as shown in Figures 6 a and b for 8 and 10% degradation.

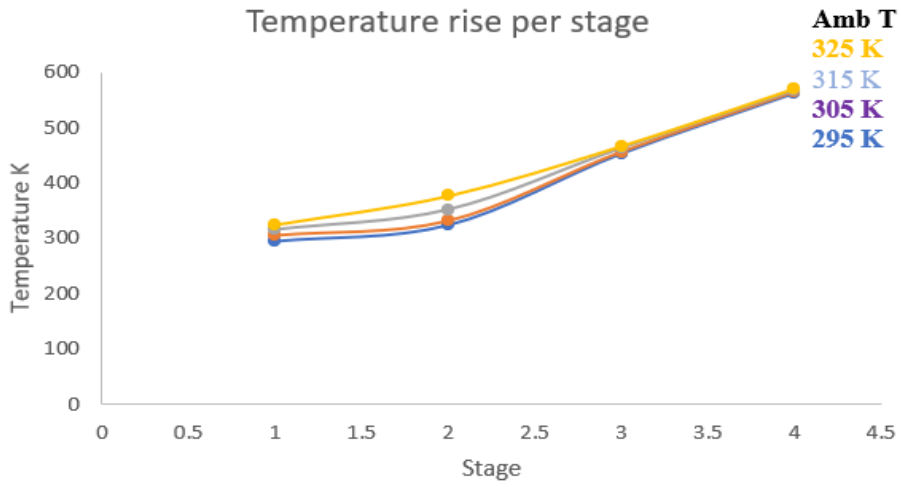

Figure 5: Ambient temperature change vs compressor exit temperature

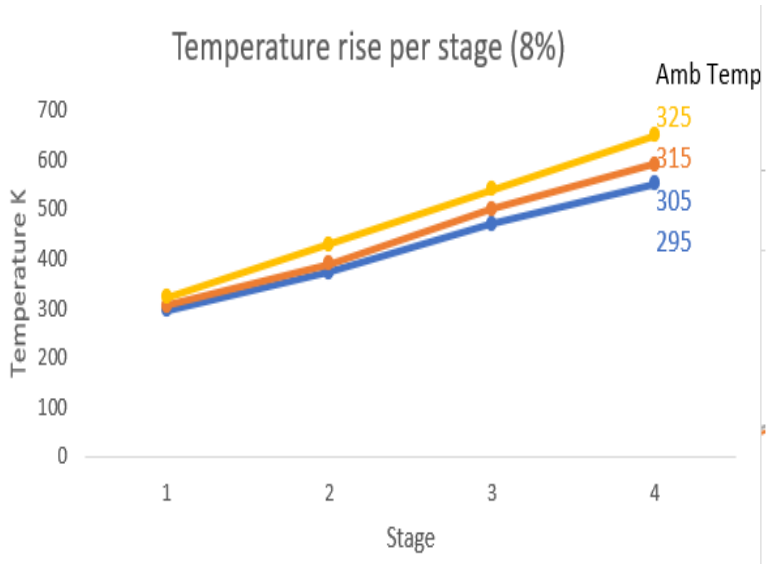

a. 8% degradation

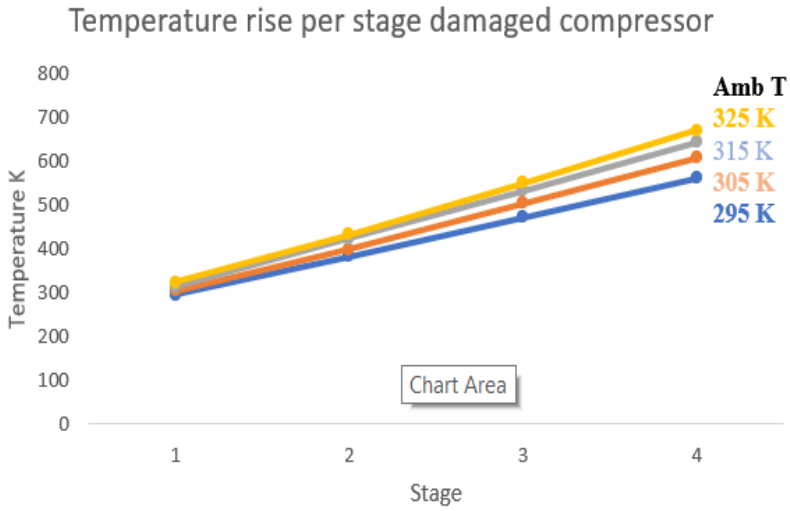

b. 10% degradation

Figure 6 a and b: Ambient temperature change with significant effect on compressor exit temperature.

4.3. Effect of Ambient Temperature on Specific Fuel Consumption and Turbine Inlet Temperature for degraded compressor and turbine.

Figure 6 shows the condition of the engine in terms of rate of specific fuel consumption with increasing ambient temperatures for 0, 8 and 10% reductions in blade length and surface area at both the compressor and the turbine. SFC obtained for 0% degraded blades was approximately 0.365 kg/kWh for ambient temperatures (295 to 315 K) and TIT 1083 K as shown in Figure 7. However, due to the degradations, the SFC will rise to 0.4 and 0.5 kg/kWh respectively as TIT increases as shown in Figures 7 and 8. Also, this will prompt the reduction in engine power from 1183 kW and continuously decreasing below 1000 kW which is already at surge margin (Figure 8). Of course, at these new conditions of the blades during climb, excessive fatigue is imposed on the engine as more SFC will be needed to augment the net power loss thereby allowing undesigned increase in PR for an increase in TIT as shown in Figure 9. This is a stage that a complete engine out is reached and the entire engine is already lost. These dynamic events are as shown in Figures 7 - 9.

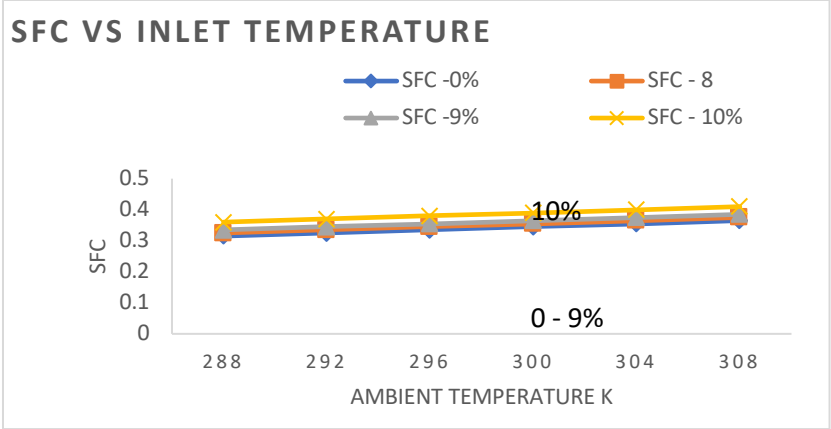

(a) SFC vs Ambient Temperatures

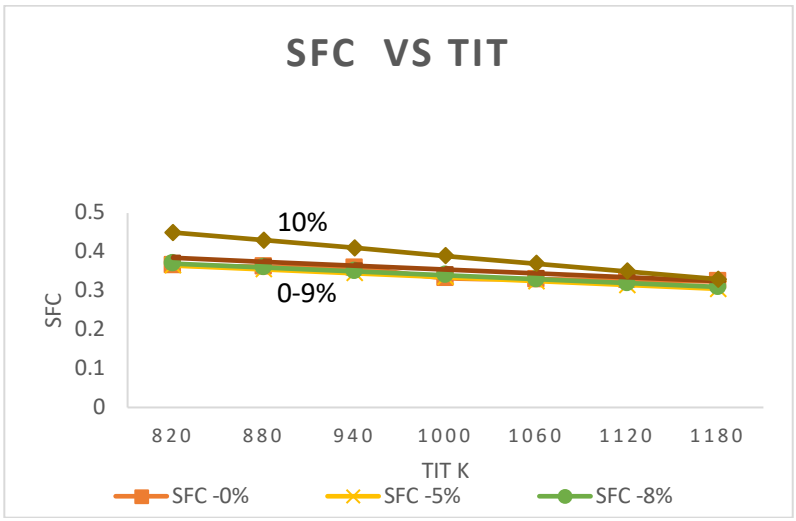

(b) SFC vs TIT

Figure 7 a and b: Change in ambient temperatures on SFC and TIT.

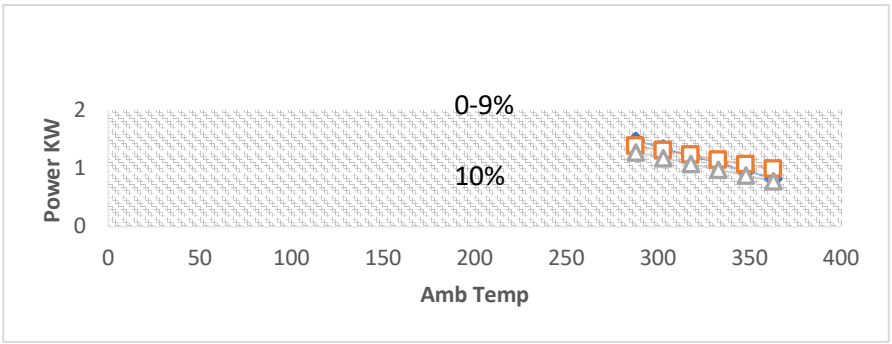

Figure 8: Change in power vs change ambient temperature

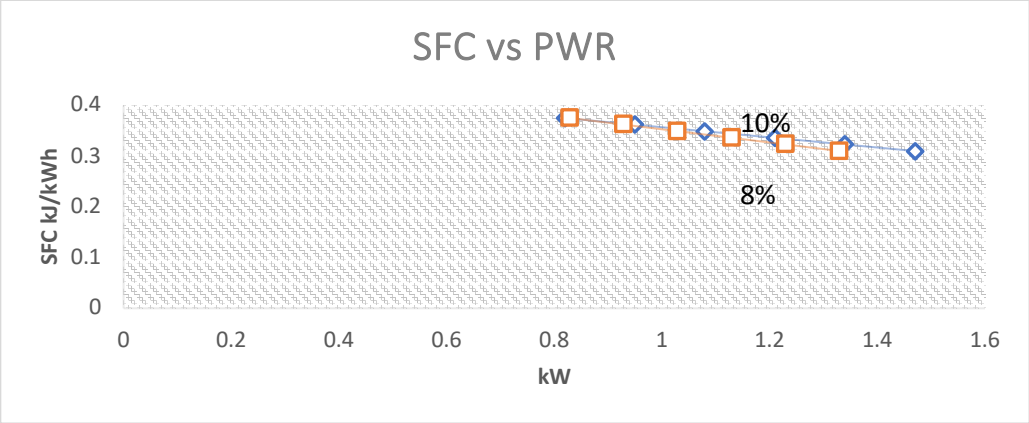

Figure 9: Increase in SFC vs decrease in power

4.4. **Effect of Pressure Ratio on Fuel Flow rate for change in Ambient Temperature**

As already being explained, the exit temperature of the compressor will definitely determine TIT that is the temperature leaving the combustion section (though not covered in this study). TIT according to the engine manufacturer must not exceed 1083 K for continued operation. However, going by this study, this condition will defiantly change due to change in the geometrical profile of the blade by reduction of it length and surface area which has been characterized as 8 and 10% degradation. Previously, the exit temperature increasing astronomically to maximum value of 600 and 750 K respectively at these new conditions. This transient response would increase as the deterioration continues. From Figures 10 and 11, the engine speed in RPM, pressure ratio, power, mass flow rate responses with the fuel flow rate and SFC which eventually result to surge at 10% reduction in surface areas of the blades in the compressor. The 10% area reduction and beyond showed that the turbine and compressor flow rates were non-uniform thereby aggravating the fuel flow in the combustion section.

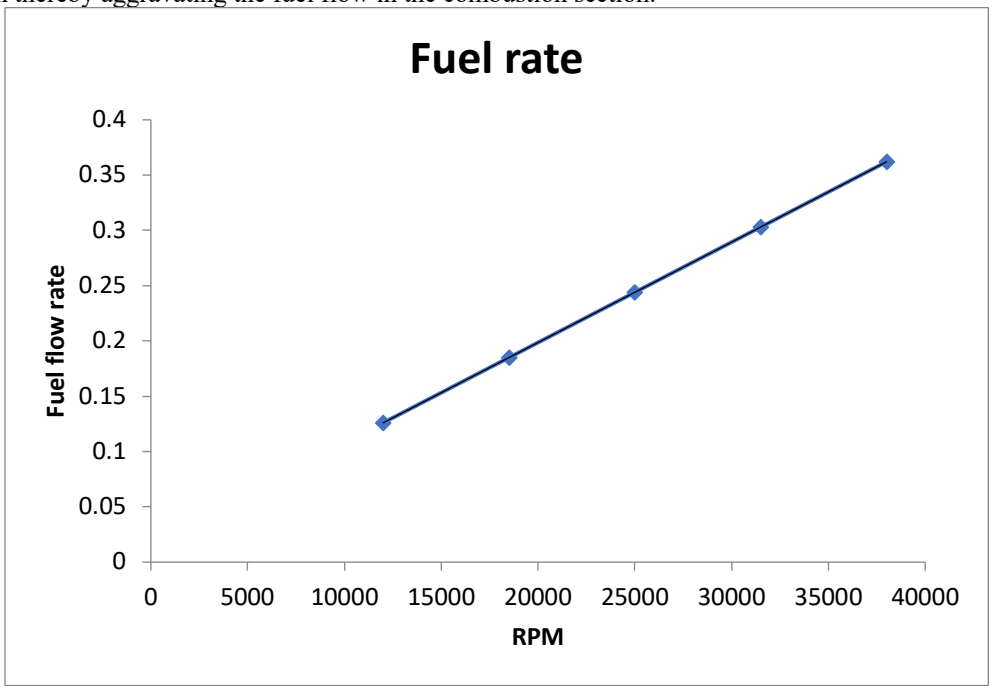

Figure 10: Increasing fuel flow rate with speed.

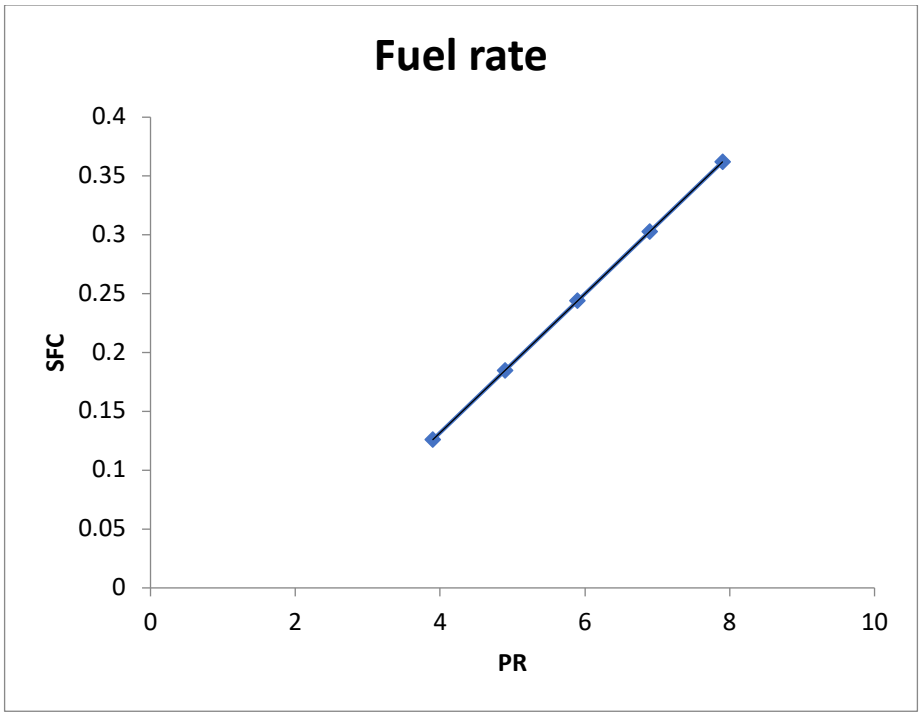

Figure 11: SFC increasing with PR

The resultant effect is that the specific fuel consumption SFC increases with the increase in ambient temperature. Under these abnormal conditions, losses in the burner section would be seriously noticed when the exit pressure and temperature at the compressor become higher for deteriorating engine thereby indicating a sudden increase in SFC an indication that the compressor section has been severely damaged (Moliere et al., 2020). This could have resulted from the blades crack or fracture as shown in the Figure 1 as earlier mentioned. The thermal efficiency also decreases with increase in air to fuel as corroborated by Rahman et al. (2011) and Moliere et al. (2020). This new development of the engine condition will cause choking at lower flow in both sections and a possibility of flow from the turbine back to the compressor a phenomenon called surge thereby shutting down the affected engine.

5. CONCLUSION

Effect of varying ambient and turbine inlet temperatures on specific fuel consumption for aero-engine with degraded blades have been studied and found to be significant. So effect of varying ambient temperatures for 8 – 10% blade surface area degradation of the compressor and turbine will affect the SFC, TIT, power output and the overall engine performance significantly especially at temperatures > 315 K. Compressor degradation usually cause higher power losses due to higher compressor exit temperatures as found to be between 600 and 700 K for 8 and 10% degradation respectively as against the validated value of 560 K which is categorized in this study as 0% degradation. Point of note is that SFC will increase with increasing turbine inlet temperature (TIT) particularly above 1100 K. The margin to permanent failure of the engine occurs at SFC of 0.4 kg/kWh, and TIT of 1100 K. Therefore operating the PT6T-turboshaft engine at these parameters could lead to permanent failure of the engine.

6. RECOMMENDATIONS

Therefore, from this study, the effect of degradation of blades up to 10% reduction in surface area has been studied and temperatures below 315 K ambient temperatures is somewhat recommended during flight to safely fly the aircraft to a final approach landing and should not exceed 315 K if the life of the engine is to be spared for the remaining stage of flight. In the event of stall before surge during flight operations, the maximum engine RPM should not exceed 80% and TIT not above 1092 K. However, if noticed on ground, whenever SFC is increased above the aforementioned values, the engine should be retired to the apron and internal failure of the blades should be ascertained and taking to the manufacturer for a complete replacement.

8. ACKNOWLEDGEMENT

The authors would like to thank University of Ilorin especially Profs, AGF Alabi, Aweda and Alao for their advisory role. Also worthy of note is Tgt. Rasheed from Kwara State for providing laboratory facilities for the simulation and experimental results respectively. Also, very special thanks to Petroleum Technological Development Fund (PTDF) for the financial support for my Ph.D work and Police Air Wing Abuja (ACP Ndubuisi and Engr. Cosmos Eze).

7. Conflict of Interest

The authors declare that no conflicting interest.

8. Data Availability

Operating data from the Aircraft Maintenance Manual from the manufacturer was used.

9. REFERENCES

De Castro-Cros, M.; Velasco, M.; Angulo, C. (2023). Analysis of Gas Turbine Compressor Performance after a Major Maintenance Operation Using an Autoencoder Architecture. Sensors 2023, 23, 1236. https://doi.org/10.3390/s23031236

Kurz, R.; Meher-Homji, C.; Brun, K.; Moore, J.J.; Gonzalez, F. (2013). Gas turbine performance and maintenance. In Proceedings of the 42nd Turbomachinery Symposium; Texas A&M University, Turbomachinery Laboratories: College Station, TX, USA, 2013.

Cheng, C.;Wang, J.; Chen, H.; Chen, Z.; Luo, H.; Xie, P. A (2021). Review of Intelligent Fault Diagnosis for High-Speed Trains: Qualitative Approaches. Entropy 2021, 23, 1.

Fu, S.; Zhong, S.; Lin, L.; Zhao, M. (2021). A re-optimized deep auto-encoder for gas turbine unsupervised anomaly detection. Eng. Appl. Artif. Intell. 2021, 101, 104199

Kurzke, J.; Halliwell, I. (2018). Propulsion and Power, An Exploration of Gas Turbine Performance Modeling, 1st ed.; Springer: Berlin/Heidelberg, Germany, 2018; ISBN 978-3-319-75977-7.

Alexiou, A. (2020). Introduction to Gas. Turbine Modelling with PROOSIS, 4th ed.; Empresarios Agrupados International (EAI) S.A.: Madrid, Spain, 2020.

Aungier, R.H. (2003). Axial-Flow Compressors, A Strategy for Aerodynamic Design and Analysis, 1st ed.; ASME: New York, NY, USA, 2003; ISBN 0-7918-0192-6.

Hendricks, E.S (2016). Meanline Analysis of Turbines with Choked Flow in the Object-Oriented Turbomachinery Analysis Code. In Proceedings of the 54th AIAA Aerospace Sciences Meeting, San Diego, CA, USA, 4–8 January 2016; AIAA-2016-0119.

Zhang, Y.; Zhang, S.; Xiao, Y. (2020). Aerodynamic Performance Prediction of Transonic Axial Multistage Compressors Based on One-Dimensional Meanline Method. In Proceedings of the ASME Turbo Expo 2020, Virtual, Online, 21–25 September 2020; GT2020-14571.

Srinivas G., Raghunandana K., and Shenoy B Satish (2018). Axial-flow compressor analysis under distorted phenomena at transonic flow conditions, Cogent Engineering, 5:1, 1526458, DOI: 10.1080/23311916.2018.1526458.

Kolias, I.; Alexiou, A.; Aretakis, N.; Mathioudakis, K. (2021). Axial Compressor Mean-Line Analysis: Choking Modelling and Fully-Coupled Integration in Engine Performance Simulations. Int. J. Turbomach. Propuls. Power 2021, 6, 4. https://doi.org/10.3390/ijtpp6010004.

Smith, S. L. (1999). "One-Dimensional Mean Line Code Technique to Calculate Stage-by-Stage Compressor Characteristics. " Master's Thesis, University of Tennessee, 1999.

Cohen H., Rogers G., and Saravanamuttoo H., (1996). Gas Turbine Theory. Longman Group Limited, fourth edition, 1996.

Onder Turan (2009). Compressor Effects on Specific Fuel Consumption of Kerosene-fueled Civil Turbofans. International Journal of Civil Aviation. ISSN 1943-3433 2009, Vol. 1, No. 1: E3 Aircraft Propulsion &Structure Maintenance Department, School of Civil Aviation, Anadolu University, PO Box 26470, Eskisehir, Turkey

APPENDICES

Nomenclature

A blade surface area, m2
Cp specific heat, J/(kg_K)
h total enthalpy,
m inlet mass flow, kg/s
p Pressure, Pa
Q heat energy, J
T Temperature, K
Tc static temperature, K
Tt total (or stagnation) temperature, K
V Velocity, m/s
F = thrust
FAR= fuel air ratio
h = specific enthalpy (kJ/kg)
LHV=lower heating value of fuel (kJ/kgK)
m = mass flow rate of fluid (kg/s)
*m*a = mass flow rate of air at inlet (kg/s)
*m*f = fuel mass flow rate (kg/s)
M = Mach number
p = total pressure (bar)
ps = static pressure (bar)
RpC = compressor pressure ratio (overall)
R = characteristic gas constant
s = specific entropy (kJ/kgK)
SFC= specific fuel consumption (kg/Nh)
T = total temperature (K)
Ts = static temperature (K)
TIT = turbine inlet temperature (K)
W = specific work (kJ/kg)

Greek Symbols

Δp = pressure loss
γ = specific heat ratio
ρ = density
η = efficiency (%)

Suffixes

a = air
amb = ambient
b = burner
g = gas
p = pressure

PAPER 82 – UNSTEADY PERFORMANCE OF DEGRADED COMPRESSOR AND TURBINE BLADES OF AN AERO-ENGINE AT VARYING AMBIENT AND TURBINE INLET TEMPERATURES

I.O. Otaiku[1], I. K. Adegun[2]

[1]International Aviation College, Ilorin, Kwara State and Kwara State University
[2]Department of Mechanical Engineering, University of Ilorin, Ilorin, Nigeria
Corresponding Author olaoluwaotaiku@yahoo.com. +23460520474.

ABSTRACT

The paper presents the modelling of unsteady performance of a degraded 4-stage compressor and single stage gas generator turbine blades of PT6T turboshaft aero-engine of a helicopter. The two sections were set as control volumes for analytical and numerical modeling. Numerically, The blade specimens (NACA 65 series) were developed using SOLIDWORKS 20 and simulations performed with FLUENT in ANSYS 20.0. The RANS (Reynolds-averaged Navier–Stokes) equations with Shear Stress Transport model SST (k-w) were chosen for the unsteadiness of pressure and temperature distributions over different levels of reductions in surface area of the blades' pressure side. 900 x 10^3 mesh elements size were selected and the boundary conditions-inlets for the two control volumes were 295-325 K and 1083 – 1245 K for compressor and turbine respectively. Analytically, equations for different levels of degradations (surface area reductions) were developed to determine their flow performance at new pressure and temperature for compressor and turbine with change in time and the corresponding rise in centrifugal stress. Results from FLUENT predicts the performance of the sections for 10% surface area reduction with complex structure in the turbulent flow imposes high fatigue stress, hence shows the highest closeness to surge margin. For the compressor, the result emphasizes the impact of inlet conditions on degraded blades over exit conditions. Also in the turbine, velocity contour shows adverse/backward flow as a result of high turbulence formation and rising fatigue due to change in exit pressure flow from stage to stage in the compressor. This exit pressure determines the TIT in the turbine which is a function of efficiency of the single stage gas generator turbine and is crucial to the overall efficiency of the engine and the safety of the engine as a whole. In conclusion, the inter-component flow behaviour between the degraded compressor and turbine as revealed in this study shows the near real-life situation of the engine performance. Summarily, the accurate engine life estimation can be deduced from TIT rising from 1100-1200 K and centrifugal stress 60MN/mm^2.

KEYWORDS: Specific fuel consumption (SFC), ambient temperature (ABT), turbine inlet temperature (TIT) and surface area degradation.

1. INTRODUCTION

1.1 The prediction of off-design steady and unsteady performance any gas turbine (industrial or aerospace) engines require the availability of compressor and turbine characteristics, which are pressure and temperature flow, pressure ratio and variation in their revolution per minute. Blades of the compressor and turbine sections operate at high temperatures and pressure depending on the materials they are made of and hence are capable to convert thermal energy into mechanical energy. During this process, the blades' mechanical properties are over-stretched beyond their design and manufacturing processes and therefore are bound to fail. This has been experimentally proven by the results presented by Otaiku and Adegun (2021). Failure of these blades while in operation have a negative impact on the engine performance and turbine efficiency. The aim and objective of this study is to model the performance of PT6T degraded engine and the impact of transient operations of a 4 stage compressor and single stage axial turbine under certain instance of changing temperatures at the compressor inlet/exit and the turbine inlet as the ambient pressure remains constant. Chernikov and Semakina (2023) used RANS SST model to predict the flow in a diffuser. Their results predicted 14% exhaust diffuser pressure recovery coefficient due to the complex vortex structure of the turbulent flow, which the ordinary Averaged Navier–Stokes equations could not resolve. The effect of compressor fouling/cracks and turbine wear have been evaluated by many scholars experimentally and numerically (Otaiku and

Adegun, 2021; Goeing, 2020; Srinival et al., 2018 and Xin et al., 2019) and approaches adopted in these literatures have used in this study with a better modified derived equations that were peculiar for the specimen developed. The work of Patel (2013); Vieweg, et al. (2019) and Kolias et al. (2021), categorically stated that levels of combined compressor and turbine wear were could be assumed to be a contributing factor for decrease in polytropic efficiency by 1% and 2% though there were no derivable methods to prove that these reductions in polytropic efficiencies were linked to a specific physical condition for the compressor or turbine. They also suggested that further study was required to correlate component efficiency and physical state which is the reason for this study and the gap has been covered going by the results presented.

1.2 Literature Review

Goeing (2020); Srinival et al. (2018); Xin et al. (2019) explained that the effect of compression ratio on compressor work is similar to turbine work. Change of air pressure from one flight level to the other, causes the work done by the compressor to change with the change in density As the work increased with increase in the compression ratio, it was expected that the ambient temperature also increased (Rahman et al., 2011).. A low ambient temperature produced high air density and a high gas turbine compressor work and output power. Increased tip clearances and changes in airfoil geometry will lead to unrecoverable condition of the section affected at these stated conditions. However, for the degraded blades the performance of the engine with variation in ambient temperature as a function of compressor work output affected the thermal efficiency of the engine as shown by Bayona-Roa et al. (2019); Liu et al. (2021) and Egorov et al. (2018). This was because, the air mass flow rate inlet to compressor increased with decrease of the ambient temperature. At 90% design speed, the losses in efficiency and pressure ratio were high due to fractured area of the blade pressure surface. It was also noticed that there was a reduction in efficiency of 22% as compared to that of on design configuration. Several researches carried out by Chernikov and Semakina (2023); Puspitasari et al. (2021) ; Deng et al. (2020); Srinivas et al. (2018); Klimko (2017); Rahman et al. (2011); Saravanamutto et al. (2009) and Camporeale et al. (2006) have clearly brought out that the margin to surge in the compressor stage was any speed less than 80-85% of the design speed. At this instance, the net power obtained form the difference between the turbine and compressor could make the shaft accelerate and move the operation point of the
compressor on the compressor map to a new position. In principle, surging is when the airflow through the whole compressor is stopped; stall effect is when only some stages are affected by flow break up. For this reason, the oscillation due to stalling can damage the compressor since it creates stress on the blades.

2. THEORETICAL ANALYSIS

The governing equations are derived by application of mass, momentum and energy equations. The unsteady Reynolds Averaged Navier Stokes (RANS) equation 1D model of fluid flow was used as a background. The dynamic effects such as the mass flow and work imbalances during engine transients were evaluated using the inter-component volumes method described in Fawke and Saravanamuttoo (1971). These transient operations existed in both compressor and high-pressure turbine. The numerical approach for modelling the unsteady performance of compressor-turbine in this study was as cited from Mathworks (2016); Camilo et al. (2019) and ANSYS Academic research (2016 and 2018) and represented as shown in Equations 1-10.:

2.1 Continuity Equation

$$\frac{\partial U_i}{\partial x_i} = 0. \quad (1)$$

$$\frac{\partial \rho}{\partial t} + \frac{\partial (\rho U_i)}{\partial x_i} = 0 \quad (2)$$

2.2 Momentum Equation

$$\frac{\partial (\rho u_i)}{\partial t} + \frac{\partial}{\partial x_j}\left(\rho u_i u_j\right) = \frac{\partial p}{\partial x_i} + \frac{\partial}{\partial x_i}\left[\, 2\mu s_{ij}\right] + \rho g_i + F_x \quad (3)$$

From Continuity Equation 3. The strain-rate tensor S_{ij} is given in Equation

$$S_{ij} = {}^1\!/_2 \left(\frac{\partial (u_i)}{\partial x_j} + \frac{\partial u_j}{\partial x_i}\right) \quad (4)$$

Reynolds Averaged Thermal Energy Equation

$$\frac{\partial T}{\partial t} + \frac{\partial (u_i T)}{\partial x_i} = \frac{\partial}{\partial x_i}\left(\alpha \frac{\partial T}{\partial x_i}\right) + S \quad (5)$$

Reynolds averaged transport equation

$$\frac{\partial(\rho\Phi)}{\partial t}+\frac{\partial}{\partial x_j}(\overline{\rho u_\iota \Phi})=\frac{\partial}{\partial x_i}\left[\Gamma\left(\frac{\partial\Phi}{\partial x_i}-\overline{\rho u_\iota \emptyset}\right)\right]+\overline{S_p\Phi}+\overline{S_c} \quad 6$$

Reynolds time average Momentum or Navier-Stokes Equation (RANS)

$$\frac{\partial(\rho U_i)}{\partial t}+\frac{\partial}{\partial x_j}\left(\rho U_i U_j\right)=\frac{\partial P}{\partial x_i}+\frac{\partial}{\partial x_i}\left[\mu\overline{S_{\iota J}}\right]-\frac{\partial}{\partial x_j}\overline{\left(\rho U_\iota U_J\right)}+\tau_{ij} \quad 7$$

Where Reynolds stresses $\tau_{ij}=\overline{(\rho U_\iota U_j)}$

Transient Term

$$\rho\frac{\partial(\overline{U_\iota+u_\iota})}{\partial t}=\rho\frac{\partial U_i}{\partial t} \quad 8$$

Convective Term

$$\rho\frac{\partial[(\overline{U_\iota+u_\iota})(\overline{U_j+u_j})]}{\partial x_j}=\rho\frac{\partial[(\overline{U_\iota U_j+U_j u_\iota})(\overline{U_j U_\iota+U_\iota u_j})]}{\partial x_j} \quad 9$$

Pressure Term

$$\frac{\partial}{\partial x_i}(\overline{P+p})=\frac{\partial P}{\partial x_i} \quad 10$$

Assuming convective, pressure and viscous terms in above equations represent time averaged components and are equal to zero.

3. METHODOLOGY

Assumptions

In this study, the following assumptions were applied before developing equations.

a. Surface reductions changes with the blade length only as width remains constant.
b. The air/gas in both sections are compressible.
c. The equations were valid for laws of conservations.
d. The compression and turbine are adiabatic and isothermal.
e. The average heat flow to the surroundings is $\dot{Q}$.
f. The stagnation temperature is constant.

3.1 Problem formulation

Compressor and turbine blades experience repeated mechanical loadings during operation due to the large centrifugal stress caused by high rotational speed and temperature. Numerical and analytical methods were applied in this study to determine the rate of change of rotational speed at high temperatures to determine the quantity of fatigue (centrifugal stress) in the engine that will cause the reduction in the blade length and surface area.

3.2 Numerical Solution

The geometry of the blades and temperature range considered in this simulation were obtained from the experimental investigations carried out by Otaiku & Adegun (2021). In this numerical method, the blades were developed using SOLIDWORKS 20. Numerical solutions were obtained using ANSYS Fluent 20. The meshes were created in Mechanical APDL with 900×10^3 elements as the densest as shown in Figure 1a & b The boundary conditions for the compressor was set as 295 to 325 K and 1083 to 1235 K for the turbine. P_2, P_1 and P_4, P_3 represent the static pressures at the outlet and inlet of the compressor and turbine respectively. The simulation was performed in RANS $k-\omega$ Shear Stress Transport SST. This tool helps in running turbulent flow and facilitates the modelling of small element sizes (900×10^3 elements) that are smaller than the selected grid spacing. The time step was 0.001s. For each unsteady performance, over 500 iterations were executed to obtain results. The fluid was assumed as compressible air for compressor and gas for turbine. The turbulent flows depict fluctuating fluid velocity which can be characterized as high frequency in momentum and energy equations.

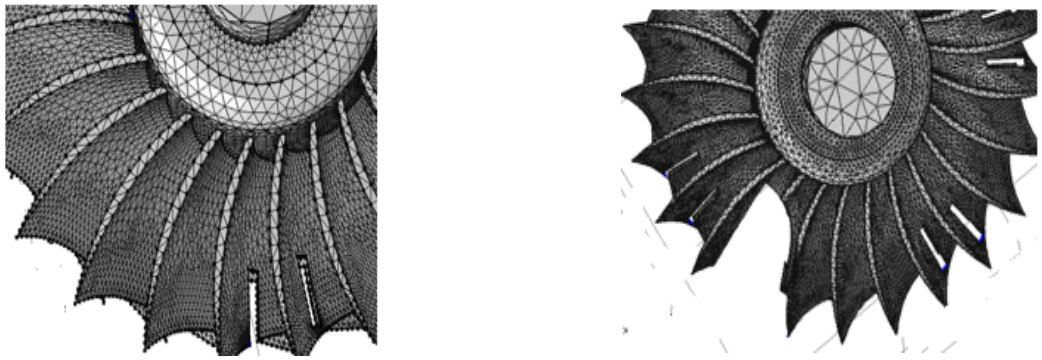

a. Formation of crack aize. b. 10% fractured area

Figure 1: Mesh specimen/

3.3 Analytical Method

The unsteady state for the compressor and turbine cause changes in mass flow rate, temperature and pressure rise. Figure 2 shows the position of the blades to the main engine discs which is used to derive the equations based on the assumptions (a-f).

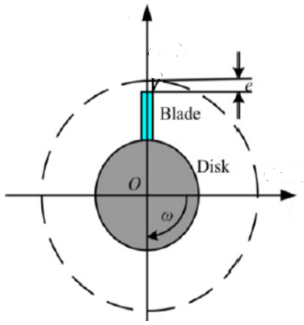

Figure 2: Blade on the compressor/turbine disk.

From Figure 2, the equation for percentage reduction in surface area can be obtained as given in Equation 11-12 below where initial radius at the tip

$$r_0^i = \frac{1}{2} l_0(t) + r_0(t) \quad 11$$

radius at the root $r_h = r_0(t)$

New radius at the tip

$$r_{new}^i = \pi \left(\frac{1}{2} \bar{l}_{new} + r_0 \right)^2 \quad 12$$

The characteristics of the flow was obtained by applying the energy balance in the control volume from Mark and Selwyn (2016) and Equations 1-3 with Equations 11-12 to derive the mechanical characteristics of the rotating blades as shown in Equations 13-22. For rotational transient conditions in x- direction, mass flow rate is as given in Equations 13 a and b.

Mass flow rate

$$\dot{m}_a = \rho v_a^i \pi \left[(r_{new}^i)^2 - \left(r_0^i \right)^2 \right] \quad 13a$$

$$\dot{m}_{in} = \dot{m}_{out} = \rho \, V_{a1} \pi \left(\frac{1}{2} l + (r_{new}^i) \right)^2 = \rho V_{a2} \pi \left(\frac{1}{2} l + r_0^i \right)^2 \quad 13b$$

Pressure per Stage

$$p^i = PR_s{}^i p^{i-1} \quad 14$$

Temperature per Stage

$$T^i = \frac{\omega_c \eta^i M^i}{c_p \dot{m}_a} + T_0{}^{i+1} \quad 15$$

The stage pressure ratio PR is given by the following expression in Equation 16 by Varga et al. (2016) and using the derived mass flow rate in :

$$PR_s = \left[1 + \eta_s \frac{UC_a}{c_p T_{01}} (tan\beta_1 - tan\beta_2)\right]^{\frac{\gamma}{\gamma-1}} \quad 16$$

The temperature at the turbine exit is calculated by substituting temperature in Equation 15 into Equation 17 where the terms $\eta_{is,T}$and PR_Trepresents turbine efficiency and turbine pressure ratio respectively:

$$T_{out} = T_{in}\left[1 - \eta_{is,T}\left(PR_T{}^{\frac{\gamma-1}{\gamma}} - 1\right)\right] \quad 17$$

The PR_{Tc} for transient states in compressor and turbine is obtained using Equations 13 a and b derived for mass flow rate.

Torque

$$M^i = r^i \dot{m}_a (v_a^i)(tan\beta_1^i - tan\beta_2^i) \quad 17$$

Power

$$M^i \omega_c = \left[r^i \dot{m}_a (v_a^i)(tan\beta_1^i - tan\beta_2^i)\right]\omega_c \quad 18$$

3.4 Centrifugal Stress per Stage

The blade tip speed U will be limited by stress considerations at the root. With the assumption (a), the radius of the blade is constant at root r_h, then the equation for the centrifugal stress per stage at the root for varying blade length at the tip is obtained by modifying Equation 18 from Jim and Wesley (2019) as shown below:

$$\sigma_r = \int_{r_t}^{r_h} \rho_b \omega^2 r dr = 0.5\rho_b U_t^2 \left[1 - \left(\frac{r_h}{r_t}\right)^2\right] \quad 18$$

$$\sigma_C = \frac{F_c}{A_h} = \int_{r_h}^{r_t} \rho\, \omega^2 \frac{A_t}{A_h}\, rdr \quad 19$$

3.5 Centrifugal Stress with Rotational Speed

Following Equations 18 and 19, the centrifugal stress and changing surface area of the blade due to fracture or breakaway with rotational speed during the unsteady condition can be obtained by modifying equations developed from Krishnan et al., (2020); Sabila (2020); Alqallaf and Teixeira (2021) as shown in Equations 20 and 21.

$$AN^2 = \frac{360\sigma_t}{\pi\left(1+\frac{A_t}{A_h}\right)\rho_{blade}} \quad 20$$

$$\sigma_C = \frac{\rho\omega^2\left(\frac{1}{2}l+r\right)^2}{\pi}\left[2 - \frac{2}{3}\left(1 - \frac{A_h}{A_h}\right)\left(1 + \frac{1}{1+\frac{r_h}{r_t}}\right)\right] \quad 21$$

So that new length according to degradation (Figure 3) level are

$$l = 17.04\ mm\ (0\%), 14.87\ mm\ (8\%)\ \&\ 14.5\ mm\ (10\%)$$

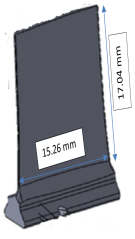

Figure 3: Present Specimen

4. RESULTS AND DISCUSSION

4.1 Increase in Pressure and Temperature

Figures 4, 5 and 6 show profile of the pressure at the 4- stage compressor and the single stage gas generator turbine for 0% degradation. The pressure contours for the two sections were similar to those predicted by Hocko (2019) as shown in Figure 7. Here, for each increase in the compressor exit temperature and TIT for the turbine, changing inlet parameters would not significantly affect the performance when on on-design parameters or according to manufacturer's specifications as shown in Figure 4 and 6. . However, during transient conditions with increment of time change, ambient parameters significantly affect exit pressure and temperature depending on the level of degradation as shown in Figures 8 and 9. However, the results obtained in the experiment were similar to those predicted by RANS in the simulation. The difference between them was because the experimental data were obtained from static position. Comparing the numerical results with previously obtained experimental results, it can be said that the effect of astronomical increase in pressure flow of hot air and gas is due to presence of cracks by extension, dislocations and disorientations of the densely packed grains of the blades constituent elements which could eventually result into heavy material loss.

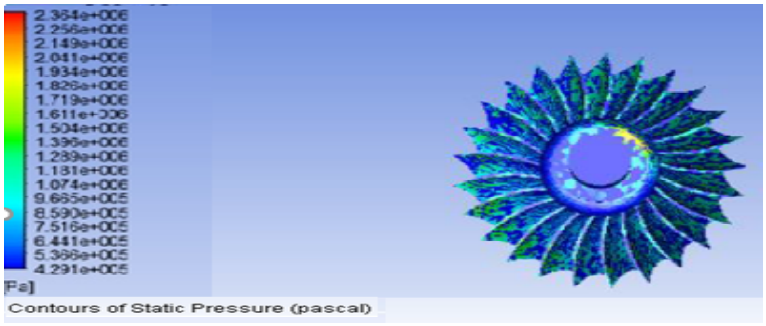

Figure 4: Undegraded (0%) compressor blades.

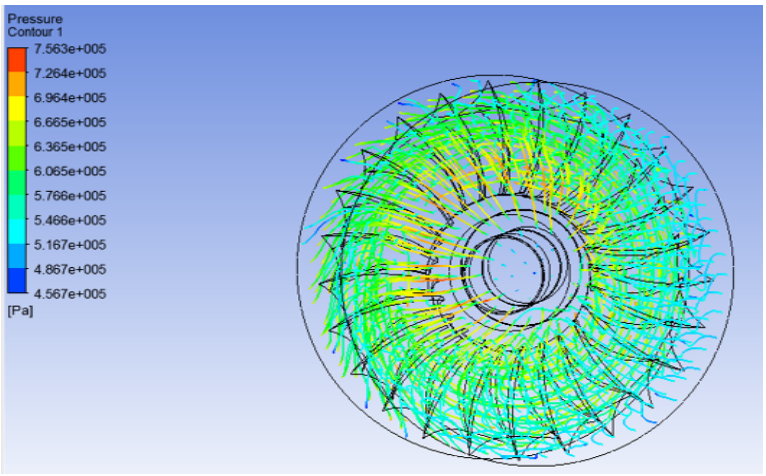

Figure 5: Undegraded (0% degradation) Turbine blades.

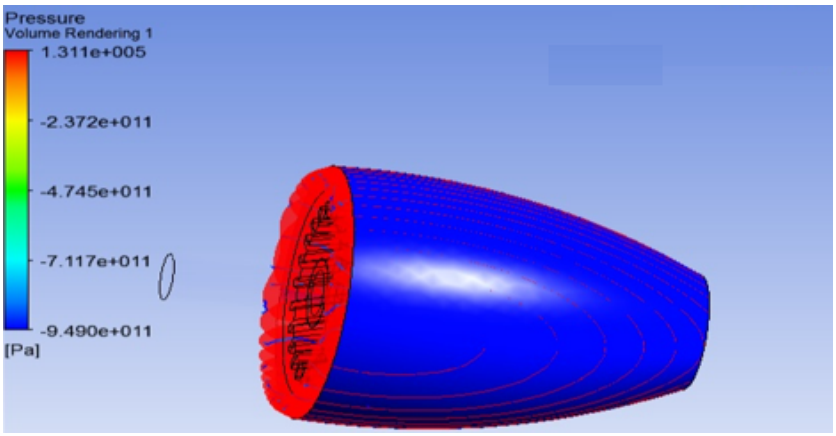

Figure 6: Evenly distributed pressure flow-
Turbine assembly.

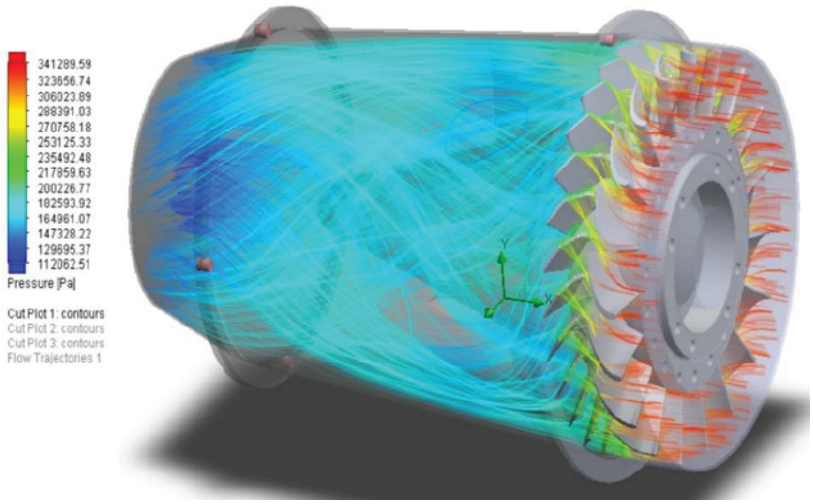

Figure 7: Pressure flow from tip to hub
Source: Hocko (2019).

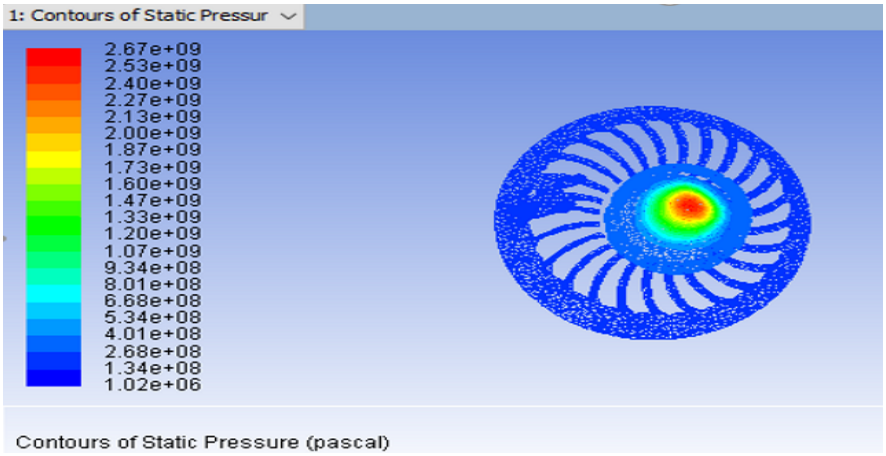

Figure 8: 8% degradation blades

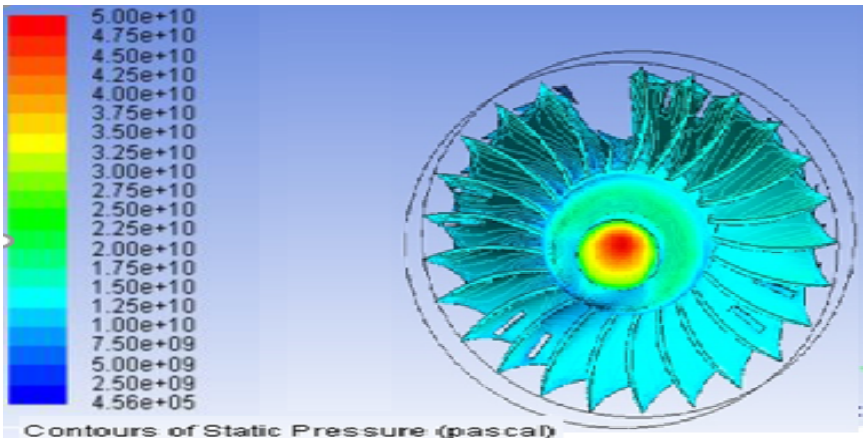

Figure 9:10% degradation.

4.2 Temperature Contour

In the same sense like pressure, temperature contours for the compressor and the turbine for steady state is as shown in Figures 10 and 11 with the ambient conditions applied.

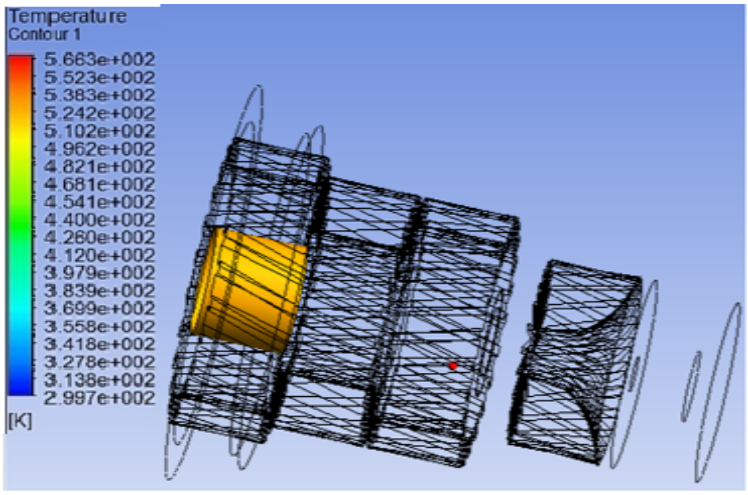

Figure 10: Effect of ambient temperature on compressor exit temperature (4- stage compressor assembly).

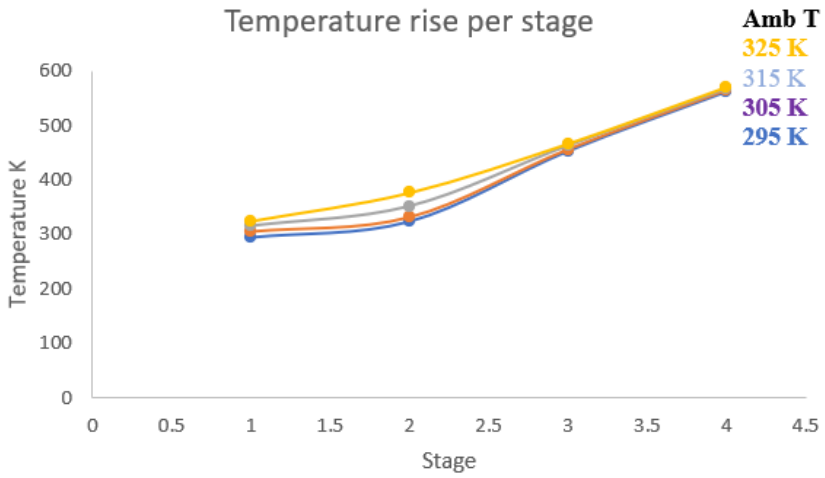

Figure 11: Insignificant effects of ambient temperature on compressor exit temperature.

Here ambient temperatures T1 in the range of 295 to 325 K were producing constant compressor exit temperatures T2 with little or no variations as shown in Figure 11. After the initial changes in pressure and temperature parameters, RANS model selected in FLUENT gave a convincing result of the new state of the sections being studied as shown in Figures 12-15.

In furtherance to the investigation of blades degradations, Figure 12 show the turbine inlet temperatures increasing beyond allowable value as shown.

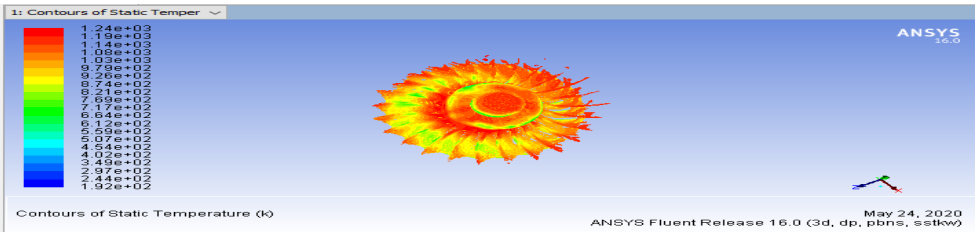

Figure 12: Too high Turbine Inlet Temperature.

This increase in TIT (T3) is precipitated by sudden increase in temperature T2 from the compressor depending on the level of degradation as analytical solutions show in Figures 13 and 14.

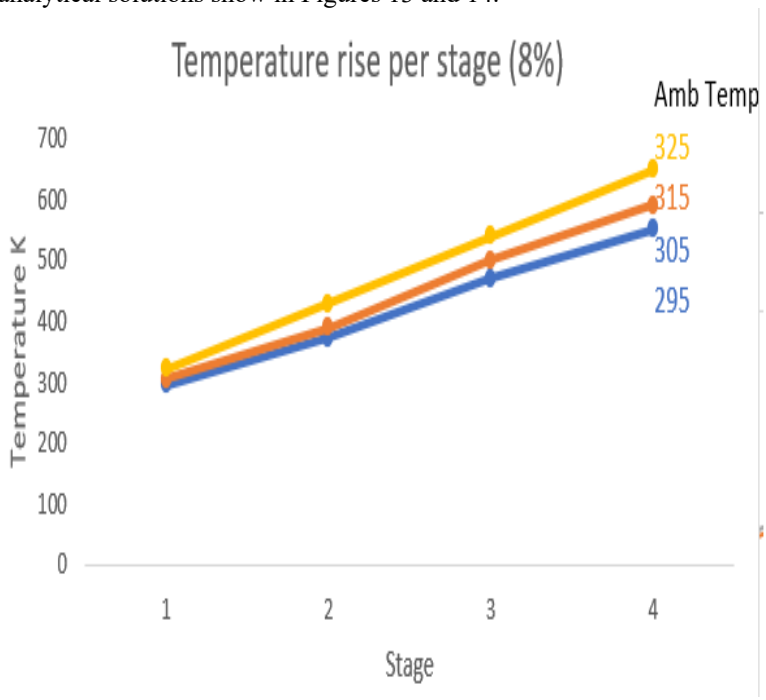

Figure 13: 8% degradation (4-compressor)

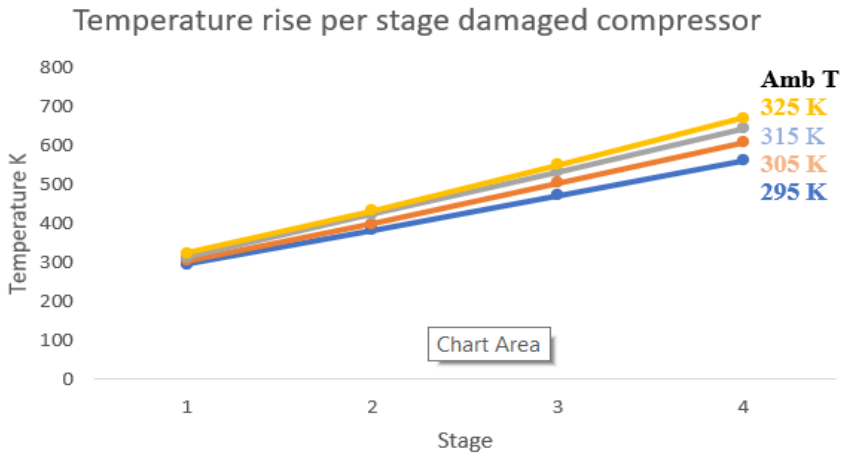

Figure 14: 10% degradation (4-stage compressor).

As can be seen from Figure 14, ambient temperature of 315 K produced analytical value of ≈ 570 K as compressor exit temperature for an 8% surface area degradation. Increase in temeprature beyond this level of degradation will severely affect the compressor exit temperature as compared to simulation result obtained in Figure 15 showing ≈ 569 K at the same ambient temperature. At 325 K, compressor exit temperature for 8 and 10% blade degradation will astronomically increase beyond the permisssible working temperature of the Ti-6AL-4V material of the blades in the compressor. Figure 15 show already degraded cowling and deformed outer surface of the compressor assembly due to this astronomical exit temperature and will continue to increase as long as the ambinet temperature increases and worsen the condition of the blades and the engine at large. This simulated or analytical temperature value will berth the badly damaged turbine condition as shown in Figures 12 and 16 respectively.

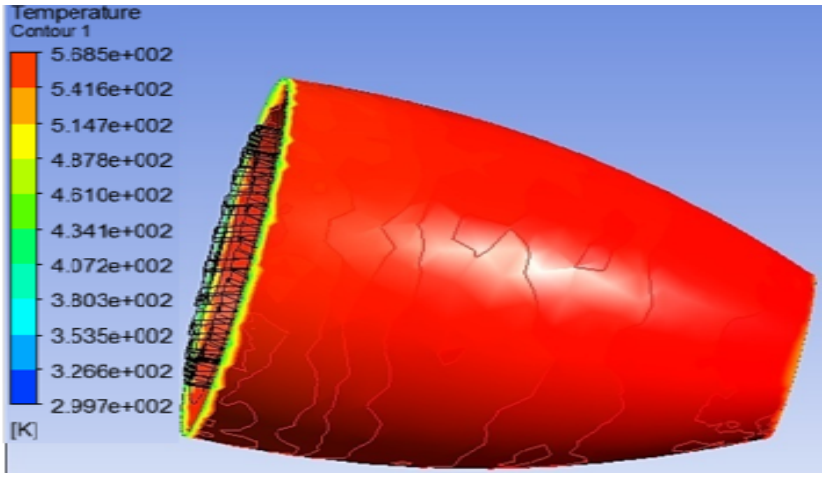

Figure 15: Effect of change in ambient temperature on compressor exit temperature for 10% degradation.

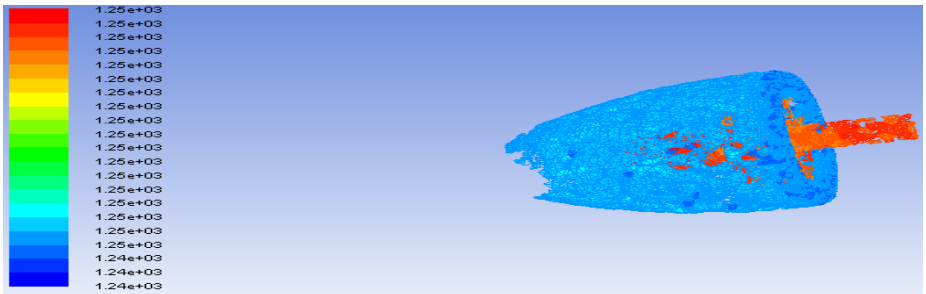

Figure 16: 10% degradation in the turbine

4.3 Velocity Contour

The mean velocity contour obtained from the unsteady simulation showed (Figure 17) high turbulent swirl and reversal flow especially in the turbine to depict the level of degradation of turbine and its closeness to approaching surge margin at temperatures beyond 315 K. This condition will aggravate as the engine shaft speed in RPM increases.

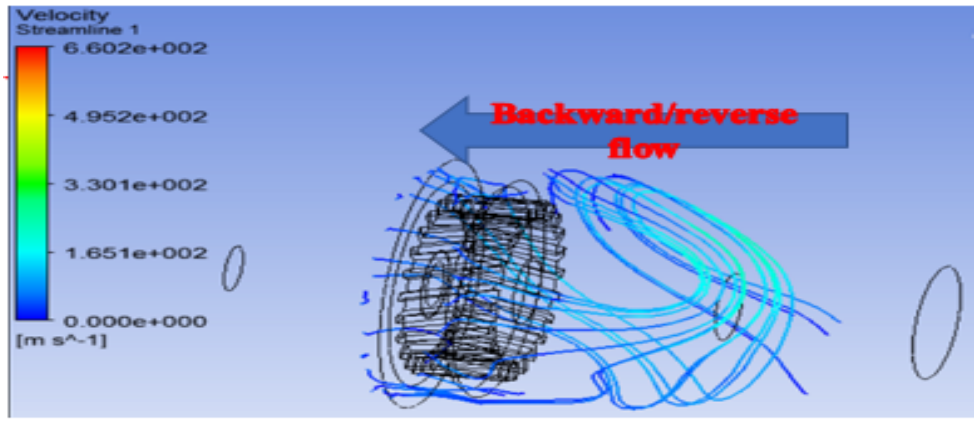

Figure 17: Flow reversal and turbulence flow in the turbine with 10% degradation.

As stated earlier, the velocity contour at the turbine shows large reversal flow due to 10% surface area reduction of the blades in the turbine enclosure.

4.3 Centrifugal stress

Centrifugal stress values for 0-10% surface area degradation was analytically obtained as shown in Figure 18. As can be viewed from Figure 17, flow reversal in the turbine and high rotating speed of the turbine shaft will impose high risk centrifugal stresses on the blades. At instances of high ambient and compressor exit temperatures the compressor and the turbine will experience near rotating stall otherwise known as surge condition reason for the need to check ambient and turbine inlet temperature when blade degradation is noticed. Flying in warm air ISA condition for degraded engine is a recipe for unsafe flight.

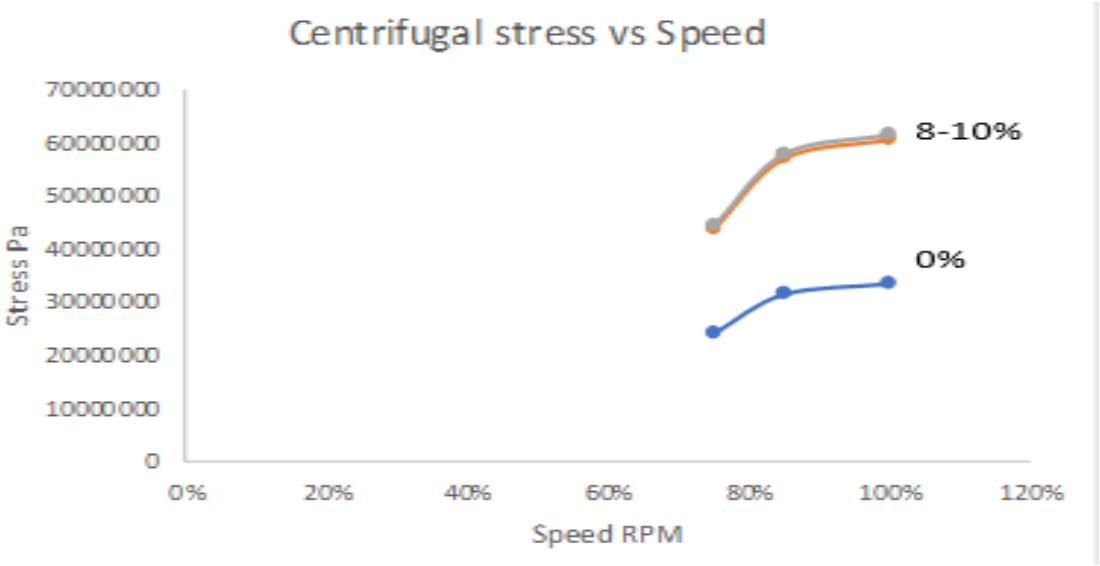

Figure 18: Centrifugal stress versus degradation level.

5. CONCLUSION

The operating pressure and temperature are important performance parameters in the compressor and turbine of gas turbine engines. So for a steady flow performance, on design parameters at the outlet of the compressor and the inlet of the turbine must be as specified. However, in real life operations, these parameters are sometime exceeded above the permissible range of the materials for the stage or section. Analytical and simulations results conducted in this study showed that astronomical increase above specified pressure and temperature ranges would cause degradations of the blades leading to severe unsteady performance. Once degraded, higher inlet/ambient temperature into the compressor would produce higher exit and inlet temperatures at the compressor and turbine respectively. Degradation from 0 -10% were simulated and analysed as 10% and above was found worse off above 315 K (ambient temperature) which could lead to permanent engine failure. Any change above 315 K for such level of degradation would cause flow reversal in the turbine due to higher TIT and could lead to a rotating stall or surge. Centrifugal stress (60 kN/m^2) imposed on the blades during the new condition would cause engine burn-out which is hazardous to safety during flight.

6. Recommendations

In the event of stall before surge during flight operations, the maximum engine RPM should not exceed 80% and at TIT above 1092 K. On this note, Engine Manufacturers are advised based on this study to incorporate Centrifugal Stress Engine Instrument that will indicate the centrifugal stress levels of the engine at any face of flight to make on spot decision by the crew to mitigate against risk of more fractured blades and breakaways which is hazardous to flight safety. For further study, experiment should be carried out on rotating blades of the compressor and the turbine.

7. APPENDICE

7.1 Euler Tubomachinery Equation

The Euler turbine equations for work in terms of wheel speed, relative velocity, and absolute velocity are given in this section in Equations 22-25. As the turbine produces more power than is required to drive the compressor during transient condition, the shaft accelerates until a new balance point between the compressor and turbine power is found. It is vice versa, for the compressor so that as it uses more power than the turbine is able to deliver, deceleration of the shaft occurs. The difference between the turbine and the compressor, i.e the surplus power, is obtained from Equation 22:

$$SP = \eta_m \dot{m}_2 (h_3 - h_4) - \dot{m}_1 (h_2 - h_1) \quad (22)$$

7.2 Surplus Power of the Dynamic Turbine Shaft

Inertia of the shaft consisting the turbine and compressors axes against any change in shaft rotational speed as a function of shaft power is as shown in Equation 23 – 24.

$$SP = M\omega = I\alpha\ (2\pi N) = I\frac{d\omega}{dt}\ 2\pi N = \frac{4\pi^2\ I\ NdN}{dt} \quad (23)$$

7.3 Dynamic Rotational Speed

Theoretically, the new rotational speed for a change in power (surplus power) is as given in Equation 24-26

$$\frac{dN}{dt} = \frac{SP}{4\pi^2\ I\ NdN} \quad (24)$$

Numerically, this is solved using Equation 25

$$N = \int_t^{t+dt} \frac{SP}{4\pi^2\ I\ NdN} \quad (25)$$

Otherwise using Euler Equation, the dynamic rotational speed is as given in Equation 26:

$$N_{new} = N_{old} + \left(\frac{dN}{dt}\right)_{new} . \Delta t \quad (26)$$

8. ACKNOWLEDGEMENT

The authors would like to thank University of Ilorin especially Profs, AGF Alabi, Aweda and Alao for their advisory role. Also worthy of note is Tgt. Rasheed from Kwara State for providing laboratory facilities for the simulation and

experimental results respectively. Also, very special thanks to Petroleum Technological Development Fund (PTDF) for the financial support for my Ph.D work and Police Air Wing Abuja (ACP Ndubuisi and Engr. Cosmos Eze).

9. Conflict of Interest

The authors declare that no conflicting interest.

10. Data Availability

Operating data from the Aircraft Maintenance Manual from the manufacturer was used.

11. REFERENCES

Otaiku I.O and Adegun I.K. (2021). Investigation of preliminary factor leading to first-third stage blade cracks initiation, growth and their effects on aero-engine performance. The Nigerian Institute of Mechanical Engineers, 34th International Conference and Annual General Meeting (2021).

Marek Klimko (2017) "Strength analysis of an aircraft turbo-compressor engine turbine disc, Cite as: AIP Conference Proceedings 1889, 020019 (2017); https://doi.org/10.1063/1.5004353.

Saravanamutto, H. I. H; Rogers, G. F.C., Cohen, H., Strazincky P. V., (2009): Gas Turbine Theory, 6th ed., Pearson Education Limited, ISBN: 978-0-13-222437-6, 2009

Rahman M. M., Ibrahim T.K, and Abdalla A.N, (2011). Thermodynamic performance analysis of gas-turbine power-plant. International Journal of the Physical Sciences Vol. 6(14), pp. 3539-3550, 18 July, 2011 http://www.academicjournals.org/IJPS

DOI: 10.5897/IJPS11.272. ISSN 1992 - 1950 ©2011 Academic Journals

Deng C., Abdalla A.N., Ibrahim T.K., Jiang M.X., Al-Sammarraie A.T., and Wu J. (2020). Implementation of Adaptive Neuro-fuzzy Model to Optimize Operational Process of Multiconfiguration Gas-Turbines. Advances in High Energy Physics Volume 2020, Article ID 6590138, 17 pages. https://doi.org/10.1155/2020/6590138

Camporeale, S. M.; Fortunato, B.; Mastrovito, M. A (2006). Modular Code for Real Time Dynamic Simulation of Gas

Turbine in Simulink. Transactions of the ASME, v. 128, p. 506-517, July 2006.

Srinivas G., Raghunandana K., and Satish S.B. (2018) Axial-flow compressor analysis under distorted phenomena at transonic flow conditions, Cogent Engineering, 5:1, 1526458, DOI: 10.1080/23311916.2018.1526458

Puspitasari P., Andoko A., and Kurniawan P. (2021) Failure analysis of a gas turbine blade: A review. https://www.researchgate.net/publication/350161777 Failure analysis of a gas turbine blade: A review Article *in* IOP Conference Series Materials Science and Engineering · February 2021 DOI: 10.1088/1757-899X/1034/1/012156.

Yadav M., Misr A., Malhotra A. and Kumar N. (2019). "Design and analysis of a high-pressure turbine blade in a jet engine using advanced materials", *Materials Today: Proceedings [Internet]*. 2019 Aug 16 [cited 2019 Nov 22]; Available from: https://www.sciencedirect.com/science/article/pii/S2214785319327191.

Rao V.N.B., Kumar I.N.N., Prasad K.B., Madhulata N., Gurajarapu N. (2014), "Failure mechanisms in turbine blades of a gas turbine Engine –an overview", *Int. J. Eng. Res. Dev*, Vol. 10, pp.48-57, 2014.

Vasilyev, B.; Selivanov, A. (2019) Numerical method of single-crystal turbine blade static strength estimation taking into account plasticity and creep effects. Mater. Phys. Mech. 2019, 42, 311–322

Chernikov, V.; Semakina, E. (2023) Experimental and Numerical Studies of the Aerodynamics of Stationary Two-Shaft Gas Turbine Exhaust System. Energies 2023, 16, 3671. https://doi.org/10.3390/en16093671.

Kuschel, M.; and Seume, J.R. (2011). Influence of Unsteady Turbine Flow on the Performance of an Exhaust Diffuser. In Turbo Expo: Power for Land, Sea, and Air; Volume 7: Turbomachinery, Parts A, B, and C; ASMEDC: Houston, TX, USA, 2011; pp. 1551–1561.

Fleige, H.-U.; Riess, W.; Seume, J. (2002) Swirl and Tip Leakage Flow Interaction with Struts in Axial Diffusers. In Turbo Expo: Power for Land, Sea, and Air; Volume 5: Turbo Expo 2002, Parts A and B; ASMEDC: Houston, TX, USA, 2002; pp. 871–878.

Vasilyev B., Nikolaev S., Raevskiy M., Belov S. and Uzhinsky I. (2020) Residual Life Prediction of Gas-Engine Turbine Blades Based on Damage Surrogate-Assisted Modeling. Appl. Sci. 2020, 10, 8541; doi:10.3390/app10238541.

Janikovič J., Pilidis and Singh (2010) Gas Turbine Transient Performance Modeling for Engine Flight Path Cycle Analysis.

NOMENCLATURE

A = area (m2)
Alt = altitude (m)
C = speed of sound (m/s)
Va = velocity of air at inlet (m/s)
Cp = specific heat at constant pressure (kJ/kgK)
F = thrust
FAR= fuel air ratio
h = specific enthalpy (kJ/kg)
LHV=lower heating value of fuel (kJ/kgK)
m = mass flow rate of fluid (kg/s)
*m*a = mass flow rate of air at inlet (kg/s)
*m*f = fuel mass flow rate (kg/s)
M = Mach number
p = total pressure (bar)
ps = static pressure (bar)
RpC = compressor pressure ratio (overall)
R = characteristic gas constant
s = specific entropy (kJ/kgK)
SFC= specific fuel consumption (kg/Nh)
T = total temperature (K)
Ts = static temperature (K)
TIT = turbine inlet temperature (K)
W = specific work (kJ/kg)

Greek Symbols

Δp = pressure loss
γ = specific heat ratio
ρ = density
η = efficiency (%)

Suffixes

a = air
amb = ambient
b = burner
g = gas
p = pressure

PAPER – 129 MATHEMATICAL MODELLING OF WELDING PARAMETERS AND THEIR EFFECTS ON ENERGY CONSUMPTION IN WELDED CR-MO METAL

Aweda J.O.[1] and Adewuyi, R.A.[2*]

[1]Department of Mechanical Engineering, University of Ilorin, Ilorin, Nigeria
[2]Department of Mechanical Engineering, The Federal Polytechnic, Ado-Ekiti, Nigeria
*Email: reuben1178@yahoo.com

ABSTRACT
This study examined the mathematical modelling of the effects of heat flux on welded Cr-Mo flat steel bars using the TIG arc welding method (ASTM A304). The TIG method employed was a double-sided half V-groove welding process with heat moving source while varying welding parameters such as material thickness, number of passes, electrodes' types and electric current in the process of welding. The mathematical transient heat transfer equations generated were run on Autodesk CFD 2018 software with welding parameters as inputs. The software was used to generate the 3-D model heat (temperature) profiles of the welded metal from the point of welding through the heat-affected zone to the parent metal. The temperature fields of the process produced by the software were distinguished by colours with the high intensity of heat being the welding zone (red) and the least at the parent metal (light blue). The temperature fields obtained were compared with the experimentally obtained values and found to be very close in values with the modelled values being slightly higher. The study demonstrated that modelling welding heat flux even before undertaking the process is a reliable tool to adopt in the welding of the Cr-Mo flat steel bar.

***KEYWORDS*:** modelling, welding parameters, heat flux, electrodes.

1. INTRODUCTION

Welding is a widely used method in most fabrications for joining metals due to its reliability and effectiveness, Tailor *et al*. (2010). However, the failure rate of machine parts during service is significantly influenced by non-uniform volumetric temperature changes in welded specimens. Simulation tools based on finite element analysis (FEA) can predict weld heat cycles and stress analysis. Nevertheless, the current industrial practice still relies on trial and error and expertise from prior designs to develop welding procedures (Kollár & Kövesdi, 2018).

Previous literature has explored various aspects of Tungsten Inert Gas (TIG) welding's modelling, simulation and process optimization. Double ellipsoidal heat source model proposed by Goldak et al. (1984) was commonly used in welding simulation and has been shown to provide good agreement with results in the elastic-plastic analysis of welded plates. Additionally, the heat input and welding parameters strongly influenced the mechanical properties of weld joints. Zhu & Chao (2006) concluded that temperature-dependent material has significant effects on welding simulation in FEA. Both thermal and mechanical material properties should be considered temperature-dependent for accurate simulation. Thermal conductivity has some impact on the distribution of the transient temperature field during welding, but material density and specific heat have negligible effects. Rocha *et al*. (2018) investigated the modelling of the temperature field generated by the deposition of a weld bead on a steel butt joint by FEM techniques and thermographic images. The comparison of experimental and numerical results showed that the thermal cycles on all selected points were almost identical. However, in the cooling phase, there was a good agreement only until about 300°C. Both experimental and simulation methods were used for butt-welded specimens.

In this study, Autodesk Computational Fluid Dynamics (CFD) simulation software was utilized to analyse the thermal and stress effects of TIG welding on Cr-Mo steel bars of various thicknesses (5 mm, 10 mm, and 15 mm) measuring 50 mm by 100 mm. The impact of energy input, heat ad temperature distribution was examined and numerical analysis was validated with experimentally obtained transient temperature curves. The study aimed at evaluating the impact of weld heat input on the mechanical properties of Cr-Mo steel that was TIG welded and compared the results of Autodesk CFD simulation with the experimental results.

Therefore, simulation tools based on FEA have been used to predict weld heat cycles and temperature profiles of welded metal. This will lead to improvement in the accuracy of welding modelling with adequate prediction of both thermal and mechanical material properties of temperature.

2. METHOD OF SOLUTION

2.1. Numerical analysis

Finite Element Method (FEM) (Flint et al., 2017), a mathematical technique was adopted to solve the partial differential transient heat transfer equations generated during the welding operation. It was used to study and analyse complicated physical problems, particularly those displaying non-linear geometry and/or material behaviour, which is often the case in welding situations involving transient heat transfer. Some examples of coupled situations and conjugate heat transfer include thermomechanical, where confined differential thermal expansion causes thermal stresses and strains, and thermoelectric, where heat is generated in a material due to its resistance to current flow. Numerical setup for modelling of the transient state, the welding parameters and mechanical properties specified by ASTM A304 were considered. The model was created using Autodesk Inventor 2017 and then imported into Autodesk CFD 2018, where the mechanical properties were set to Cr-Mo steel bar A304 using the toolbar and the sequential modelling is presented in Table 1 and Figure 1.

Table 1: Mechanical Properties of Cr-Mo A304 Steel flat bar (Hashemzadeh et al., 2015)

Properties	Values
Density, ρ	8000 kg/m^3
Hardness	123 HV
Ultimate Tensile strength	505 MPa
Tensile strength at yield	215 MPa
Elongation at break	70 %
Modulus of elasticity	193–200 GPa
Poisson's Ratio	0.29
Charpy impact	325 J
Shear modulus	86 GPa

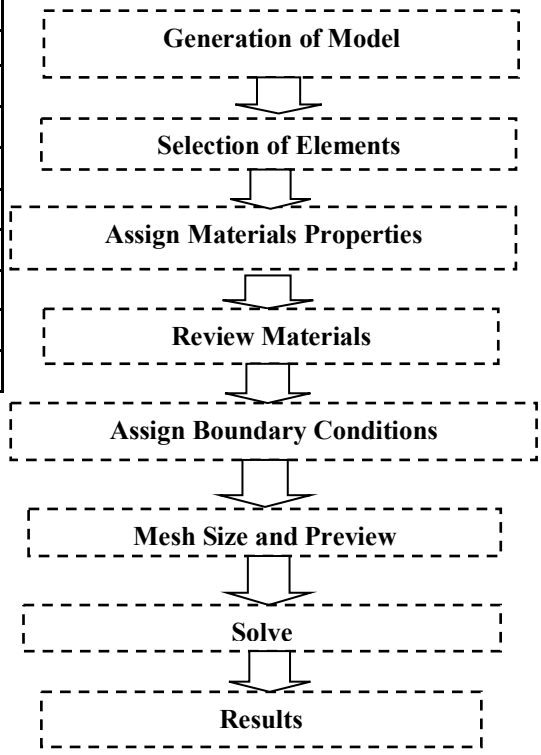

Figure 1: Sequential modelling

2.2. Experimental procedure

The Cr-Mo steel flat bar used was of varying thicknesses of 5mm, 10mm, and 15mm and was welded using a double-sided half V-groove joint with a Tungsten inert gas (TIG) welding machine. Other varying parameters include electrode diameter, weld current and number of weld passes. The materials were machined in pairs to size 100mm by 50mm from different thicknesses, with 18 samples of the Cr-Mo flat steel bar type under consideration. Before the welding operation, on each pair, a hole of 5.0 mm was drilled and tapped close to the weld centreline of the samples where a K-type thermocouple of 2000^{0}C capacity was connected to a data logger with type K thermocouples –3 channel–LU-MTM-380SD to measure temperature distribution between the base metal and welded bead which changes with time while welding operation was on. The Arc welding temperature (1350 - 1450 ^{0}C) was measured using Digital Infrared Thermometer Ametek LAND Cyclops 100L S/N 240671 91.

The assembly was performed with the welding current of 90 A, 100 A, and 150 A (DCEN), at a constant voltage of 24 V, and the welding rate of 0.2703 mm/s.

2.3. Theoretical analysis

The modelling of the transient state of a Tungsten Inert Gas (TIG) weldment using numerical and analytical methods is described in this study. A Double-Sided Half V-Groove weld joint that joins two steel bars was formed, with dimensions of 50mm by 100mm and thicknesses of 5mm, 10mm and 15mm. The welding procedure was modelled as a single pass on both sides of the bar in this analysis, and the weldment was symmetrical.

The Finite Element (FE) modelling of the TIG welding process was conducted in two steps using Autodesk Inventor 2017 for the physical modelling of the specimens and Autodesk CFD 2018 for structure and thermal analyses, the approach of Chujutalli et al. (2020), Ravinder (2015) and Rocha et al.(2018) were adopted and used in the validation. The non-uniform volumetric temperature distribution during the weld thermal cycle leads to non-uniform volumetric changes that cause weld thermal stresses. These non-uniform volumetric changes were due to solidification of the weld zone (WZ), metallurgical transformations, and plastic deformation, and result in distortion of grains. These welding-induced thermal stresses and distortion of grains are critical in the design of welded joints and structures. Figure 2 represented the numerical modelling of weld heat input with heat source Q adopted that focuses on the weld pool and Figure 3 shows heat conduction analysis in the weld metal. A finite element simulation was performed, yielding the temperature distribution, welding-induced thermal stresses and the distortion of grains in a Double-Sided Half V-Groove welded bar. Goldak's double ellipsoidal heat source model with Transient temperature distribution was used, following previous works by Tailor *et al*., 2010; Ravinder, 2015; Rocha *et al*., 2018; Hashemzadeh *et al*., 2015. The results of this study can be used to optimize the design and performance of welded joints and structures.

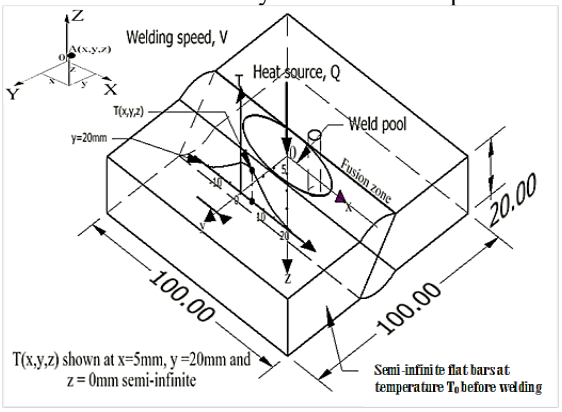

Figure 2: Weld heat input model in weld metal

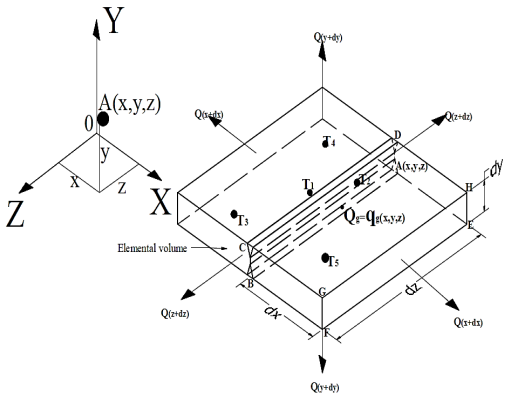

Figure 3: Heat conduction analysis in 3D model

Determination of Heat flux/thermal energy radiated over weldment surface, as shown in Figure 3. Heat flux/thermal energy over weldment surface (q): $Q/A=q= k\, dT/dx$ (1)

Where;

k =thermal conductivity of the material,

dT = change in temperature and dx = thickness of the material, according to Flint *et al.,* 2017, Trupiano *et al.,* 2022 and Rajput, 2012.

Let T = Temperature at the face ABCD (weld zone)

$(dT/dx)\,dx$ = Change in temperature through distance dx

$T+ (dT/dx)\, dx$ = temperature on the right face EFGH (at a distance dx from the left face ABCD; HAZ & Base metal).

2.4. Heat governing equations

Heat influx due to heat flow by conduction is given by the Fourier equation (Rajput, 2012)

$$Q'_x = -k_x(dy.dz)\frac{\partial T}{\partial x}.dt. \quad (2)$$

$$Q'_y = -k_y(dx.dz)\frac{\partial T}{\partial y}.dt. \quad (3)$$

$$Q'_z = -k_z(dx.dy)\frac{\partial T}{\partial z}.dt. \quad (4)$$

The transient temperature during welding is

$$\frac{\partial}{\partial x}\left[k_x\frac{\partial T}{\partial x}\right] + \frac{\partial}{\partial y}\left[k_y\frac{\partial T}{\partial y}\right] + \frac{\partial}{\partial z}\left[k_z\frac{\partial T}{\partial z}\right] + q_g = \rho.c.\frac{\partial T}{\partial t}. \quad (5)$$

or, using the vector operator ∇, we get

$$\nabla.(k\nabla T) + q_g = \rho.c.\frac{\partial T}{\partial t}. \quad (6)$$

The equations for convection and radiation are given as

$$q''_{conv} = h_f(T - T_0). \quad (7)$$
$$q''_{rad} = \varepsilon\sigma(T^4 + T_0^4). \quad (8)$$

Where

ρ = density, c = specific heat, q_g = internal heat generation rate, k = thermal conductivity and t =time interval. h_f =convection coefficient, ε = emissivity, σ = Stefan-Boltzmann constant, T = body temperature, and T_0 = ambient temperature, similar to observations by Hashemzadeh (2015) and Chen and Soares (2016).

2.5. Assumptions and boundary conditions

The heat transfer was in a transient state and involved several iterations between 0-500. The voltage used was 24V, the weld length was 100mm and the welding time was 370s. Based on experimental results, the welding rate was 0.2703mm/s.

2.6. Nodes, elements, degrees of freedom

Nodal discretization and Grid Independence test of nodes on peak temperature as shown in Figures 4 and 5 respectively. The 3D model of Cr-Mo flat steel bar underwent both thermal and structural analyses and had meshes consisting of 13,549 nodes and 6,989 elements (5 mm thick), 14,565 nodes and 7,537 elements (10 mm thick), and 16,254 nodes and 9,946 elements (15 mm thick) as represented in Figure 6(a-c). The degrees of freedom at each of the nodes that form the elements for thermal analysis is the temperature (T) and structural analysis is displacements (Ux, Uy, and Uz). The analysis at each node has four degrees of freedom - Ux, Uy, Uz, and T (due to thermal expansion effects) according to Arpita (2016), Malhotra *et al*. (2014) and Zhu and Chao (2006).

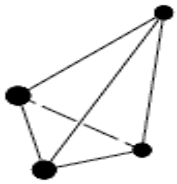

Figure 4: 3-D Solid element, Tetrahedral with four sides

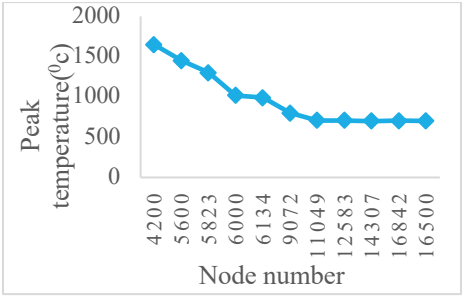

Figure 5: Grid Independence Test

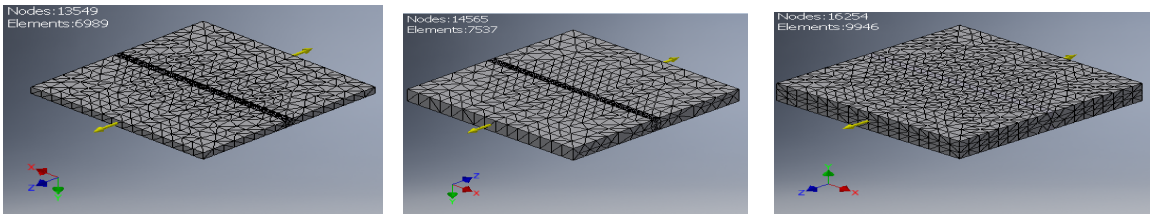

(a) (b) (c)

Figure 6(a-c): Geometry and mesh distribution in a 3D model for 5 mm, 10 mm and 15 mm thick Steel flat bars

3. RESULTS AND DISCUSSION

3.1 Thermal analysis of welded metal

The effect of weld heat input on welded metal was modelled with a coupled temperature-displacement analysis, each node in the weld model has three degrees of freedom Ux, Uy, Uz, and T (due to thermal expansion effects) in three planes (YZ, XZ, and XY). Thermal model (temperature fields) on Cr-Mo steel using Autodesk (CFD) 2018 revealed how temperature fields change over the length of the welded specimen. The reddish area of the weld zone changed towards the bar's edges. This colour change was used to investigate thermal stresses that occurred within the grains that lead to failure. The thermal simulation of the heat-affected zone and weld pool on Cr-Mo steel bar showing the three planes (YZ, XZ, XY) aids in understanding how differential heating and cooling in different zones of a weld

joint cause non-uniform volumetric changes, which lead to residual stresses. This type of data was useful for the determination of thermal stresses which normally lead to failure in machine parts. Figures (7-10) show the model result of weld heat input; one weld passes with 5mm, 90A, 1p & Ø1.6mm.

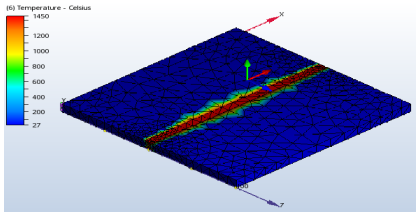

Fig. 7: 3-D Model generated

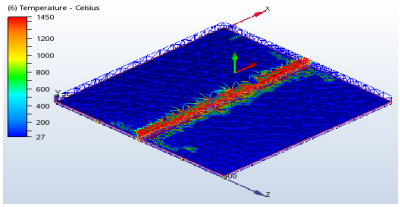

Fig. 8: Effect of weld heat input on HAZ across the Welded XZ plane along Y axis at 2.5 mm depth.

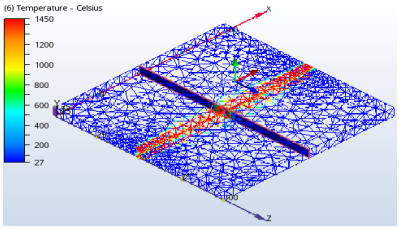

Fig. 9: Effect of weld heat input on HAZ welded area YZ plane along X axis 50 mm.

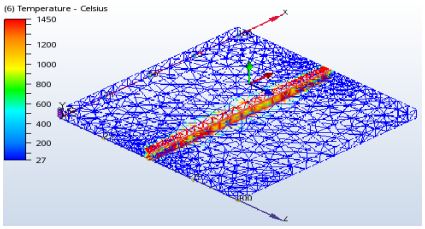

Fig. 10: Effect of weld heat input on HAZ on the welded area XY-plane along Z axis 5.2 mm away from weld centreline.

The variation of colours represented non-uniform volumetric changes in temperature at 3 mm depth below the surface of the bar. The different values of the temperature are shown in the figure. Figures (11-14) show the model result of weld heat input; one weld pass with 10 mm, 150 A, 1 p & Ø2.4 mm.

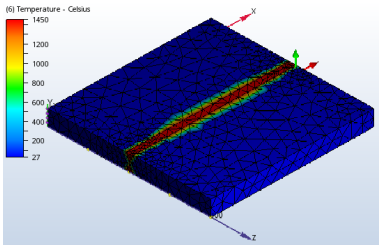

Fig.11: 3-D Model generated

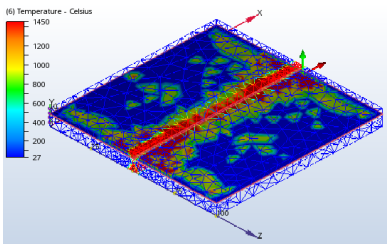

Fig. 12: Effect of weld heat input on HAZ across the welded XZ plane along Y axis at 3 mm depth

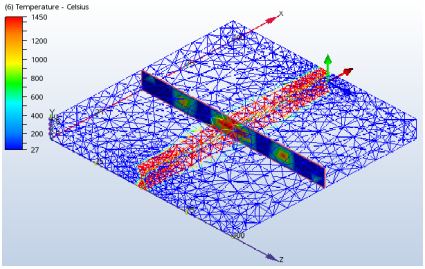

Fig. 13: Effect of weld heat input on HAZ on the welded area YZ-plane along X axis 50 mm.

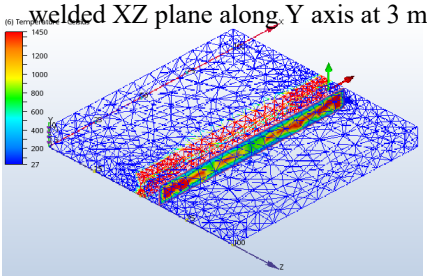

Fig. 14: Effect of weld heat input on HAZ along the welded area XY-plane along Z axis 10 mm away from weld centreline

The temperature profile of the xz-plane heat-affected zone away from the weld zone differs significantly from the bar's edges. The Figure shows non-uniform temperature distribution within the weldment away from the weld zone which altered the mechanical properties of the weldment leading to failure while in service. Figures (15-18) show the model result of weld heat input; two weld passes with 15 mm, 110 A, 1 p & Ø3.2 mm.

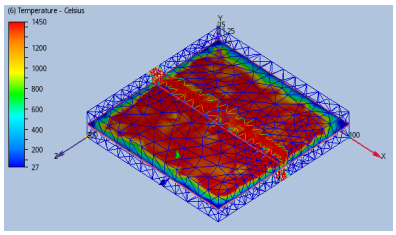

Fig. 15: 3-D Model generated

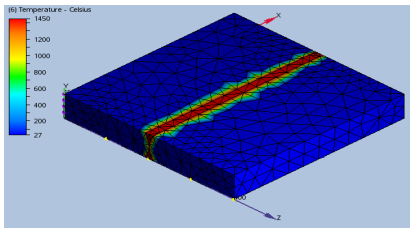

Fig. 16: Effect of weld heat input on HAZ across the welded XZ plane along Y axis at 7.5 mm depth

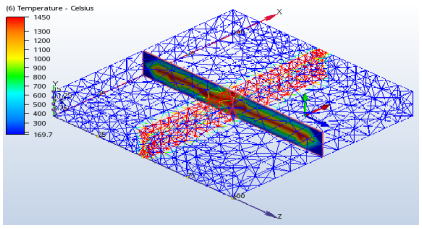

Fig. 17: Effect of weld heat input on HAZ on the welded area YZ-plane along X axis 50 mm.

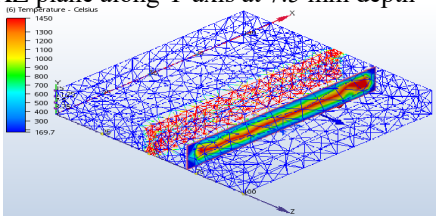

Fig. 18: Effect of weld heat input on HAZ along the welded area XY-plane along Z axis 20 mm away from weld centreline

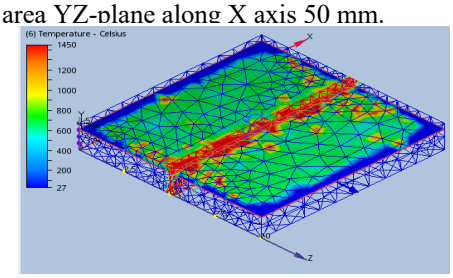

Fig.19: Effect of weld heat input on HAZ across the welded XZ-Plane along Y axis 3 mm depth.

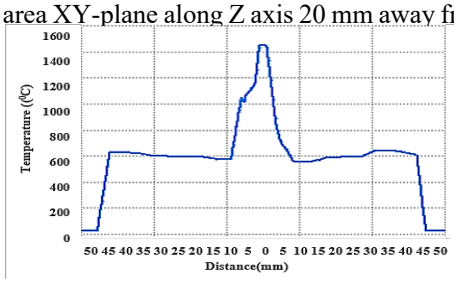

Figure 20: Temperature field against distances away from weld zone 3 mm depth.

Figure 19 illustrates non-uniform volumetric changes in temperature at 3 mm depth caused by cracks or slide lines, a material behaviour that causes the temperature to rise at some nodes/elements that form the mesh.
Tracing the nodes/elements that form the mesh on XZ-Plane across the weld zone revealed non-uniform volumetric changes in temperature presented in Figure 20. There is a decrease in temperature as it moves away from the weld zone

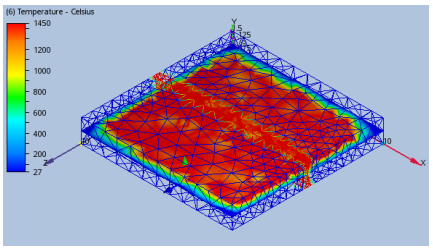

Figure 21: Effect of weld heat input on weldment XZ-Plane align to Y axis at 7 mm

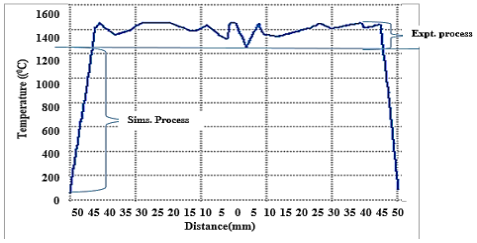

Figure 22: Temperature field against distances away from weld zone 7.5 mm depth.

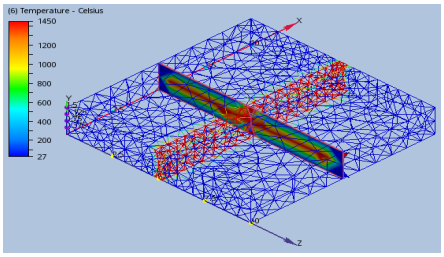

Figure 23: Effect of weld heat input on weldment at XZ-Plane along Y axis at 50 mm

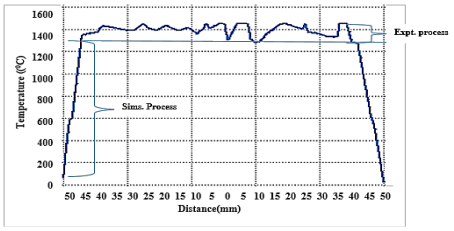

Figure 24: Temperature field against distances away from weld zone 5 mm depth.

Figures 19, 21 and 23 show the simulated welding curves and experimental welding curves which indicate the heating and cooling step on the surface of the bar, at 3 mm depth on the bar and 7.5 mm and on XZ-Plane along the Y axis at 50 mm on the bar within the weldment. The above graphs are obtained by picking nodes on the weldment which show the temperature distribution throughout the distance on the weldment. The temperature distribution obtained gradually increases to a max temperature of 1420^{0}C during the heating step and decreases to ambient temperature during the cooling step. Figures 20, 22 and 24 show the decrease in temperature as it moves away from the weld zone. Similar observations as reported by Cullen & Korkolis, 2013; Jelinek et al., 2020; Laser et al., 2017.

3.2. Effects of electrode diameter on heat flux

Figure 25 shows the effect of electrode diameter on Heat flux generated in the welded metal**.** The heat flux distribution obtained gradually decreases with an increase in metal thickness and electrode diameter.

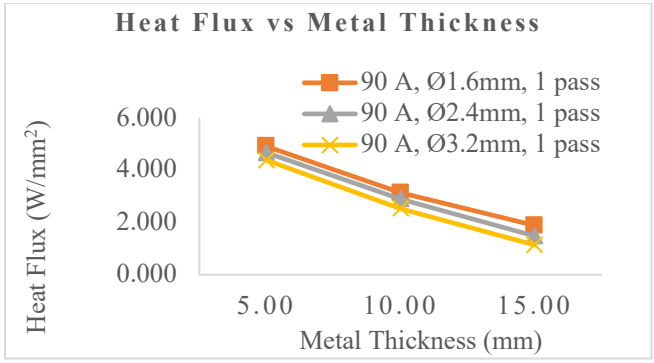

Fig. 25: Effect of Electrode diameter on Heat flux.

3.3. Effects of weld passes on heat flux

Figure 26 shows the effect of weld passes on Heat flux generated in the welded metal**.** The heat flux distribution obtained gradually decreases with an increase in metal thickness and the number of weld passes

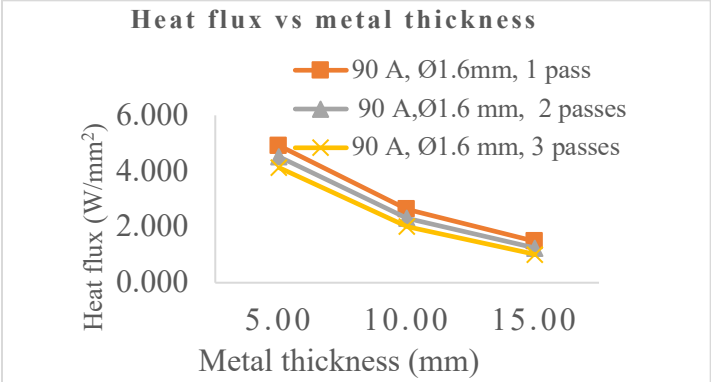

Fig. 26: Effect of weld pass on Heat flux.

3.4. Significant influence of welding parameters on heat flux

Figures 27(a-d) show the Regression Analysis with the equation as a function of Heat flux (W/mm2) versus welding parameters, which revealed that material thickness has a high significant influence on heat flux as shown in Figure 28a with a low standard deviation of 0.413816 compared to other welding parameters.

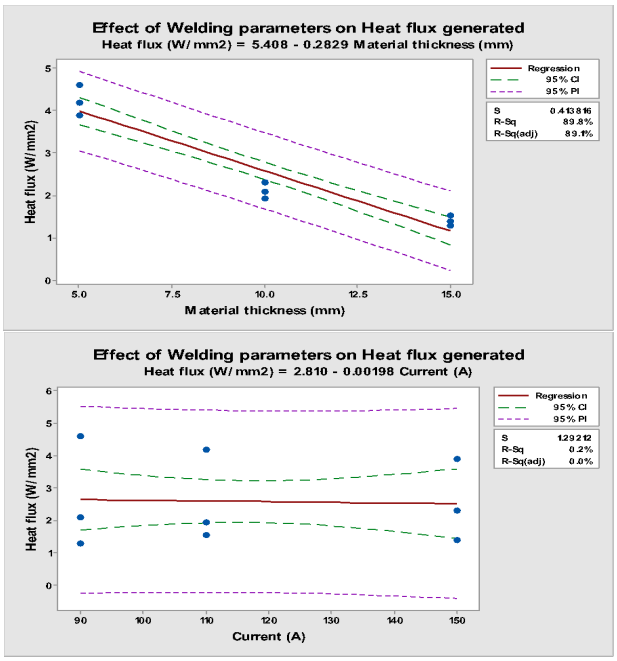

(a) (b)

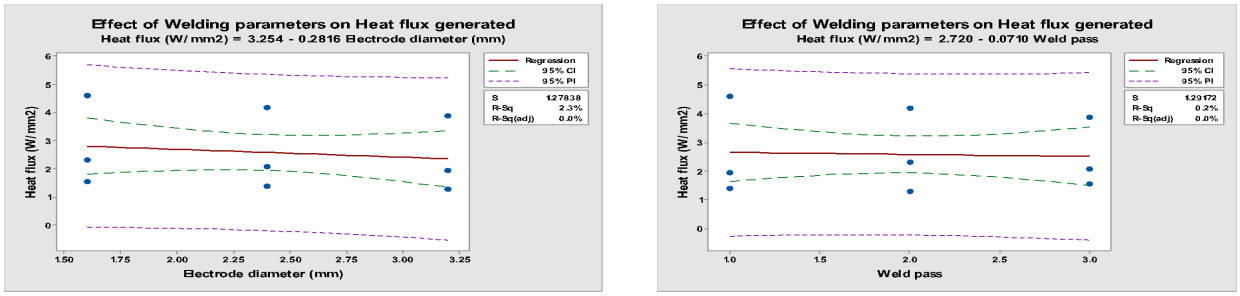

(c) (d)

Fig. 27(a- d): Effect of welding parameters on Heat flux generated in the weld metal

3.5 Typical Stress Analysis of welded metal

Von Mises stress distribution shown in Figures (28-33) was used to predict the yielding or failure of the material due to the load applied from uniaxial stress. The material experienced plastic deformation when the von Mises stress exceeded the yield strength. Based on the figures, the maximum von Mises stress plotted was 282.2 MPa (5 mm), 199 MPa (10 mm) and 158.43 MPa (15 mm) while the yield strength of the welded Cr-Mo Steel flat bar was 215MPa. Hence, the area with higher von Mises Stress above the Yield Strength experienced plastic deformation. The plastic deformation occurred mostly in the HAZ region.

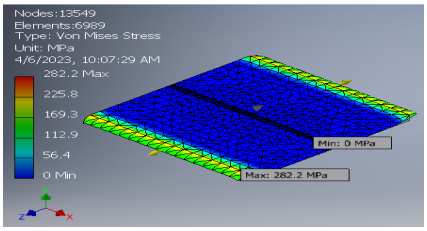

Fig. 28: Von Mises stresses on weld specimen

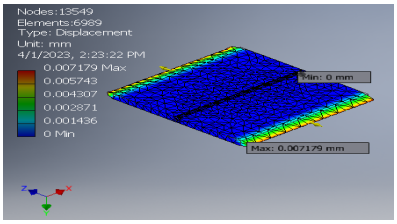

Fig. 29: Displacement on Weld Specimen

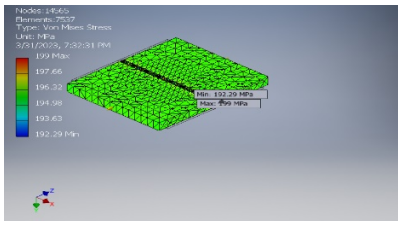

Fig. 30: Max.and Min. Von Mises stresses on welded specimen

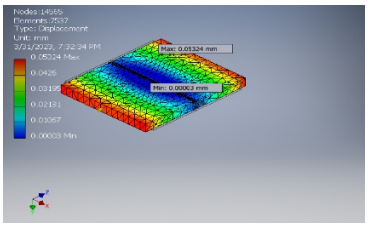

Fig. 31: Displacement on Weld Specimen

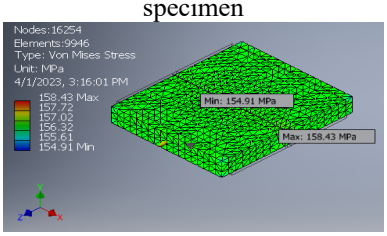

Fig. 32: Von Mises stresses on weld specimen

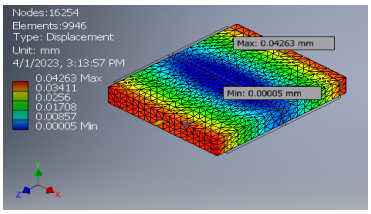

Fig. 33: Displacement on Weld Specimen

3.6 Comparison of numerical with experimental results

The variation in experimental and modelled mechanical properties of a welded Cr-Mo flat steel bar, concerning changes in material thickness and stress at break. It highlights the potential influence of factors such as increased residual stress and distortion in the weld region, changes in the microstructure of the material, and welding defects like porosity, cracking, or lack of fusion. Figures (34-35) emphasize the need to consider the specific parameters used in the model and their correspondence with the actual welding process used in the experiment. It also stresses the importance of accounting for variations in material properties, welding parameters, and testing conditions that could affect the results.

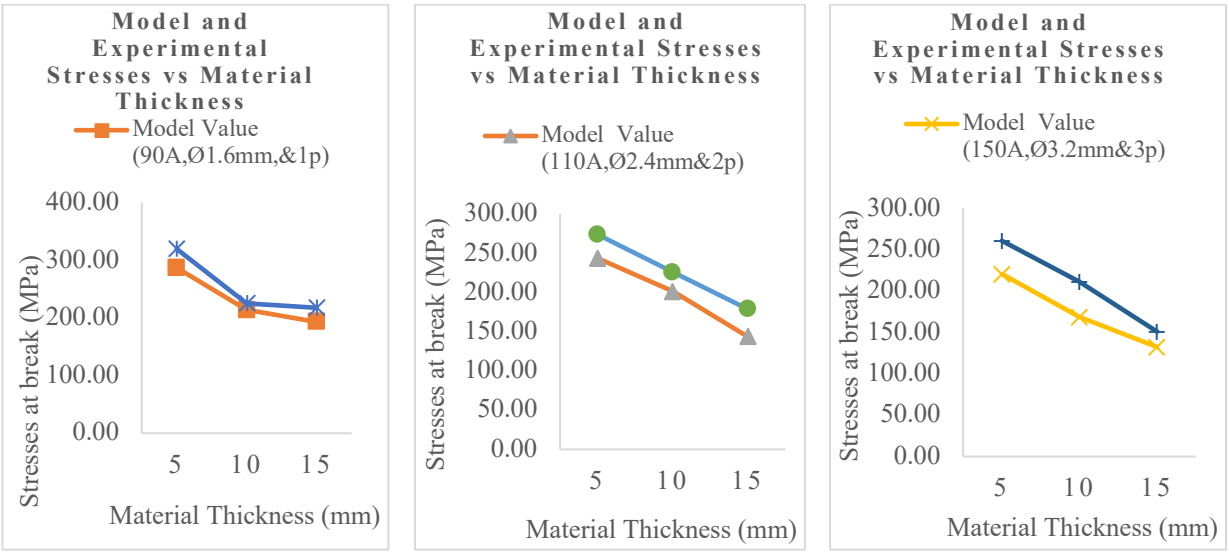

(a) (b) (c)

Fig. 34(a, b & c): Effect of weld parameters on stress in weld metal

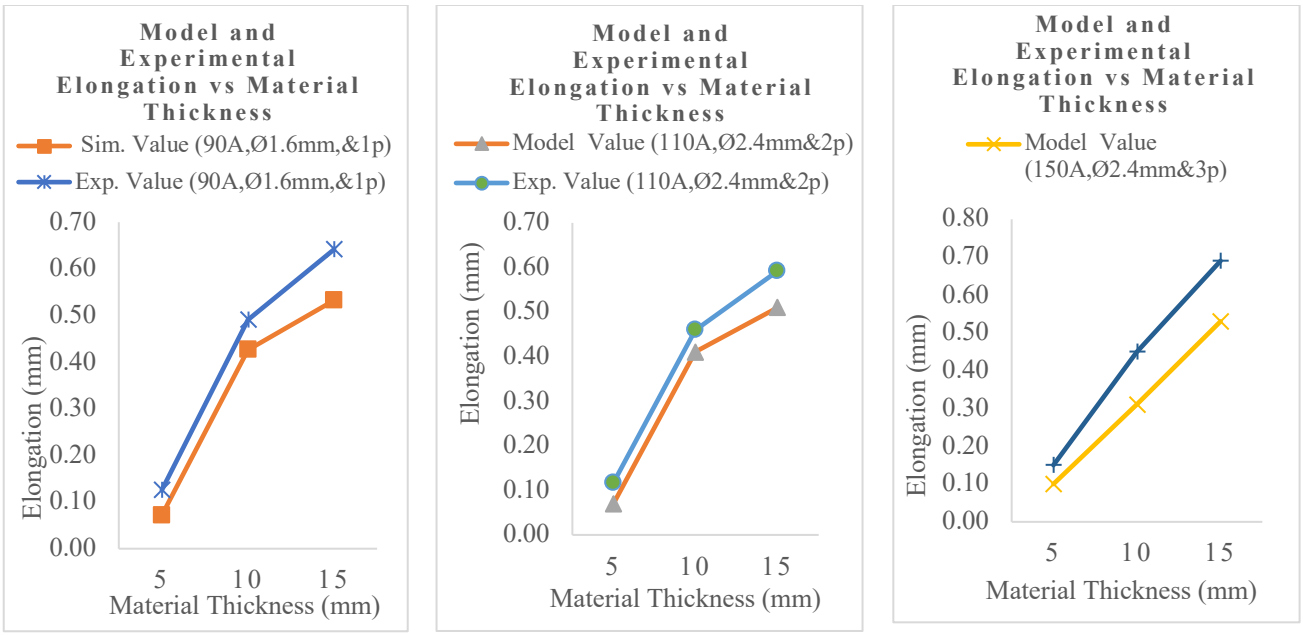

(a) (b) (c)

Fig. 35(a, b & c): Effect of weld parameters on Elongation in welded metal

3. CONCLUSIONS

It has been established that the Finite Element package, namely Autodesk Inventor and Autodesk CFD can be used to model weld heat input effect and predict material failure after the welding operation. The following specific conclusions can be drawn:

1. Von Mises stress follows tensile stress within 5-13% variation. FEA yields a safety factor of 10-12, indicating a safe design.
2. The optimum material thickness and welding current with high Von Mises stress are 5 mm and 90 A respectively.
3. Failure of fabricated machine parts can be predicted, based on the modelling results. Thus, the cost of experimental analysis can be avoided.
4. The material thickness has a great influence on the mechanical properties of the weld metal. An increase in the value of this parameter leads to a decrease in heat flux generated between 12.07 to 20.14%.

REFERENCE

Tailor, D. H., Srinivasan, K. N., Channiwala, S. A., Sohel, M., & Panwala, M. (2010). Simulation of temperature field of TIG welding using FDM. *American Society of Mechanical Engineers, Pressure Vessels and Piping Division (Publication) PVP*, *6*(PART A), 515–521. https://doi.org/10.1115/PVP2009-77697

Arpita N. Bhavsar, V. A. P. (2016). Influence of process parameters of TIG welding process on mechanical properties of SS304L welded joint. *International Research Journal of Engineering and Technology (IRJET)*, *03*(05), 977–984.

Chujutalli, J. H., Lourenço, M. I., & Estefen, S. F. (2020). Experimental-based methodology for the double ellipsoidal heat source parameters in welding simulations. *Marine Systems and Ocean Technology*, *15*(2), 110–123. https://doi.org/10.1007/s40868-020-00074-4

Flint, T. F., Francis, J. A., Smith, M. C., & Balakrishnan, J. (2017). Extension of the double-ellipsoidal heat source model to narrow groove and keyhole weld configurations. *Journal of Materials Processing Technology*, *246*(August), 123–135. https://doi.org/10.1016/j.jmatprotec.2017.02.002

Fu, G., Gu, J., Lourenco, M. I., Duan, M., & Estefen, S. F. (2015). Parameter determination of double-ellipsoidal heat source model and its application in the multi-pass welding process. *Ships and Offshore Structures*, *10*(2), 204–217. https://doi.org/10.1080/17445302.2014.937059

Hashemzadeh, M., Chen, B. Q., & Guedes Soares, C. (2015). Numerical and experimental study on butt weld with a dissimilar thickness of thin stainless steel plate. *International Journal of Advanced Manufacturing Technology*, *78*(1–4), 319–330. https://doi.org/10.1007/s00170-014-6597-6

Arpita N. Bhavsar, V. A. P. (2016). Influence of process parameters of TIG welding process on mechanical properties of SS304L welded joint. *International Research Journal of Engineering and Technology (IRJET)*, 03(05), 977–984.

Cullen, G. W., & Korkolis, Y. P. (2013). Ductility of 304 stainless steel under pulsed uniaxial loading. *International Journal of Solids and Structures*, 50(10), 1621–1633. https://doi.org/10.1016/j.ijsolstr.2013.01.020

Flint, T. F., Francis, J. A., Smith, M. C., & Balakrishnan, J. (2017). Extension of the double-ellipsoidal heat source model to narrow groove and keyhole weld configurations. *Journal of Materials Processing Technology*, 246(August), 123–135. https://doi.org/10.1016/j.jmatprotec.2017.02.002

Pu, X., Zhang, C., Li, S., & Deng, D. (2017). Simulating welding residual stress and deformation in a multi-pass butt-welded joint considering a balance between computing time and prediction accuracy. *International Journal of Advanced Manufacturing Technology,* 93(5–8), 2215–2226. https://doi.org/10.1007/s00170-017-0691-5

Reda, R., Magdy, M., & Rady, M. (2020). Ti – 6Al – 4V TIG Weld Analysis Using FEM Simulation and Experimental Characterization. *Iranian Journal of Science and Technology, Transactions of Mechanical Engineering,* 44(3), 765–782. https://doi.org/10.1007/s40997-019-00287-y

Rocha, E. J. F., De Sousa Antonino, T., Guimarães, P. B., Ferreira, R. A. S., Barbosa, J. M. A., & Rohatgi, J. (2018). Modelling of the temperature field generated by the deposition of weld bead on a steel butt joint by FEM techniques and thermographic images. *Materials Research,* 21(3). https://doi.org/10.1590/1980-5373-MR-2016-0796

Trupiano, S., Belardi, V. G., Fanelli, P., Gaetani, L., & Vivio, F. (2022). A semi-analytical method for the calculation of double-ellipsoidal heat source parameters in welding simulation. *IOP Conference Series: Materials Science and Engineering*, 1214(1), 012023. https://doi.org/10.1088/1757-899x/1214/1/012023

PAPER 163 – GREY-BASED TAGUCHI ANALYSIS FOR TRIPLE OBJECTIVE OPTIMIZATION OF TIG WELDED LOW CARBON STEEL

C. S Abima* and N. Madushele

Mechanical Engineering Science, University of Johannesburg, South Africa
*Email: cynthias@uj.ac.za

ABSTRACT
The welding process remains one of the most value-adding techniques in the industry, especially for fabrication and repair purposes. Present scenario report that increasing hardness reduces ductility and percentage elongation properties which are equally essential for structural integrity. Against this backdrop, this study adopts the grey base-Taguchi method to investigate the process parameters combination that results in an optimum balance of tensile strength, hardness, and elongation at break point for the Tungsten Inert Gas welding of low-carbon steel joints. L9 Taguchi matrix is adopted towards maximizing the triple functions. A single grade for the responses was established, followed by ANOVA and signal-to-noise ratio analysis. A confirmatory test followed by a repeat showed a 0.257 improvement in the grey relational grade which validates the effectiveness of the method in achieving the triple-objective functions. The study benefits the scientific and industrial bodies by providing the process window for maximizing the tensile strength and hardness properties of welded joints in a way that the increased hardness properties do not compromise the elongation at break hence making the joint susceptible to brittle failure.

KEYWORDS: Grey-based Taguchi, Triple objective optimization, Tensile strength, Hardness and Percentage elongation

1. INTRODUCTION

Welding is an efficient metal joining process widely used in various sectors, such as automobiles, aircraft, buildings, marine etc. (Vidyarthy & Sivateja, 2020). It is one of the most value-adding processes in the manufacturing industry, especially for repair and fabrication purposes. The integrity of the welded assembly or repaired components depends on the resultant mechanical properties of the joints (C. Abima et al., 2021). These mechanical properties are influenced by numerous factors, including welding technique, heat input, temperature gradient, microstructural presentation and weld defects (C. S. Abima et al., 2021; Nguyen & Kim, 2020; Pan et al., 2022). Of the numerous welding techniques, tungsten inert gas (TIG) is widely used due to its ability to weld a wide range of materials, high efficiency, high-quality joints, high deposition rate, easy operating principle, and lower cost. The tensile and hardness properties of TIG welded joints have been investigated by several studies in a bit to determine the influence of process parameters on the resultant joint quality. For instance, (İrsel, 2022) has reported increased yield strength and tensile strength for low carbon steel (S235JR) welded by TIG welding with ER30L filler wire. The authors attributed these strength improvements to an increase in hardness properties as a result of delta-ferrite phase formation. Another author reported that the tensile strength and elongation decrease as preheat temperature increases but increase as the welding current increases (Kumar & Singh, 2019). Still, in the pursuit for better mechanical properties, several researchers have adopted various optimization methods such as Taguchi, response surface methodology, etc. (Ghuge et al., 2022). For example (Shanmugasundar et al., 2019) optimized the TIG welding process by considering the gas flow rate, current and nozzle distance for optimal tensile strength. Their result shows that the welding current mainly influences the ultimate tensile. Taguchi optimization analysis of TIG welded joints reported by (Ghumman et al., 2022) shows that the hardness values and tensile strength were mostly influenced by increased arc current as gas flow rate. The study of (Joseph et al., 2017) also showed that the tensile strength of the welds were most influenced by the welding voltage and current. Lower level settings of these parameters matrix by Genetic algorithm and response surface methodology favourd the tensile strength.

Because the structural integrity of weldment is judged by combined mechanical properties rather than single responses, it became imperative to adopt a system capable of optimizing multiple objective properties. To achieve this, the grey-based Taguchi method was introduced. This method overcomes the limitation of a single function or response per an analysis of the conventional Taguchi method (Wakchaure et al., 2018). For example, the grey-based approach was adopted by (Mohanty et al., 2021) to optimize the tensile and hardness properties of 0.002% C steel welded via the

TIG welding process on a higher the better criteria. The tensile strength and hardness value increase with increased current, voltage and speed. Another study reports the parameter optimization of pulsed TIG welded Monel 400 AISI and AISI 304 steel dissimilar joints to maximize the tensile strength and percentage elongation and minimize the heat-affected zone (Avinash et al., 2019). The authors reported that the pulse frequency most influenced the grey relational grade (GRG) and that a confirmatory test showed an increase in the percentage elongation, tensile strength and a reduced heat-affected zone of the weldment. (Vinoth et al., 2021) reported that lower current welding speed with intermediate gas flow rate gave the optimal result for grey relational grade analysis of TIG welded 316 for improved corrosion, impact and tensile strength.

Although a variety of TIG welding process parameters have been investigated to optimize dual objectives such as tensile strength and elongation or tensile strength and hardness, reports show that the hardness of steel increases with increasing tensile strength (Angst et al., 2001) (Zhang et al., 2011). However, increasing hardness reduces percentage elongation and thus leads to brittle failure, which is detrimental to structural members. For structural applications, these three qualities are required at their optimum (Zhang et al., 2011) without an appreciable trade-off. Following this, the Grey-based Taguchi optimization is adopted in this study to optimize the triple functions for the structural integrity of AISI 1008 TIG welded joints.

2. MATERIALS AND EXPERIMENTAL PROCEDURE

2.1 Materials and equipment

The welding procedure was carried out with 100 x 100 x 6 mm AISI 1008 plates welded by the conventional TIG welding machine and a 2.4 mm diameter ER70S/6 filler electrode in a butt joint configuration. The elemental weighted composition of AISI 1008 and the filler electrode are presented in Table 1.

Table 1 Chemical composition of AISI 1008ER70S/6 filler metal

Element symbol	C	S	P	Mn	Si	Cr	Mo	Ni	Al	Fe	V	Cu
AISI 1008	0.072	0.009	0.001	0.32	0.07	0.042	0.005	0.006	0.042	Bal	-	-
ER70S/6	0.06	0.035	-	1.4	0.8	0.15	0.15	0.15	-	-	0.03	0.5

2.2 Welding parameters, responses and design matrix

Three factors in three levels were selected for the experimental design matrix to optimize the triple functions. A thorough literature survey aided the choice process parameters adopted in this study. Welding voltage (levels- 10, 15, 20), current (levels- 140, 160, 180), and gas flow rate (levels- 15, 17, 19) were the selected process parameter and their respective levels. On the other hand, the desired output responses are the tensile strength, percentage elongation and hardness. The design matrix was achieved by adopting the Taguchi statistical method. In contrast to the traditional trial-and-error approach, the Taguchi method enables limited experimental runs to provide ideal and optimal results. Table 2 shows the L9 orthogonal matrix of the welding process parameters.

Table 2 Matrix design for Experimental run

Sample	Input process parameters		
Run	Voltage (V)	Current (A)	Gas flow rate L/mm
T-L1	10	140	15
T-L2	10	160	17
T-L3	10	180	19
T-L4	15	140	17
T-L5	15	160	19
T-L6	15	180	15
T-L7	20	140	19
T-L8	20	160	15
T-L9	20	180	17

2.3 Welding and mechanical test procedures

The rust layer due to oxidation was removed by surface grinding and cleaned by acetone a few minutes before the welding operation. Shielding of the weld pool was achieved by crystal argon gas. Following the completion of the welding, test pieces for tensile and hardness analysis are cut off. Three replicate specimens were machined for each parameter in accordance with ASTM standards E8/E8M and tested using an axail testing machine. The weld hardness properties were tested using the digital Indentec Vickers microhardness test machine according to ASTM E384 standard, at a dwell time of 15 seconds, and a 300N impression force by a diamond indenter travelling a distance of 0.2mm for each indent across the sample length.

2.4 Analytical methods

The TIG welding process parameters were multi-objectively optimized for maximum tensile strength, percentage elongation, and hardness value using the grey-based Taguchi technique. When evaluating the strength of the links between sequences, grey relational analysis is helpful. It combines many output responses into a single output response by assigning Grey Relational Grade (GRG) values to discrete output responses. The signal-to-noise ratio (S/N) and the ANOVA analysis were computed using the Minitab 17 application.

3. RESULTS AND DISCUSSION

3.1 Physical observation of welds

All welds have good front and rear bead appearance, as shown in Figure 1. There were no physical flaws like pores, splatter, or fractures. The backside of every weld bead had likewise fused completely.

3.2 Tensile and Hardness Results

The ultimate tensile strength (UTS) and percentage elongation (% Ɛ) of the welded specimen under loading conditions have been determined using axial tensile testing. These properties are crucial as they determine the strength and the stress-strain relationship of components and structures. All tested specimens failed at the base material region, indicating strong joint connections. Only the hardness values (HV) for the heat-affected zone is taken into account in this study. The result (Table 3) presents an average of the three replicate tested samples.

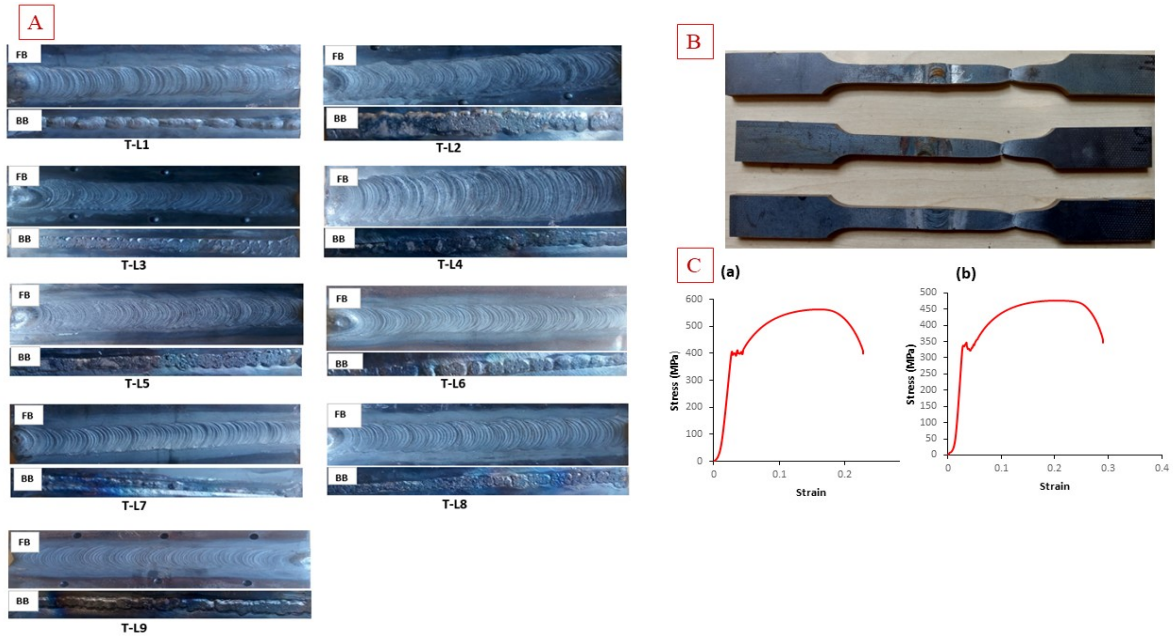

Figure 1 (A) welded specimens (B) fractured specimens (C) representative stress-strain

Table 3 Results from the experiment

Input Parameters						Experimental outcomes		
Sample runs	Voltage (V)	Current (A)	Gas flow rate (L/min)	Welding speed	Heat input	UTS (MPa)	% Ɛ	HV
T-L1	10	140	15	36.93	1592.2	389.0	23.6	159.7
T-L2	10	160	17	36.93	1819.7	338.3	28.3	126.9
T-L3	10	180	19	38.72	1952.5	399.0	24.1	150.8
T-L4	15	140	17	35.30	2498.6	386.0	21.5	133.7
T-L5	15	160	19	33.33	3024.3	389.5	25.5	134.7
T-L6	15	180	15	30.00	3780	476.6	24.1	154.8
T-L7	20	140	19	34.28	3430.6	306.2	23.4	153.2
T-L8	20	160	15	35.30	3807.4	394.7	25.1	152.8
T-L9	20	180	17	40.00	3780	335.5	25.2	131.6

3.3 Grey relational analysis

The ideal process parameter combination that maximizes the intended responses based on larger-is-better criteria is found using the grey-based Taguchi approach. Equation 1 is used to first normalize the experimental data before Equation 2 computes the data set's deviation sequence. Finally, Equations 3 and 4 are used to derive the grey relational coefficient and the grey relational grades (GRG). The data for the grey-relational analysis are shown in Table 4.

$$x_i^*(k) = \frac{x_i(k) - \text{Min}\, x_i(k)}{\text{Max}\, x_i(k) - \text{Min}\, x_i(k)} \qquad \text{Data normalization (the larger-the-better)} \qquad (1)$$

where = $x_i^*(k)$ is the normalized value, $x_i(k)$is the target value, Min $x_i(k)$ is the lowest value of $x_i(k)$, and Max $x_i(k)$ is the highest value of $x_i(k)$

i = 1, 2, 3…,m. and k =1, 2, 3…,n. m and n are the number of experimental data and the number of responses, respectively.

$$\xi_i(k) = \frac{\Delta_{Min} + \xi\Delta_{Max}}{\Delta_{oi} + \xi\Delta_{Max}} \qquad \text{Grey relational coefficient} \qquad (2)$$

where $\xi_i(k)$ = grey coefficient, Δ_{oi} = deviation sequence, $\Delta_{Min}\ and\ \Delta_{Max}$ = minimum and maximum values of Δ_{oi} for all the sequences, and ξ = the identification coefficient. The identification coefficient of 0.5 is utilized to produce equal weightage for both quality response factors.

$$\Delta_{oi} = \|x_o(k) - x_i(k)\| \qquad \text{Deviation sequence} \qquad (3)$$

$$y_i = \frac{1}{n}\sum_{k-1}^{n} \xi_i(k) \qquad \text{Grey relational grade} \qquad (4)$$

where y_i is the GRG for the ith experimental run, and n is the number of characteristic response

Table 4 Grey relational analysis

Runs	Sequence deviation			Grey relational coefficient			GRG	Ranking
	UTS	% Ɛ	HV	UTS	% Ɛ	HV		
T-L1	0.514	0.691	0.000	0.493	0.420	1.000	0.638	2
T-L2	0.812	0.000	1.000	0.381	1.000	0.333	0.572	4
T-L3	0.455	0.618	0.271	0.523	0.447	0.648	0.540	5
T-L4	0.532	1.000	0.793	0.485	0.333	0.387	0.402	9

T-L5	0.511	0.412	0.762	0.494	0.548	0.396	0.480	7
T-L6	0.000	0.618	0.149	1.000	0.447	0.770	**0.739**	**1**
T-L7	1.000	0.721	0.198	0.333	0.410	0.716	0.486	6
T-L8	0.481	0.471	0.210	0.510	0.515	0.704	0.576	3
T-L9	0.829	0.456	0.857	0.376	0.523	0.369	0.423	8

Minitab 17 software has been used to calculate the main effect plots for the signal-to-noise ratio (S/N) and the mean effect plot for means. The response table for means corresponding to the values of the GRGs (Table 5) shows that the optimum parameter set is Voltage 1 - Current 3 – Gas flow rate 1, i.e. voltage = 10 V, current = 180 A, gas flow rate = 15L/min. The ranking shows that the gas flow rate had the most influence on the GRG, followed by the welding voltage.

Table 5 Response table for means

Level	Voltage (V)	Current (A)	Gas flow rate L/min
1	**0.5833**	0.5087	**0.6510**
2	0.5403	0.5427	0.4657
3	0.4950	**0.5673**	0.5020
Delta (Max-Min)	0.0883	0.0587	0.1853
Rank	2	3	1

The overall grade for grey relations = 0.5396

Figure 2 shows that a change in any of the process parameters affects the output response. The GRG decreases with increasing voltage and increases with increasing current. On the other hand, the GRG first decreased and then increased slightly with an increased gas flow rate. Changes in the gas flow made a significant change in the GRG.

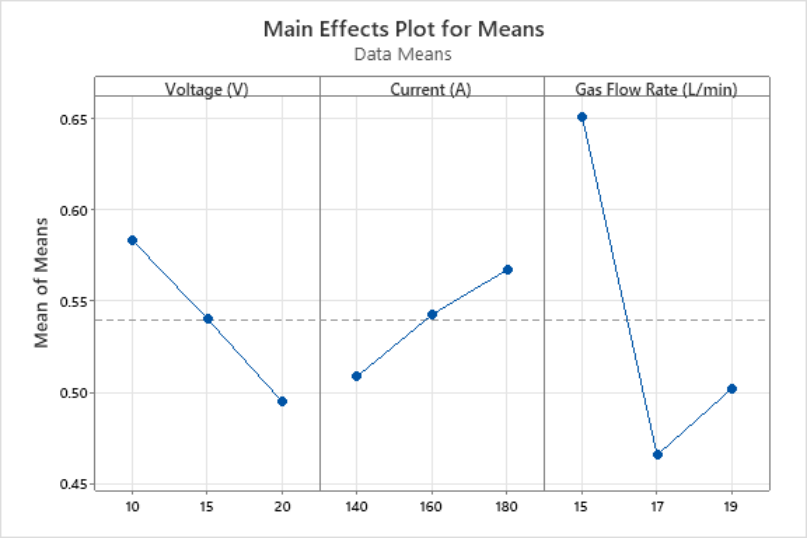

Figure 2 The main effects plot for means

3.5 Analysis of Variance

Analysis of variance (ANOVA) demonstrates the relative percentage contribution and level of significance of each parameter's influence at a 95% confidence level. Table 6 shows that the flow rate had the most influence on the GRG, with a 36.69% contribution, followed by the welding voltage with 12.89%.

Table 6 ANOVA for the transformed response

Source	DF	Seq SS	Contribution	Adj SS	Adj MS	F-Value	P-Value
Regression	3	0.050168	55.27%	0.050168	0.016723	2.06	0.224
Voltage	1	0.011704	12.89%	0.011704	0.011704	1.44	0.284
Current	1	0.005163	5.69%	0.005163	0.005163	0.64	0.461
Gas Flow Rate	1	0.033301	36.69%	0.033301	0.033301	4.10	0.099
Error	5	0.040604	44.73%	0.040604	0.008121		
Total	8	0.090772	100.00%				

3.6 Confirmatory experiment

With the values of the optimum set of process parameters (Voltage 1 - Currentn 3– Gas flow rate 1, i.e. voltage = 10 V, current= 180 A, gas flow rate = 15L/min) acquired for the GRG, a confirmation experiment was carried out to validate predicted against experimental results. The obtained tensile strength, percentage elongation and hardness values for these optimum set of parameters are 486 Mpa, 25.3% and 158 HV, respectively. These values are compared with the initially obtained optimum parameters with the highest ranking for the GRG, i.e. voltage = 15 V, current= 180 A, gas flow rate = 15L/min). The GRG value obtained for the predicted optimal parameters is 1.0485, suggesting a high level of similarity. In the confirmation experiment, which incorporated the initial data and confirmation test results, a GRG value of 1.000 was achieved, indicating a perfect match. Both experiments demonstrated favourable and accurate outcomes, reinforcing the validity of the predicted optimal parameters and the success of the confirmation experiment.

$$\hat{y} = y_m + \sum_{i=1}^{n}(\hat{y} - y_m)\,, \qquad (5)$$

where y_m is the total mean GRG, $\hat{y}$ is the GRG at the optimal level of each process parameter, and n is the number of significant parameters.

The confirmation test results in Table 7 reveal a close match between the predicted and experimental GRG values. The optimal parameter settings significantly enhance the grey relational grade of the responses, particularly the tensile strength and yield strength, by a notable improvement of 0.0489. This indicates the effectiveness of the chosen parameter combination in improving the desired mechanical properties.

Table 7. Confirmation results

	Initial optimal parameters	Optimal parameters from S/N of GRG	
		Predicted	Experimental
level	Voltage 2- Current 3- Gas flow rate 1	Voltage 1- Current 3 - Gas flow rate 1	Voltage 1- Current 3- Gas flow rate 1
UTS (MPa)	476.6		396
% Ɛ HV	24.1		25.3
HV	154.8		153
GRG	0.739	0.5968	0.854

Improvement in GRG = 0.257

4. CONCLUSION

Grey-based Taguchi optimization technique for triple function optimization of process parameters in TIG welding for AISI 1008 is reported for a total of nine runs produced following the L9 orthogonal matrix. The study show that obtaining a high strength and hardness weldment that exhibit favourable percentage elongation to avoid brittle joints is possible by adopting the grey-based Taguchi method.

To attain optimal tensile strength, percentage elongation, and hardness, the recommended parameters are voltage at 10 V, current at 180 A, and gas flow rate at 15 L/mm. More so, the set of optimal parameters resulted in higher values for all the measured outcomes. According to the ANOVA analysis, the gas flow rate is the mos program influential parameter impacting the ultimate tensile strength.
This result also shows that high-level current, low voltage, and low gas flow settings gave the best tensile, hardness, and ductile behaviour suitable for industrial applications.

ACKNOWLEDGEMENT

The authors acknowledgement the University of Johannesburg for granting a research fund.

REFERENCES

Abima, C., Akinlabi, S., Madushele, N., & Akinlabi, E. (2021). Process Parameters Optimization for GMA Welding of AISI 1008 Steel Joints for Optimal Tensile Strength Revue des Composites et des Matériaux Avancés-Journal of Composite and Advanced Materials Process Parameters Optimization for GMA Welding of AISI 1008 S. *Revue Des Composites et Des Matériaux Avancés*, *6*(December), 349–354. https://doi.org/10.18280/rcma.310606

Abima, C. S., Akinlabi, S. A., Madushele, N., Fatoba, O. S., & Akinlabi, E. T. (2021). Multi-objective optimization of process parameters in TIG-MIG welded AISI 1008 steel for improved structural integrity. *International Journal of Advanced Manufacturing Technology*, *https://doi.org/10.1007/s00170-021-08181-1*. https://doi.org/10.1007/s00170-021-08181-1

Angst, J., Sellar, R., & Merikangas, K. R. (2001). On the tensile strength and hardness relation for metals. *Journal of Materials Engineering and Performance*, *10*(6), 718–722. https://doi.org/10.1361/105994901770344601

Avinash, S., Balram, Y., Sridhar Babu, B., & Venkatramana, G. (2019). Multi-response optimization of pulse TIG welding process parameters of welds AISI 304 and Monel 400 using grey relational analysis. *Materials Today: Proceedings*, *19*, 296–301. https://doi.org/10.1016/j.matpr.2019.07.211

Ghuge, N. C., Palande, D. D., & Belkhode, P. B. (2022). Optimization of Cutting Parameters using the RSM-Desirability Approach in the MQL-Assisted Turning of AISI 4130. *Nigerian Journal of Technological Development*, *19*(4), 316–323. https://doi.org/10.4314/njtd.v19i4.4

Ghumman, K. Z., Ali, S., Din, E. U., Mubashar, A., Khan, N. B., & Ahmed, S. W. (2022). Experimental investigation of effect of welding parameters on surface roughness, micro-hardness and tensile strength of AISI 316L stainless steel welded joints using 308L filler material by TIG welding. *Journal of Materials Research and Technology*, *21*, 220–236. https://doi.org/10.1016/j.jmrt.2022.09.016

İrsel, G. (2022). Study of the microstructure and mechanical property relationships of shielded metal arc and TIG welded S235JR steel joints. *Materials Science and Engineering A*, *830*. https://doi.org/10.1016/j.msea.2021.142320

Joseph, J., Muthukumaran, S., & Joseph, J. (2017). Optimization of activated TIG welding parameters for improving weld joint strength of AISI 4135 PM steel by genetic algorithm and simulated annealing. *Int J Adv ManufTechnol*, *93*, 23–34. https://doi.org/10.1007/s00170-015-7599-8

Kumar, S., & Singh, R. (2019). Optimization of process parameters of metal inert gas welding with preheating on AISI 1018 mild steel using grey based Taguchi method. *Measurement*, *148*, 106924. https://doi.org/10.1016/j.measurement.2019.106924

Mohanty, S., Mohanta, G. K., Senapati, A. K., & Rath, K. C. (2021). Taguchi grey relational analysis for optimal process parameter of low carbon steel welded by GTAW by using ER309L filler material. *Materials Today: Proceedings*, *44*, 2556–2561. https://doi.org/10.1016/j.matpr.2020.12.631

Nguyen, N. V., & Kim, S. E. (2020). Experimental study to investigate microstructure and continuous strain rate

sensitivity of structural steel weld zone using nanoindentation. *International Journal of Mechanical Sciences*, *174*. https://doi.org/10.1016/j.ijmecsci.2020.105482

Pan, M., Li, Y., Sun, S., Liao, W., Xing, Y., & Tang, W. (2022). A Study on Welding Characteristics, Mechanical Properties, and Penetration Depth of T-Joint Thin-Walled Parts for Different TIG Welding Currents: FE Simulation and Experimental Analysis. *Metals*, *12*(7). https://doi.org/10.3390/met12071157

Shanmugasundar, G., Karthikeyan, B., Santhosh Ponvell, P., & Vignesh, V. (2019). Optimization of process parameters in TIG welded joints of AISI 304L -austenitic stainless steel using taguchi's experimental design method. *Materials Today: Proceedings*, *16*, 1188–1195. https://doi.org/10.1016/j.matpr.2019.05.213

Vidyarthy, R. S., & Sivateja, P. (2020). Influence of activating flux tungsten inert gas welding on mechanical and metallurgical properties of the mild steel. *Materials Today: Proceedings*, *28*, 977–981. https://doi.org/10.1016/j.matpr.2019.12.335

Vinoth, V., Sudalaimani, R., Ajay, C. V., Kumar, C. S., & Prakash, K. S. (2021). Materials Today : Proceedings Optimization of mechanical behaviour of TIG welded 316 stainless steel using Taguchi based grey relational analysis method. *Materials Today: Proceedings*, *45*, 7986–7993. https://doi.org/10.1016/j.matpr.2020.12.1002

Wakchaure, K. N., Thakur, A. G., Gadakh, V., & Kumar, A. (2018). Multi-Objective Optimization of Friction Stir Welding of Aluminium Alloy 6082-T6 Using hybrid Taguchi-Grey Relation Analysis- ANN Method. *Materials Today: Proceedings*, *5*(2), 7150–7159. https://doi.org/10.1016/j.matpr.2017.11.380

Zhang, P., Li, S. X., & Zhang, Z. F. (2011). General relationship between strength and hardness. *Materials Science and Engineering A*, *529*(1), 62–73. https://doi.org/10.1016/j.msea.2011.08.061

PAPER 164 – ADDITIVE MANUFACTURING IN MODERN DENTISTRY: STATE OF THE ART AND FUTURE PROSPECT

C. S Abima[1*] and N. Madushele[2]

[1]Mechanical Engineering Science, University of Johannesburg, South Africa
[2]Biomedical Engineering and Healthcare Technology Research Centre (BEAHT RC) University of Johannesburg, South Africa

*Email: cynthias@uj.ac.za, oyamacythia@gmail.com

ABSTRACT
The adoption of additive manufacturing in dentistry has initiated sufficient growth in the manufacturing of dentures. Despite the potential for improving healthcare at a low cost, the integration of additive manufacturing in dentistry has been deemed to be slow. The call for research and development to improve its adoption in the delivery of dental treatment is evident in past studies. This paper reviews recent studies on additive manufacturing in dental treatment. A scientometric review is presented to identify the different research trends and the current research focus through Voswier visualization software using a bibliometric approach. The findings revealed that only developed and a few developing countries are actively involved in research publications in this field. This result is worrisome as the cases of dental disease and people needing denture replacement continue to rise across the globe. The root cause of this has also been studied and evaluated in this study. This research contributes to the existing body of knowledge by synthesizing state-of-the-art research on additive manufacturing in modern dentistry. Furthermore, the study highlights the sustainable benefits of additive manufacturing in prosthodontics.

KEYWORDS: 3D printing, additive manufacturing, CAM/CAD, modern dentistry, digital dentistry, dentures, prosthodontic

1. INTRODUCTION

Complete removable dentures have been used to reinstall patients with edentulism for a long time (Arutyunov et al., 2022; Pradhan et al., 2022). Before the introduction of advanced manufacturing processes, dentures were fabricated by conventional methods such as milling and lost-wax techniques (Anadioti et al., 2020). Technological advancement led to the introduction of digital dentistry in the 1980s (T et al., 2009). After the first attempt at fabricating dentures by developing a computer-aided-design/computer-aided manufacturing (CAD/CAM) model in 1994 (Tamburrino et al., 2022), (Goodacre et al., 2012) launched the construction of digital dentures. Since then, digital dentistry has changed the practice of dentistry in many areas. For instance, 3D printers can produce models for patients before surgery, allowing them to visualize the operation and result, enhancing patient compliance and acceptability. In addition, digital manufacturing procedures in dentistry improve patient healthcare in the early treatment phase and guarantee accurate capturing of patient diagnoses with the help of dental scanners (Hoang et al., 2016), (Güth et al., 2017). Patient data obtained by precise scanning is now further transferred to CAD/CAM programming software to plan and fabricate required dentures models and structures (Stanley et al., 2018; Tamburrino et al., 2022). Interestingly, manufactured dentures are more affordable for patients since employing CAD/CAM lowers the cost of dental restoration, eliminating the need for temporary crowns and bridges during treatment and reducing the number of doctor appointments. Therefore, the patient can replace dentures within a short time frame at a lower cost and zero risk.

The frameworks for removable dentures, and temporary and fixed bridge dentures have traditionally been fabricated using formative manufacturing approaches (such as the lost-wax technique, alginate impression and flasking methods). These conventional formative techniques are manual, laborious, material and time-consuming, involving several steps where mistakes are likely to happen. In modern/digital dentistry, subtractive and additive manufacturing processes are employed for dental fabrication. The traditional subtractive method becomes unsuitable when fabricating tin and complex shapes with undercut areas. Moreso, the efficient removal of material from a workpiece in milling operations requires heavy cutting forces. These heavy forces produce vibrations that place the workpiece under some degree of thermal and mechanical stress. This, especially with thin parts, may lead to dimensional distortion (Hagman & Svanborg, 2022).

These challenges, coupled with numerous discomfort, urgently necessitated an automatic procedure for dental manufacturing. The huge amount of waste associated with subtractive processes (Kalberer et al., 2019; Srinivasan et al., 2021) and the unaesthetic appearance (Li et al., 2020) of the manufactured product makes additive manufacturing a better choice (Awasthi et al., 2021; Rouf, Malik, et al., 2022).

Additive manufacturing is a layer-by-layer deposition of materials to create a piece (Čretnik & Fekonja, 2022; Ferchow et al., 2022; Galante et al., 2019; Rekow, 2020; Su et al., 2020). Among the numerous advantages of additive manufacturing in dental applications are the speed and accuracy offered by dental 3D printers. Multiple parts can be printed simultaneously once the digital copies are available and can fit on the bed. This means that technicians begin part production once the scan copy arrives [26], reducing delivery time for patient treatments and improving data retention (Anadioti et al., 2020). These advantages promotes additive manufacturing in dentistry ranging from prosthodontics, maxillofacial surgery, and oral implantology to orthodontics, endodontics, periodontology, biomedical and pharmaceutical markets (Al-Dulimi et al., 2021; Sheoran et al., 2020; Silva et al., 2017; Singh & Ramakrishna, 2017). Several researchers have studied various aspects of 3D printing in dentistry. For instance, (Punia et al., 2022) elaborated on various 3D printing techniques and the materials used in dental applications. (Rouf, Raina, et al., 2022) further studied the mechanical properties of 3D printed parts for dental applications. (Tian et al., 2021) also presented a classification and characteristics of additive manufacturing technologies adopted in dentistry. The authors also highlighted the factors affecting 3D printing technology. (Osman et al., 2017) also reported that digital light processing of zirconia dental implants presented desirable dimensional accuracy and excellent surface finish. The market for dental 3D printing is anticipated to grow from USD 3.2 billion in 2022 to USD 7.9 billion in 2027 at a CAGR of 20.2% (Tamimi & Hirayama, 2019). American College of Prosthodontists record reveals that about 120 million Americans are missing at least one tooth, and over 36 million are completely edentulous (Akl & Stendahl, 2022). Over 200 million Americans are anticipated to have partial dentures in the next 15 years, and 2.3 million implant-supported crowns are created each year.

Currently, North America dominates the 3D printing market, having above 35 per cent of the market share, followed by Europe (Akl & Stendahl, 2022). North America takes the lead due to the growing incidence of dental caries & gum disease, the ageing population, the high cost of oral care, the increasing demand for aesthetic dentistry, and the expanding acceptance of digital dentistry. African countries are still at the bottom of this list due to slow growth resulting from limited funding for establishing digital manufacturing stations or laboratories (Campbell et al., 2019). (Tiwari et al., 2021) reported an increased burden of dental diseases in South Africa. The authors stated that limited dental specialists and dental services are available to care for the increased dental issues in South Africa. (Dizon et al., 2018) also estimated a 22.3% increase in the adoption of additive manufacturing processes in the next few years.

It becomes crucial to evaluate the research associated with additive manufacturing in dentistry, the organizations involved, regional and international contributions to the field, and priority themes that are likely to influence the agendas for research advancements to visualize the application of additive manufacturing in dentistry. A road map of knowledge areas through the identification of research patterns is needed to future broaden the growth of additive manufacturing in dental applications. Therefore, using the VOSviewer program, the study objective is to undertake a scientometric examination of the scholarly output on the subject of 3D printing in dentistry between 2008 and 2022.

2. RESEARCH METHODOLOGY

The data used for this study was retrieved on the 7th of April 2023 from the University of Johannesburg Library Scopus database. Published articles were sourced using the following terms “dentistry, 3D printing, additive manufact*”. The Boolean operators “OR” and “AND” were used to connect the search queries. The search period ranges from 2008 to 2022, a period of 15 years. The initial search within the year range resulted in a total of 286 documents. After filtering to limit the search terms to dentistry application, document type and limited to English language, a total number of 188 documents (146 journal articles (77.7 %), 26 (13.8%) conference proceedings and 16 (8.5%) book chapters) were obtained. Their full records, including authors, article titles, affiliation countries, document sources and abstracts, were downloaded in CSV format. The VOSviewer software was used to map out the study themes and interrelationships of the various themes. Curve lines and circles represent these interrelationships

between themes. Greater relationship strength is indicated by a thicker line and verse visa. The more significant an item is the bigger its circles.

3. RESULTS AND DISCUSSION

a. Growth Trend Analysis

Table 1. shows exponential growth over the last five years from 2018 to 2022. The fast growth over this period is attributed to the increased demand for eco-friendlier and customized dental treatment. Very slow growth was observed from 2008 to 2016. Research growth on this subject peaked up in 2017 and has been on the increase yearly.

Table 1. The growth trend of publications and citations on additive manufacturing in dentistry

Year	Number of publications
2022	48
2021	32
2020	28
2019	26
2018	21
2017	12
2016	7
2015	2
2014	3
2013	3
2012	1
2011	2
2010	1
2009	1
2008	1
Total	188

b. Journal Source Analysis

Of the 188 working documents, 83 document sources published articles on additive manufacturing in dentistry. Out of these 83 document sources, only 6 met the threshold at the defect setting of a minimum of 5 documents per source and zero citations. For this reason, the minimum number of documents per source was reduced to 3. With this new setting, 14 sources met the threshold. The analysis shows that the journal of prosthetic dentistry had the highest number of publications and was closely followed by the journal of prosthodontics. The top 14 most published journal sources are presented in Table 2. A similar trend was reported by (Kamali et al., 2022).

Table 2: Top Active journals publishing on additive manufacturing in dentistry

Source	Documents	Citations
Journal of prosthetic dentistry	8	310
Journal of prosthodontics	7	144
Dental materials	6	1049
Materials today: proceedings	6	49
International journal of computerized dentistry	5	101
Rapid prototyping journal	5	29
Journal of aesthetic and restorative dentistry	4	91

Journal of the mechanical behavior of biomedical materials	4	41
Lecture notes in mechanical engineering	4	3
Processes	4	35
Archives of materials science and engineering	3	15
Clinical epidemiology and global health	3	155
Metals	3	9
Polymers	3	23

3.3 Keyword Analysis

In scientometric studies, keywords are used to identify trends in a particular field or application (Adekunle et al., 2021; D. Aghimien et al., 2022; D. O. Aghimien et al., 2020; Nyika et al., 2021). In this study, the co-occurrence of keywords on the search query and their interrelationship has been analyzed by VOSviewer software and presented in Fig. 1. Of the retrieved 1348 keywords, 78 keywords met the set threshold of a minimum of 5 occurrences per keyword. Keywords such as 3D printing, computer-aided design, additive manufacturing, prosthesis design, digital dentistry, rapid prototyping, and dental implant. The co-occurrence map of keywords identified four clusters represented by the red, green, blue and yellow colours. The red cluster reflected keywords describing the industrial research focus of additive manufacturing, including the type of materials, mechanical properties, biocompatibility and material characterization techniques. The green cluster had keywords related to design and procedures for product optimization through computer-aided design and case documentation. While the blue clustered keywords focused on the additive manufacturing procedures for digital dentistry. The yellow-clustered words described the use of additive manufacturing in orthodontics, prosthesis and rapid prototyping of dentures.

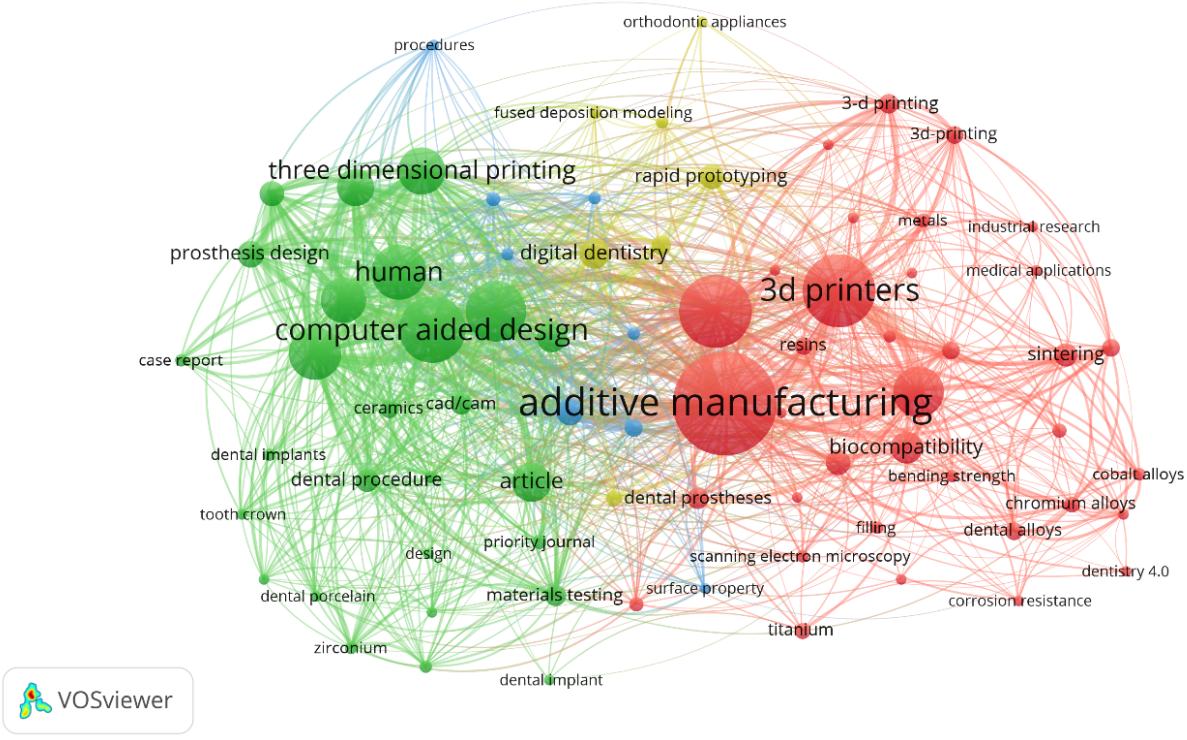

4. *Figure 1. Co-occurrence of keywords on additive manufacturing in modern dentistry*

3.4 Countries Analysis

For the bibliometric analysis of countries, the precondition was set at a minimum number of 5 documents per country and 2 citations. The database retrieved 55 countries actively publishing within the search query. From preconditions, 14 out of 55 countries meet the threshold. Table 3 shows that the United States of America (USA), India, Germany, Spain and Switzerland are the top publishers on additive manufacturing in dentistry, followed by Poland, Australia, China etc. Developed nations in Europe and the USA as well as fast-developing countries such as China, India, Brazil and Romania made up the list.

Table 3. Countries analysis

Country	Documents	Citations
United States	32	1489
India	23	265
Germany	11	81
Spain	10	134
Switzerland	9	133
Poland	8	67
Australia	7	55
China	7	42
United Kingdom	7	51
Romania	6	10
Slovenia	6	14
Sweden	5	105
Brazil	4	29
Slovakia	4	15

These nations now have the technical and human resources necessary to switch from traditional production methods to additive methods, in contrast to poor underdeveloped countries. (Nyika et al., 2021) reported a similar trend in a scientometric analysis on the environmental effects of additive manufacturing, where institutions of developed countries were active publishers on the subject. The bibliographic coupling of countries presented in Fig 2 reveals a strong interrelationship and collaboration between the United States, Switzerland and Spain. It also shows a robust partnership between USA and India. Strong partnerships also exist between Switzerland and Brazil. It is, therefore, safe to say that collaborative efforts contributed significantly to the advances in research studies in these countries. Sadly no African country was identified to be carrying out significant research in dentistry as it relates to additive manufacturing.

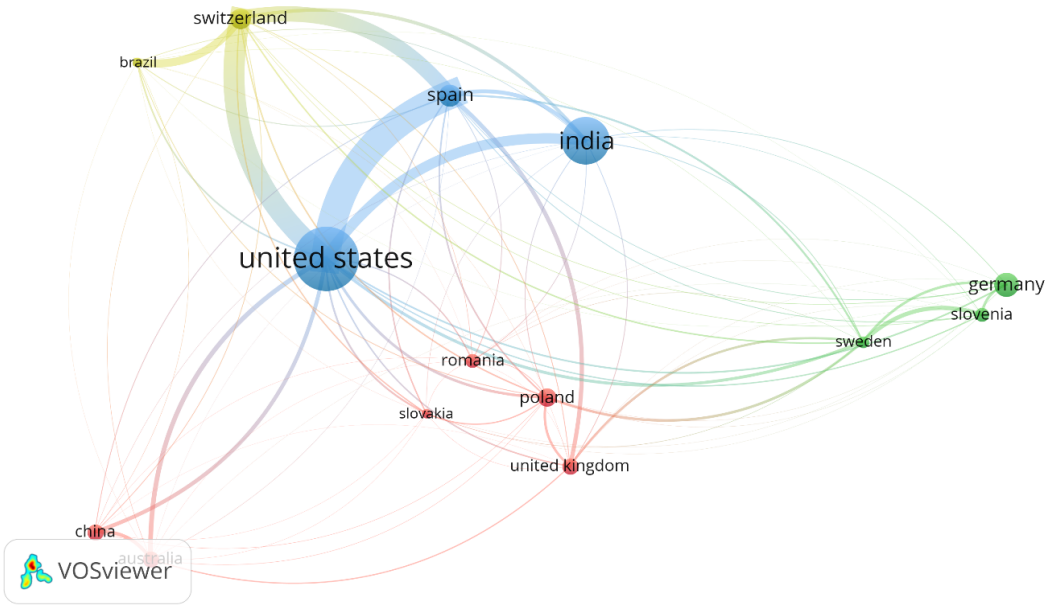

Figure 2. The bibliographic coupling of countries

4. FUTURE PROSPECT OF ADDITIVE MANUFACTURING IN MODERN DENTISTRY

Customized medication delivery systems for individuals with dental disorders may be made using 3D printing in addition to dental prosthesis and orthodontic. Additionally, 3D printing could make dental research and development more productive and efficient. In order to more accurately evaluate novel therapies and technologies, researchers may be able to employ 3D printing technology to produce more precise replicas of teeth, gums, and other oral components. Additive manufacturing produces dental prosthesis with minimum waste since it only employs the precise quantity of material required to construct the desired piece. This decreases the amount of material waste generated throughout the production process. Another long-term advantage of AM in dentistry is the reduction in the requirement for inventory storage and transportation. Additive manufacturing can be more energy-efficient than traditional manufacturing procedures since it requires less energy to manufacture the same or better-quality dental prosthesis. Finally, dental prostheses made with additive manufacturing technology can have a longer lifespan than traditional dental prostheses, minimizing the need for frequent replacements and the environmental effect of dental waste.

5. CONCLUSION

The application of additive manufacturing in dentistry, especially in the production of dentures, helps to improve patent treatment through custom-made dentures. It is imperative to explore the extent of the adoption of additive manufacturing in denture manufacturing. The study shows that the journal of prosthetic dentistry and journal of prosthodontics had the highest publication and that USA and India are the most active publishing countries in the subject area. This bibliometric analysis has revealed a rising trend in research, publications, and citations on additive manufacturing in dentistry, with a significant upshot from 2017 upwards. However, the technological capacity and uses of 3d printers must be extended to many nations by providing the personnel and financial resources required to implement the technology. In addition, more collaboration between authors and institutions is required in the field to share ideas and advance technological knowledge in dentistry. Indeed, an automatic procedure for dental manufacturing is the way forward, especially in South Africa, where a report has it that dental issues among 6-year-old children seem to be increasing, and it's currently around 40%. Of this, almost 80% of cases are untreated, and many of these children require restorations and possibly extractions (Wyk et al., 2004). Dulimi et al. (Srinivasan et al., 2021) relate that 3D printing and rapid prototyping can greatly change people's lives if implemented on a wider scale (Al-Dulimi et al., 2021). The study indicated that intensive research is needed on additive manufacturing of dentures considering the rising pollution of patients needing tooth replacement.

ACKNOWLEDGEMENT

Authors are grateful to University of Johannesburg for funding this research

REFERENCES

Adekunle, S. A., Ejohwomu, O., & Aigbavboa, C. O. (2021). Building information modelling diffusion research in developing countries: A user meta-model approach. *Buildings*, *11*(7), 1–20. https://doi.org/10.3390/buildings11070264

Aghimien, D., Aigbavboa, C. O., Oke, A. E., Edwards, D., Thwala, W. D., & Roberts, C. J. (2022). Dynamic capabilities for digitalisation in the AECO sector – a scientometric review. *Engineering, Construction and Architectural Management*, *29*(4), 1585–1608. https://doi.org/10.1108/ECAM-12-2020-1012

Aghimien, D. O., Aigbavboa, C. O., Oke, A. E., & Thwala, W. D. (2020). Mapping out research focus for robotics and automation research in construction-related studies: A bibliometric approach. *Journal of Engineering, Design and Technology*, *18*(5), 1063–1079. https://doi.org/10.1108/JEDT-09-2019-0237

Akl, M. A., & Stendahl, C. G. (2022). Removable Partial Denture Frameworks in the Age of Digital Dentistry : A Review of the Literature. *Prosthesis*, *4*, 184–201.

Al-Dulimi, Z., Wallis, M., Tan, D. K., Maniruzzaman, M., & Nokhodchi, A. (2021). 3D printing technology as innovative solutions for biomedical applications. *Drug Discovery Today*, *26*(2), 360–383. https://doi.org/10.1016/j.drudis.2020.11.013

Anadioti, E., Musharbash, L., Blatz, M. B., Papavasiliou, G., & Kamposiora, P. (2020). 3D printed complete removable dental prostheses: a narrative review. *BMC Oral Health*, *20*(1), 1–9. https://doi.org/10.1186/s12903-020-01328-8

Arutyunov, S., Kirakosyan, L., Dubova, L., Kharakh, Y., Malginov, N., Akhmedov, G., & Tsarev, V. (2022). Microbial Adhesion to Dental Polymers for Conventional, Computer-Aided Subtractive and Additive Manufacturing: A Comparative In Vitro Study. *Journal of Functional Biomaterials*, *13*(2), 1–12. https://doi.org/10.3390/jfb13020042

Awasthi, A., Saxena, K. K., & Dwivedi, R. K. (2021). An investigation on classification and characterization of bio materials and additive manufacturing techniques for bioimplants. *Materials Today: Proceedings*, *44*, 2061–2068. https://doi.org/10.1016/j.matpr.2020.12.176

Campbell, R. I., Beer, D. J. de, & Pei, E. (2019). Additive manufacturing in South Africa : building on the foundations. *Figshare*, 1–18.

Čretnik, A., & Fekonja, A. (2022). The Use of Selective Laser Melting in Mandibular Retrognathia Correction. *Metals*, *12*, 1–10. https://doi.org/10.3390/met12091544

Dizon, J. R. C., H, A., Jr, E., Chen, Q., & Advincula, R. C. (2018). Mechanical characterization of 3D-printed polymers. *Additive Manufacturing*, *20*, 44–67.

Ferchow, J., Bühler, M., Schlüssel, M., Zumofen, L., Klahn, C., Hofmann, U., Kirchheim, A., & Meboldt, M. (2022). Design and validation of a sheet metal clamping system for additive manufacturing and post-processing. *International Journal of Advanced Manufacturing Technology*, *119*(11–12), 7947–7967. https://doi.org/10.1007/s00170-022-08773-5

Galante, R., Figueiredo-Pina, C. G., & Serro, A. P. (2019). Additive manufacturing of ceramics for dental applications: A review. *Dental Materials*, *35*(6), 825–846. https://doi.org/10.1016/j.dental.2019.02.026

Goodacre, C. J., Garbacea, A., Naylor, W. P., Daher, T., Marchack, C. B., & Lowry, J. (2012). CAD/CAM fabricated complete dentures: concepts and clinical methods of obtaining required morphological data. *The Journal of Prosthetic Dentistry*, *107*(1), 34–46.

Güth, J. F., Runkel, C., Beuer, F., Stimmelmayr, M., Edelhoff, D., & Keul, C. (2017). Accuracy of five intraoral scanners compared to indirect digitalization. *Clinical Oral Investigations*, *21*(5), 1445–1455. https://doi.org/10.1007/s00784-016-1902-4

Hagman, C., & Svanborg, P. (2022). Additive Manufacturing of a Removable Partial Prosthesis in Titanium Using Binder Jetting Technology : A Brief Research Report. *Frontiers in Manufacturing Technology*, *2*(l), 1–7. https://doi.org/10.3389/fmtec.2022.863593

Hoang, D., Perrault, D., Stevanovic, M., & Ghiassi, A. (2016). Today surgical applications of three-dimensional printing: A review of the current literature & how to get started. *Annals of Translational Medicine*, *4*(23). https://doi.org/10.21037/atm.2016.12.18

Kalberer, N., Mehl, A., Schimmel, M., Müller, F., & Srinivasan, M. (2019). CAD-CAM milled versus rapidly prototyped (3D-printed) complete dentures: An in vitro evaluation of trueness. *Journal of Prosthetic Dentistry*, *121*(4), 637–643. https://doi.org/10.1016/j.prosdent.2018.09.001

Kamali, A. H., Moradi, M., Goodarzian, F., & Ghasemi, P. (2022). A discrete event simulation method for performance analysis of an additive manufacturing in the dental clinic. *International Journal of Advanced Manufacturing Technology*, *118*, 2949–2979. https://doi.org/10.1007/s00170-021-08135-7

Li, C., Pisignano, D., Zhao, Y., & Xue, J. (2020). Advances in Medical Applications of Additive Manufacturing. *Engineering*, *6*(11), 1222–1231. https://doi.org/10.1016/j.eng.2020.02.018

Nyika, J., Mwema, F. M., Mahamood, R. M., Akinlabi, E. T., & Jen, T. (2021). A five-year scientometric analysis of the environmental effects of 3D printing. *Advances in Materials and Processing Technologies*, *DOI: 10.10*, 1–11. https://doi.org/10.1080/2374068X.2021.1945267

Osman, R. B., Van Der Veen, A. J., Huiberts, D., & Wismeijer, D. (2017). 3D-printing zirconia implants; a dream or a reality? An in-vitro study evaluating the dimensional accuracy, surface topography and mechanical properties of printed zirconia implant and discs. *Journal of the Mechanical Behavior of Biomedical Materials*, *75*, 521–528.

Pradhan, S. R., Singh, R., & Banwait, S. S. (2022). On 3D printing of dental crowns with direct metal laser sintering for canine. *Journal of Mechanical Science and Technology*, *36*(8), 4197–4203. https://doi.org/10.1007/s12206-022-0737-y

Punia, U., Kaushik, A., Garg, R. K., Chhabra, D., & Sharma, A. (2022). 3D printable biomaterials for dental restoration: A systematic review. *Materials Today: Proceedings*, *63*, 566–572. https://doi.org/10.1016/j.matpr.2022.04.018

Rekow, E. D. (2020). Digital dentistry: The new state of the art — Is it disruptive or destructive? *Dental Materials*, *36*, 9–24. https://doi.org/10.1016/j.dental.2019.08.103

Rouf, S., Malik, A., Singh, N., Raina, A., Naveed, N., Siddiqui, M. I. H., & Haq, M. I. U. (2022). Additive manufacturing technologies: Industrial and medical applications. *Sustainable Operations and Computers*, *3*(May), 258–274. https://doi.org/10.1016/j.susoc.2022.05.001

Rouf, S., Raina, A., Irfan Ul Haq, M., Naveed, N., Jeganmohan, S., & Farzana Kichloo, A. (2022). 3D printed parts and mechanical properties: Influencing parameters, sustainability aspects, global market scenario, challenges and applications. *Advanced Industrial and Engineering Polymer Research*, *5*(3), 143–158. https://doi.org/10.1016/j.aiepr.2022.02.001

Sheoran, A. J., Kumar, H., Arora, P. K., & Moona, G. (2020). Bio-medical applications of additive manufacturing: A review. *Procedia Manufacturing*, *51*, 663–670. https://doi.org/10.1016/j.promfg.2020.10.093

Silva, M., Felismina, R., Mateus, A., Parreira, P., & Malça, C. (2017). Application of a Hybrid Additive Manufacturing Methodology to Produce a Metal/Polymer Customized Dental Implant. *Procedia Manufacturing*, *12*, 150–155. https://doi.org/10.1016/j.promfg.2017.08.019

Singh, S., & Ramakrishna, S. (2017). Biomedical applications of additive manufacturing: Present and future. *Current Opinion in Biomedical Engineering*, *2*, 105–115. https://doi.org/10.1016/j.cobme.2017.05.006

Srinivasan, M., Kamnoedboon, P., McKenna, G., Angst, L., Schimmel, M., Özcan, M., & Müller, F. (2021). CAD-CAM removable complete dentures: A systematic review and meta-analysis of trueness of fit, biocompatibility,

mechanical properties, surface characteristics, color stability, time-cost analysis, clinical and patient-reported outcomes. *Journal of Dentistry*, *113*(August). https://doi.org/10.1016/j.jdent.2021.103777

Stanley, M., Paz, A. G., Miguel, I., & Coachman, C. (2018). Fully digital workflow, integrating dental scan, smile design and CAD-CAM: Case report. *BMC Oral Health*, *18*(1), 4–11. https://doi.org/10.1186/s12903-018-0597-0

Su, C. Y., Wang, J. C., Chen, D. S., Chuang, C. C., & Lin, C. K. (2020). Additive manufacturing of dental prosthesis using pristine and recycled zirconia solvent-based slurry stereolithography. *Ceramics International*, *46*(18), 28701–28709. https://doi.org/10.1016/j.ceramint.2020.08.030

T, M., Y, H., J, K., Kuriyama S, T., & Y, T. (2009). A review of dental CAD/ CAM: current status and future perspectives from 20 years of experience. *Dental Materials Journal*, *28*(1), 44–56.

Tamburrino, F., Aruanno, B., Razionale, A. V., Barone, S., Martini, M., & Bordegoni, M. (2022). A Digital Process for Manufacturing Customized Trays for Dental-Whitening Treatments. *Processes*, *10*(7), 1–11. https://doi.org/10.3390/pr10071232

Tamimi, F., & Hirayama, H. (2019). *Digital Restorative Dentistry*.

Tian, Y., Chen, C., Xu, X., Wang, J., Hou, X., Li, K., Lu, X., Shi, H., Lee, E., & Jiang, H. B. (2021). A Review of 3D Printing in Dentistry : Technologies , Affecting Factors , and Applications. *Scanning*, *2021*, 1–19.

Tiwari, R., Bhayat, A., & Chikte, U. (2021). Forecasting for the need of dentists and specialists in South Africa until 2030. *Plos One*, *16*(5), 1–14.

Wyk, P. J. Van, Wyk, C. Van, & Africa, S. (2004). Oral health in South Africa. *International Dental Journal*, *54*, 373–377.

PAPER 193: LEARNING FROM EXAMPLES PARADIGM FOR THE DESIGN OF FUZZY CONTROL FOR A REACTIVE DISTILLATION PROCESS

*Giwa, Samuel Boluwatife[1]; Araromi, Dauda Olurotimi[1], Sulayman, Aminah Abolore[1] and Salami, Kolapo Kazeem[1]

[1]Department of Chemical Engineering, Ladoke Akintola University of Technology, Ogbomosho, Oyo State.

*Email: sbgiwa@student.lautech.edu.ng

ABSTRACT

The successful implementation of process intensification techniques, such as reactive distillation (RD), often requires tight control of the process. Tight control refers to the need to closely monitor and regulate process parameters such as temperature, pressure, flow rate, and reactant concentrations, among others, to maintain optimal performance. However, RD is highly nonlinear due to complex interactions between vapor-liquid equilibrium, vapor-liquid mass transfer, and chemical kinetics arising from the concurrent separation and reaction and hence making its control challenging. In this work, a generic nonlinear two-reactant-two product reactive distillation process model was used to design a fuzzy controller based on the 'learning from examples' paradigm for RD closed loop system. The performance of the fuzzy controller was compared with Proportional Integral (PI) controller. The results showed that the fuzzy controller outperformed the PI controller in terms of setpoint tracking with no overshoot

KEYWORDS: process intensification, Reactive Distillation, Nonlinear, Fuzzy controller, Proportional integral control

6. INTRODUCTION

In the process industry, chemical reactions can achieve the purpose of transforming raw materials into products. Some of these reactions include transesterification reaction employed in the production of isopropanol (Geng et al., 2022), co-production of ethyl acetate (EtAC) and amyl acetate (AmAC), production of ethanol(Zhao et al., 2021). The products obtained may be subjected to additional purification/separation for specific purposes, particularly when applications demand exceptionally high levels of purity. For instance, ethanol intended for use as a combustion fuel generally needs to achieve a purity level, as the presence of water could potentially lead to the deterioration or corrosion of engine components (Khuong et al., 2017). In separation of this water from ethanol, Reactive distillation emerges as a highly viable alternative to traditional distillation in the separation of water from ethanol(Cárdenas-Guerra et al., 2018). This is because water and ethanol form an azeotrope at 95% composition, thus presenting a challenge that conventional distillation struggles to overcome (Mekala et al., 2022).

Reactive distillation is a process which combines chemical reaction and distillation in a single column(Sakuth et al., 2008)(Leet & Kulprathipanja, 2019). Reactive distillation has been employed in many industrial processes (Luyben, 2009). In the face of global warming, reactive distillation has been shown to offer a low CO2 emission as synthesis of ethyl propionate (Du et al., 2022). The integration of reaction and separation have effects of reducing the operating cost, as it could be seen in the purification of levulinic acid where equipment cost is saved by 24%(Solis-Sanchez et al., 2022). The growing application of reactive distillation processes has necessitated a better understanding of its process dynamics and control. The integration of separation and reaction presents a very complex control strategy, this is a result of the nonlinear coupling of chemical reaction, and phase equilibrium as the design of reactive distillation processes is significantly more complex than the design of conventional distillation processes (Keller, 2014). This makes the control of RD systems challenging as the process objectives such as obtaining product purity specification (separation performance) while maximizing reactant conversion (reaction performance) must be fulfilled. These are translated into achievable control objectives, which are then integrated into the overall control strategy (Baur et al., 2000).

Reactive distillation columns are generally modelled by a set of highly nonlinear first-order differential equations (Olanrewaju & Al-Arfaj, 2005). However, many model-based controllers use linear models because they are easier to analyse and require fewer computational recourses than nonlinear models (Kawathekar, 2021) but the highly non-linear nature of RD makes linear controllers difficult in capturing and controlling its complex dynamics (Fedor & Perduková, 2017). Moreover, for effective control, nonlinear controllers show high superiority over linear controllers(Kawathekar & Riggs, 2007). This introduces us to a special type of controller called the fuzzy logic controller which can combat this problem of non-linearities as it is not based on a mathematical model and is mostly used to solve the problem with a high degree of uncertainty or fuzziness. This type of controller is based on fuzzy logic and it behaves like a man-in-the-loop(Al-Odienat & Al-Lawama, 2008).

In a study conducted by Tian et al. (2003), the reliability of the fuzzy logic controller was demonstrated through the successful implementation of a pattern-based predictive control scheme that was developed to maintain the required purity in the distillation ethyl tert-butyl ether (Tian et al., 2003). Kapoor et al. (2011) conducted a study to compare the performance of a PID and fuzzy controller in a reactive distillation column using a generic mathematical model and found that the deviation of temperature from steady state error was less with the use of the fuzzy controller and it also reached a steady state faster.

7. THEORETICAL ANALYSIS AND METHODOLOGY

2.1 Modelling Reactive Distillation Process

In this study, the reactive distillation process was modelled using the principles of mass and energy balance based on the assumptions presented by Bamikole & Taiwo(2018). Figure 1 shows a schematic diagram of a typical reactive distillation column with the column considered to have N number of stages with the reboiler and the condenser being the 1 and N stages respectively.

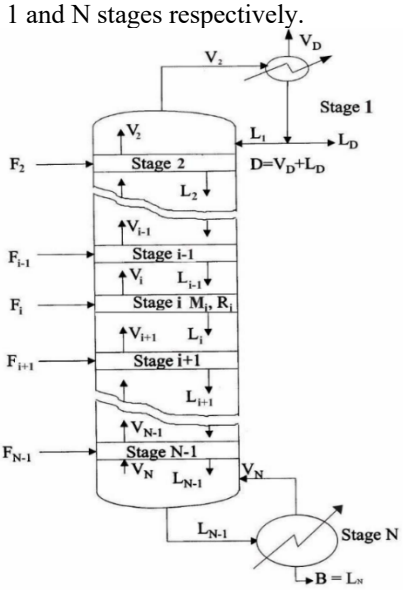

Figure 3: A schematic diagram of reactive distillation (Bamikole & Taiwo, 2018)

The reactive distillation column is comprised of three main sections. The first section called the reactive section, is where the chemical reaction occurs. The second section called the stripping section, is located between the condenser and the reactive section. The third section called the rectifying section, is located between the reactive section and the reboiler.

Equation 1 to 9 shows various equations modelling the column with the various parameters defined in section 2.2

Material balance around the reboiler:

$$\frac{M_N\, dx_N}{dt} = L_{N-1}x_{N,j} - Bx_{N,j} - v_{v_1}y_{N,j} \text{ where } L_{N-1} = B + V_N \quad (1)$$

j is the number of components

$$\frac{M_i\, dx_{1,j}}{dt} = L_{i-1}x_{i-1,j} - L_i x_{i,j} + V_{i+1}y_{i+1,j} - V_i y_{i,j} - F_i z_{1,j} + \delta_i v_j r_{i,j} \quad (2)$$

$$V_i = D(r+1) + \sum_{i=2}^{i}(1-q_i)F_i \quad (3)$$

Material balance around the condenser:

$$\frac{M_1\, dx_{1,j}}{dt} = V_2 y_{2,j} - L_i x_{I,j} - Dx_{i,j} \quad \text{where } V_2 = L_1 + D \quad (4)$$

Material balance in the liquid phase:

$$L_i = \sum_2^i q_i F_i + \sum_1^i R_i + rD \quad (5)$$

The equation showing the vapor flowrate from other stages:

$$V_i = D(r+1) + \sum_{i=2}^{i}(1-q_i)F_i \quad (6)$$

The reaction rate equation is given as

$$R_{i,j} = r_{i,j} * M_i \qquad where\ r_{i,j} = 3.255 * 10^{12} e^{-\frac{9547}{T_i}} x_A x_B \quad (7)$$

Equations 8 and 9 are derivation from the vapor-liquid equilibrium and Raoults law

$$\sum_{j=1}^{nc} y_{i,j} = \sum_{j=1}^{nc} \frac{\gamma_{i,j} P_{i,j}^0 x_{i,j}}{\emptyset_{i,j} P} = 1 \text{ where } \sum_{j=1}^{nc} x_{i,j} = 1 \quad (8)$$

$$T_i = \frac{1}{ln\left(P_{i,j}^0\right)}\left(A_j - B_j ln\left(P_{i,j}^0\right)\right) \quad (9)$$

The resulting equations above were solved using the semi-implicit Runge-Kutta in MATLAB workspace using relevant parameters presented by Olanrewaju & Al-Arfaj(2005).

a. Parameters nomenclature

In this section, all the parameters and variables utilized in equations 1 through 9 are explicitly defined.
B is the bottom flow rate, V_N is the Vapor flow rate coming from stage N, L_N is the Liquid flow rate coming from stage N
D is the distillate flow rate, $x_{i,j}, y_{i,j}$ is the Liquid and vapor mol fraction of the ith component at the ith stage respectively.
q_i is the Vapor quality (the fraction or percentage of vapor in a two-phase mixture of a liquid and a vapor) at the ith stage, $r_{i,j}$ is the Rate of production of the jth component in the ith stage, F_i is the Feed flow rate at the ith stage.
M_i is the Liquid hold-up at the ith stage, R is the Reflux ratio, δ_i Checks if the reaction is taking place at the ith stage where it takes a value of 1 if the reaction occurs else 0, k_0 is the Arrhenius constant, and E is the activation energy.
R is the universal gas constant, $R_{i,j}$ is the Rate of production of jth component in the ith stage, and N is the total number of stages including the reboiler and the reflux drum.
x_A is the mol fraction of water in the liquid phase, x_B is the mole fraction of ethylene oxide in the liquid phase, nc is the Number of components,
A_j, B_j is the Antoinne Parameters, $P_{i,j}^0$ is the Saturated vapor pressure of the jth component in the ith stage, $\emptyset_{i,j}$ is the Fugacity coefficient of the jth component at the ith stage.
T_i is the Temperature at the ith stage, $\gamma_{i,j}$ is the Activity coefficient of the jth component in the ith stage, $P_{i,j}^0$ is the saturated vapor pressure of the jth component in the ith stage, Vs is the Vapor flow rate from the reboiler.

b. Fuzzy controller

According to Nizami (2011), the use of a fuzzy logic system is a key feature of the fuzzy controller, which gained widespread attention when Mamdani designed a control system for a laboratory-scale steam engine boiler using fuzzy algorithms (Mamdani, 1974). Fuzzy control provides a formal framework for representing, manipulating, and implementing a human's heuristic knowledge of system control (Ibarra & Webb, 2016) as it is based on the concept of fuzzy logic, which allows for degrees of truth between true and false. The use of fuzzy control provides a flexible and adaptive approach to system control, accounting for uncertainty and complexity (Zadeh, 2009). Additionally, incorporating human expertise into the control system leads to improved system performance and efficiency (Heras-Cervantes et al., 2019). The fuzzy controller is integrated into a closed-loop control system, as shown in the block diagram in Figure 2.

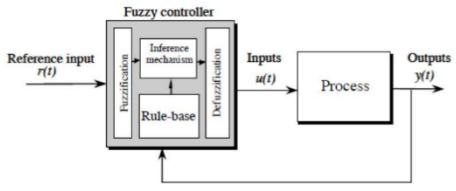

Figure 2: A typical fuzzy controller

The fuzzy controller has inputs (r(t)) and outputs (u(t)), similar to a regular PID controller. The plant outputs are represented by y(t) (Matko & Kavšek-Biasizzo, 2000). The design of a fuzzy controller involves selecting inputs and outputs, filtering them, and designing each of the four components of the controller as shown in Figure 2.

c. Construction of fuzzy rules from the "Learning from examples" algorithm

In their 1992 article, Wang and Mendel introduced the learning-from-examples approach, which involves that involves constructing a fuzzy rule-based system from a set of example cases. This method allows for the creation of a fuzzy inference system without the need for prior knowledge of the system's underlying dynamics or structure (Wang & Mendel, 1992). The learning from examples algorithm is described by the following key steps

1. Defining the lower and upper bound of output and input
2. Input Data: Start with a labeled dataset called "examples" where each data point consists of input features and corresponding output labels.
3. Setting up fuzzy membership function for set of input and output
4. Construction of rules using training data
5. Check if similar rule exists; if no, go to step 8 else move to step 6
6. Compare the degree of attainment
7. Select rule with the highest degree of attainment and discard the other rule
8. Add to rules

Our objective is to achieve servo responses in the RD system's top and bottom product compositions by controlling the reflux flow rate and vapor boil-up rate, using proportional integral control (PI) triggered by the error signal as shown in equation (10)

$$u(t) = k_p * e(t) + k_i * \int e(t)dt \tag{10}$$

k_p and $k_i$are the proportional constant and integral constant respectively, e is the magnitude of the error signal at time t and u is the output signal from the controller.

Simulation of the closed-loop of the RD model under PI control and Tyreus-Luyben parameter settings generated a dataset for fuzzy rule construction. Fuzzy membership functions assigned to regions in the input and output domains represented linguistic values, with triangular membership functions used. The dataset was used to obtain fuzzy rules, with premises formed from the input portion and consequents from the output portion. The rule base for the two-input two-output system has the form described in Equation 11(Passino & Yurkovich, 1998).

$$R_i = if\ u_1 is\ X_1^j\ and\ u_2 is\ X_2^k\ Then\ y\ is\ Y^l \tag{11}$$

The ith rule has "degree" defined by equation (12) for output y

$$degree\left(R_i^y\right) = \mu_{A_1^j}(u_1) * \mu_{A_1^k}(u_2) * \ldots * \mu_{A_n^l}(u_n) * \mu_{B_1^p}(y) \tag{12}$$

where, $u_1 and\ u_2$ denote reflux rate and vapor boil-up rate, respectively, y denote either top and bottom product composition, j, k, l, and q can be any of linguistic values (S, C, B), $X_m^j and\ Y_m^j$ denote the fuzzy sets with associated membership functions $\mu_{X_k^j}(u_k)$ and $\mu_{Y_m^j}(y_m), m = 1,2$

Through rules embedded in the inference mechanism, the appropriate rule was determined by computing $\mu_i(u_1, u_2, \ldots, u_n)$ for all rules in the rule base as described by Equation 13.

$$\mu_i(u_1, u_2, \ldots, u_n) = \mu_{A_1^j}(u_1) * \mu_{A_1^k}(u_2) * \ldots * \mu_{A_n^l}(u_n) \tag{13}$$

The largest value of $\mu_i(u_1, u_2, \ldots, u_n)$ fixes the appropriate rule.

d. Defuzzification Stage

This is the stage to convert the fuzzy set quantification of the conclusions to a discrete value that will serve as input to the plant(Matko & Kavšek-Biasizzo,2000). The defuzzification strategy used in this work is the centroid method given in Equation 14 (Nizami, 2011; Ibarra & Webb, 2016).

$$y_q^{crisp} = \frac{\sum_{i=1}^{R} b_i^q \mu_i(u_1,u_2,\ldots,u_n)}{\sum_{i=1}^{R} \mu_i(u_1,u_2,\ldots,u_n)} \quad (14)$$

where R is the number of rules and b_i^q is the center of the area of the membership function $\mu_{B_q^k}(y_q)$

8. RESULTS AND DISCUSSION

To simulate the system, the fourth order Runge-Kutta method was utilized with a sampling interval of 3 minutes. For the LFE algorithm, three membership functions were selected for each input and output, which represent three linguistic values. The fuzzy control employed four input linguistic variables; top error, integral of top error, bottom error, and integral of bottom error, where the error indicates the difference between each product composition and the desired value. Reflux rate and vapor boil-up rate were selected as output linguistic variables. The fuzzy rule base was generated using 2000 data sets, and the rule base was used to generate a surface plot for the bottom and top composition fuzzy controllers (Figures 4a and 4d) respectively.

The fuzzy controller's information is compactly represented by a surface created from rules and membership functions.

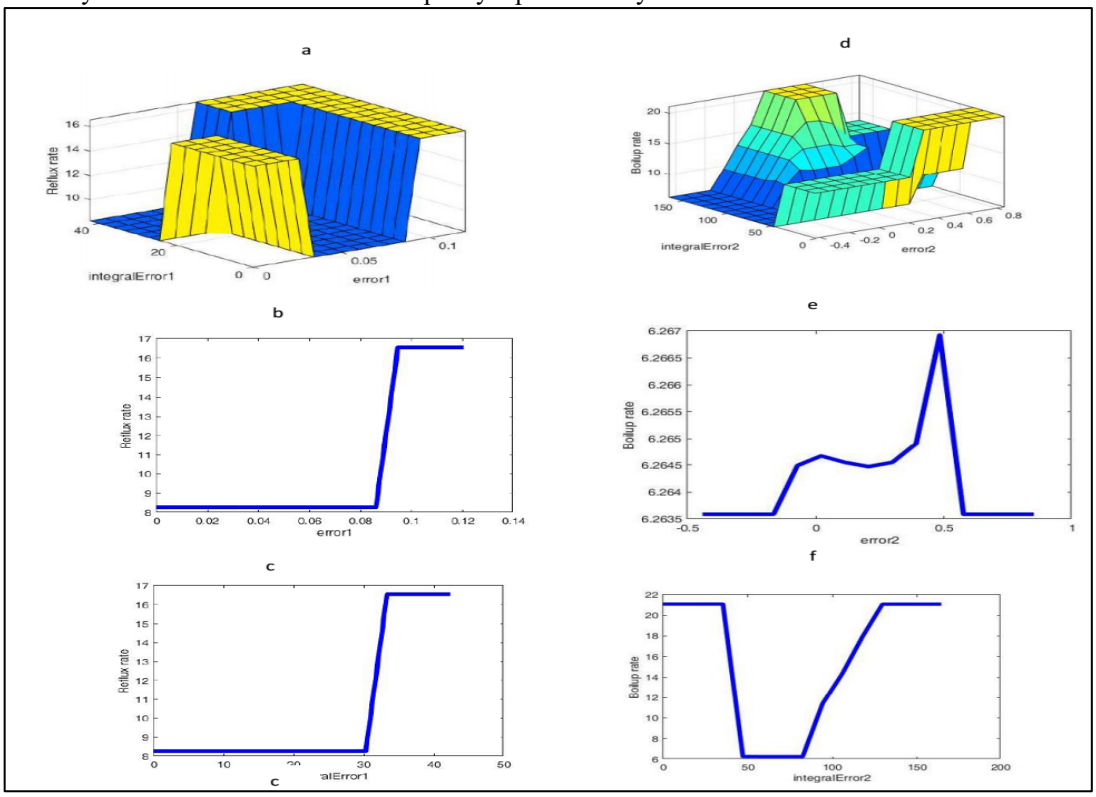

Figure 4: Surface plot for the control surface represented in both 3-D and 2-D

The top composition fuzzy controller exhibits a discontinuous control surface in the form of a plane. Figures 4b and 4c show quasi-linear relationships between the input and controller output. The control surface for the bottom composition is rippled and exhibits a non-linear relationship between the inputs and controller output.

The designed fuzzy controllers for top and bottom compositions are tested and the results are shown in Figure 5. The controllers can effectively control the RD system by tracking set points. The response is smooth and without oscillations.

In Figure 5, the performance of the fuzzy controller and PI controller based on Tyreus-Luyben settings in tracking set point variables is shown with continuous and dotted lines, respectively. Both controlled outputs and manipulated variables are displayed. Multiple simulations were conducted with incremental set point values up to 0.98, beyond which the system became unstable. The PI controllers exhibited oscillatory behaviour and unreasonable overshoot, while the Fuzzy controllers had smooth responses and were able to track all setpoints tested. Overall, the Fuzzy controllers outperformed the conventional PI controllers.

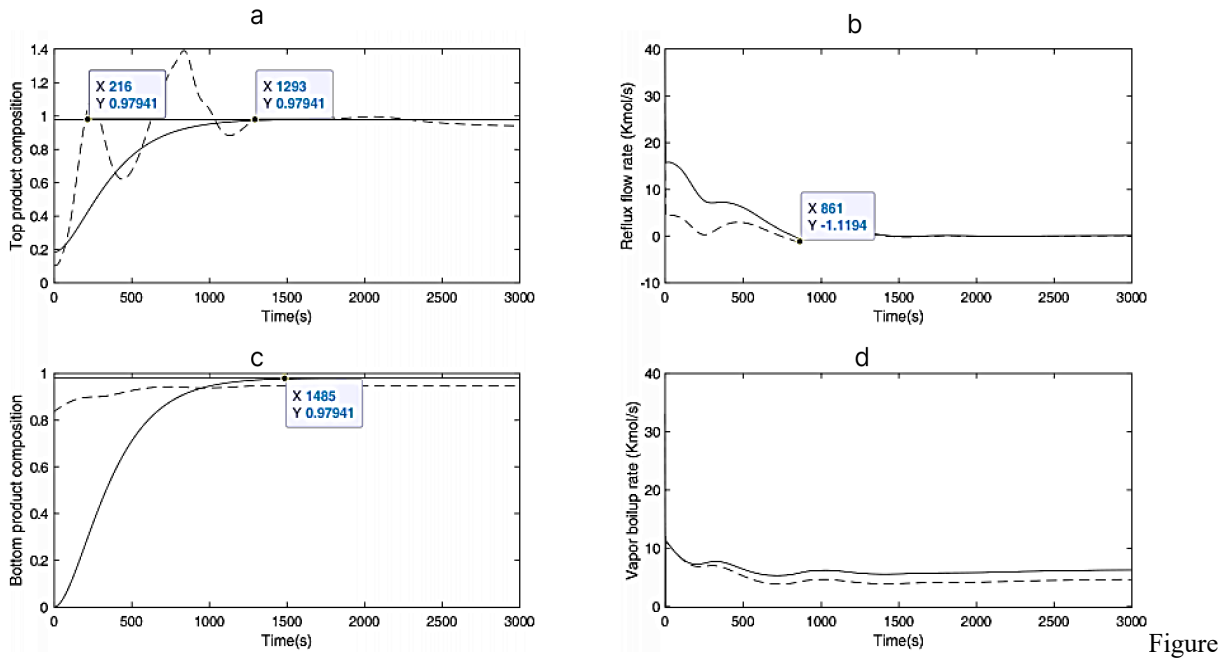

Figure 5: Closed-loop responses of RD process

The responses of the fuzzy controllers were slow and overdamped compared to conventional PI controllers. The rise time for the fuzzy controller's top product response is significantly longer, as seen in Figure 5a. However, the rise times for both PI controllers are unreasonably short for practical implementation of the cascade process plant, which has inherent transportation lag due to simultaneous reaction and separation. Therefore, the rise time obtained for the Fuzzy control system is reasonable in a practical sense.

The output of the controller for reflux and vapor boil-up rates are similar, as shown in Figures 5b and 5d. The Fuzzy controller initially sends a large feedback signal, while the PI controller exhibits unreasonable behaviour with negative values. Both controllers initially provide the same rate for vapor boil-up, but they later diverge, with the fuzzy controller having a higher rate. The findings suggest that high flow rates are necessary during start-up, followed by a steady supply at lower rates once steady states have been established for both products.

To ensure balance, the study focused on the reaction, which is a reversible elementary reaction involving four reacting species with unity stoichiometric coefficients. The components' relative volatilities are $\alpha_C > \alpha_A > \alpha_B > \alpha_D$, with A and C being the main components of the top product, while B and D are present in larger quantities in the bottom product. After simulations, both top and bottom products reached a purity of 0.98, leading to an overall conversion of 98% using the designed fuzzy controllers for the RD process.

Our approach surpassed the method utilized by Olanrewaju and Al-Arfaj(2005) which assumed a linear system and utilized a robust linear state estimator for the modelling and control of reactive distillation. By achieving higher product purities, our approach demonstrated its superiority and potential to enhance process performance. Our approach achieved higher product purities, demonstrating its effectiveness and potential for improving process performance. In 2.4 hours, a composition of 97.9% was reached for the x_d composition in the bottom product, while Olanrewaju and Al-Arfaj's method took 4 hours to reach a steady state composition of 95%. Similarly, for the top product, we achieved 97.9% purity was achieved in 2.8 hours, compared to Olanrewaju and Al-Arfaj's method which took 1.5 hours to reach 95%. Although our approach has a minor drawback in achieving a steady state for the x_c composition, its ability to achieve higher purities in a shorter time frame makes it a promising avenue for further development.

3. CONCLUSION

An uncoupled fuzzy rule-based controller for a generic nonlinear reactive distillation model was developed using a "Learning from Example" algorithm. This algorithm employed data obtained from simulated closed-loop control schemes of the RD, which utilized PI-type controllers with parameters obtained from Tyreus-Luyben parameter settings. Using three triangular membership functions for both the antecedent and consequent parts of the If-Then rules, sixteen rules were derived for each control scheme. The resulting fuzzy controller was able to track all the setpoints used in the simulations, achieving a purity of 98% for each output. Moreover, the overall fractional conversion for the RD was found to be 98%.

REFERENCES

Al-Odienat, A. I., & Al-Lawama, A. A. (2008). The advantages of PID fuzzy controllers over the conventional types. *American Journal of Applied Sciences*, *5*(6), 653–658. https://doi.org/10.3844/ajassp.2008.653.658.

Bamikole, J. O., & Taiwo, O. (2018). *Journal of the Nigerian Society of Chemical Engineers, 33 (1), 2018 Modelling And Simulation Of Reactive Distillation Systems Using Matlab And Aspen Plus*. *33*(1), 129–142.

Cárdenas-Guerra, J. C., Figueroa-Gerstenmaier, S., Reyes-Aguilera, J. A., & Hernández, S. (2018). Simulation Study of a Reactive Distillation Process for the Ethanol Production. Chemical Engineering Transactions, 69, 613–618. https://doi.org/10.3303/CET1869103

Fedor, P., & Perduková, D. (2017). Use of Fuzzy Logic for Design and Control of Nonlinear MIMO Systems. *Modern Fuzzy Control Systems and Its Applications*. https://doi.org/10.5772/68050.

Geng, X., Ding, Q., Na, J., Yan, P., Li, H., Lei, Z., Li, G., Dai, C., & Gao, X. (2022). Enhanced transesterification reactive distillation for producing isopropanol: From kinetics, pilot-scale experiments, and process design to sustainability evaluation. Separation and Purification Technology, 302, 122108. https://doi.org/10.1016/J.SEPPUR.2022.122108

Heras-Cervantes, M., Marx Chávez-Campos, G., Javier Vergara Hernández, H., del Carmen Téllez-Anguiano, A., Anzurez-Marin, J., & Espinosa-Juárez, E. (2019). Fuzzy Logic Modeling and Observers Applied to Estimate Compositions in Batch Distillation Columns. Distillation - Modelling, Simulation, and Optimization. https://doi.org/10.5772/intechopen.83479.

Ibarra, L., & Webb, C. (2016). Advantages of Fuzzy Control While Dealing with Complex/ Unknown Model Dynamics: A Quadcopter Example. *New Applications of Artificial Intelligence*. https://doi.org/10.5772/62530.

Kapoor, U., Rani, A., Singh, V., & Gupta, J. R. P. (2011). Simulation and control of reactive distillation column. *India International Conference on Power Electronics, IICPE 2010*. https://doi.org/10.1109/IICPE.2011.5728067

Kawathekar, R. (2021). Nonlinear Model Predictive Control. In *Advances in Industrial Control*. https://doi.org/10.1007/978-3-030-68010-7_5.

Kawathekar, R., & Riggs, J. B. (2007). *Nonlinear model predictive control of a reactive distillation column*. *15*, 231–239. https://doi.org/10.1016/j.conengprac.2006.07.004.

Keller, T. (2014). Reactive Distillation. In *Distillation: Equipment and Processes*. https://doi.org/10.1016/B978-0-12-386878-7.00008-5.

Khuong, L. S., Masjuki, H. H., Zulkifli, N. W. M., Mohamad, E. N., Kalam, M. A., Alabdulkarem, A., Arslan, A., Mosarof, M. H., Syahir, A. Z., & Jamshaid, M. (2017). Effect of gasoline–bioethanol blends on the properties and lubrication characteristics of commercial engine oil. RSC Advances, 7(25), 15005–15019. https://doi.org/10.1039/C7RA00357A

Leet, W. A., & Kulprathipanja, S. (2019). Reactive Separation Processes. Reactive Separation Processes, 1–17. https://doi.org/10.1201/9780203741238-1

Mekala, M., Neerudi, B., Are, P. R., Surakasi, R., Manikandan, G., Kakara, V. R., & Dhumal, A. A. (2022). Water Removal from an Ethanol-Water Mixture at Azeotropic Condition by Adsorption Technique. Adsorption Science and Technology, 2022. https://doi.org/10.1155/2022/8374471

Luyben, W. L. (2009). Control of a column/pervaporation process for separating the ethanol/water azeotrope. *Industrial and Engineering Chemistry Research*, *48*(7), 3484–3495. https://doi.org/10.1021/ie801428s.

Matko, D., & Kavšek-Biasizzo, K. (2000). Generalized Predictive Control of a Nonlinear Process using Fuzzy Model. *IFAC Proceedings Volumes*, *33*(25), 83–88. https://doi.org/10.1016/S1474-6670(17)39320-5

Mamdani, E. H. (1974). Application of fuzzy algorithms for control of simple dynamic plant. Proceedings of the Institution of Electrical Engineers, 121(12), 1585-1588.

Nizami, M. S. (2011). *Development of a Fuzzy Logic Controller for a Distillation Column Using Rockwell Software by Master of Applied Science*.

Olanrewaju, M. J., & Al-Arfaj, M. A. (2005). Development and application of linear process model in estimation and control of reactive distillation. *Computers and Chemical Engineering*, *30*(1), 147–157. https://doi.org/10.1016/j.compchemeng.2005.08.007

Passino, K. M., & Yurkovich, S. (1998). *Fuzzy control*. 475.

Sakuth, M., Reusch, D., & Janowsky, R. (2008). Reactive Distillation. Ullmann's Encyclopedia of Industrial Chemistry. https://doi.org/10.1002/14356007.C22_C01.PUB2

Tian, Y. C., Zhao, F., Bisowarno, B. H., & Tadé, M. O. (2003). Pattern-based predictive control for ETBE reactive distillation. *Journal of Process Control*, *13*(1), 57–67. https://doi.org/10.1016/S0959-1524(02)00011-2

Wang, L. X., & Mendel, J. M. (1992). Generating Fuzzy Rules by Learning from Examples. *IEEE Transactions on Systems, Man, and Cybernetics*, *22*(6), 1414–1427. https://doi.org/10.1109/21.199466

Zadeh, L. A. (2009). Position Paper: Toward extended fuzzy logic; A first step. Fuzzy Sets and Systems, 160(21), 3175-3181. Retrieved 5 9, 2023, from https://sciencedirect.com/science/article/pii/s0165011409002140

Zhao, F., Yi, Y., & Lü, X. (2021). Essential process and key barriers for converting plant biomass into biofuels. *Advances in 2nd Generation of Bioethanol Production*, 53–70. https://doi.org/10.1016/B978-0-12-818862-0.00009-1

PAPER 226 – STUDY OF THE PYROLYTIC CONVERSION OF PALM KERNEL SHELLS BIOMASS TO FUEL

O. R. Ayadju[1], I. Bori[2*]

[1]Department of Mechanical Engineering, Federal University of Technology, Minna, Nigeria.
[*]Email: chat2obus@yahoo.com

ABSTRACT
The overdependence on the use of fossil fuels, environmental problems caused by conventional energy sources and deforestation caused by the excessive use of wood for energy has brought the need for alternative energy sources. Agricultural residue such as palm kernel shells have shown great promise in solving this energy problem.
The biomass material used (palm kernel shell) was obtained from Suleja, Niger state. The palm kernel shell was washed and sun dried to reduce the level of moisture present in the feedstock. A pyrolyzer was designed, fabricated and was used for the pyrolysis of palm kernel shell. The process of pyrolysis was carried out at pyrolyzing temperature range of 300°C – 700°C and at a pyrolysis duration of 20 minutes.
The result showed that palm kernel shell at 300°C yielded 71.34% char, 20.69% tar and 7.92% gas; 400°C yielded 44.04% char, 26.12% tar and 18.1% gas; 500°C yielded 42.10% char, 37.29% tar and 20.61% gas; 600°C yield 33.71% char, 40.14% tar and 26.14% gas; 700°C yielded 29.88% char, 33.04% tar and 37.08% gas.
From the above result, it can be concluded that as the pyrolyzing temperature increases, both tar and gas increases rapidly while the char production reduces and vice-versa.

KEYWORDS: Biomass, energy, pyrolysis, tar, char, fabricated, design

1. INTRODUCTION

The surging worldwide clamour and the unfavourable effects of non-renewable fossil fuels on the environment had inspired substantial research attention in a wide range of engineering application of renewable resources such as biomass (Oyedepo et al., 2019). Its initial energy comes from the sun, and can regrow in a relatively short amount of time. Its sources are consistently available and can be managed sustainably. Hence the heightening energy demand must be progressively contended by varied energy resources, including sustainable and renewable sources like biomass (Ciubota-Rosie et al., 2008).

We use four types of biomass today- wood and agricultural products, solid waste, landfill gas and biogas, and alcohol fuels (like ethanol or biodiesel) (National Energy Education Development, 2008).

The main benefits of biomass are biomass is a renewable energy source, biomass helps climatic changes by reducing greenhouse gas emissions, cleaner environment and widely available source of energy.

The problems with biomass energy is that it takes a lot of land area and water to grow plants, and it can setup a potential food versus fuel feedstock as food crops like cassava, maize, sweet potato are used as biomass feedstocks and could increase deforestation due to the use of wood biomass, which can in turn affect the environment.

The major components of biomass are cellulose, hemicellulose and lignin, each of which is different in their decomposition behaviour (Vigouroux, 2001). Moreover, decomposition of each component depends on heating rate, temperature and the presence of contaminants due to different molecular structures (Jahirul et al., 2012).

Biomass can be converted into useful forms of energy using a number of different processes. Factors that influence the choice of conversion process are the type and quantity of biomass feedstock, the desired form of the energy, environmental standards, economic conditions, and project specific factors.

The methods of converting biomass to energy: Conversion of biomass to energy is undertaken using two main process technologies: The conversion of biomass to energy is undertaken using biochemical/biological method or thermochemical methods. The biochemical conversion is the process by which biomass is converted into gas

(CO_2/CH_4), waste (compost or fertilizer) and water (water or C_2H_5OH) by using microorganisms (Ciubota-Rosie et al., 2008).

Thermochemical methods

Solid fuels, such as biomass and coal, undergo thermal conversion to provide various forms of energy and other products. The three thermochemical processes by which solid fuels are converted are: Direct combustion, Gasification, Liquefaction, Torrefaction, and Pyrolysis (Mafu, 2018). Pyrolysis is defined as the thermal destruction of organic materials in the absence of oxygen, or partially combusted in a limited oxygen supply, to produce a hydrocarbon rich gas mixture, an oil-like liquid and a carbon rich solid residue. Pyrolysis converts biomass at temperatures around 5000 C, in the absence of oxygen, to liquid (bio-oil), gaseous and solid (charcoal) fractions (Ciubota-Rosie et al., 2008). The advantages of pyrolysis are but not limited to the production of few air emissions due to limited use of oxygen, carbon sequestration, high energy efficiency, versatility, and energy independence.

2. THEORETICAL ANALYSIS

2.1 Moisture content

2.1 Moisture content is the weight of water contain in the sample. It was determined by measuring the difference between the weights of the samples before and after the drying process, and it is mathematically determined with the relation:

$$\text{M.C.} = \frac{\text{Wo}-\text{WI}}{W1} \times 100 \qquad (2.1)$$

The same analysis is carried out on the sample three times and the average of the three results is calculated using the relation:

$$\text{M.C.}_T = \frac{\text{M.C.1}+\text{M.C.2}+\text{M.C.3}}{3} \qquad (2.2)$$

$MC_1 + MC_2 + MC_3$ are the moisture content of the first, second, and third trial of the moisture content determination.

2.2 Weight determination

Weight determination is very important in the analysis, because it gives the amount of products (char, tar, and gas) at different temperature. It also helps in determining the efficiency of the process and that of the equipment.

$$W_{pks} = w_{ppks} - w_p \qquad (2.3)$$

$$W_{char} = w_{pchar} - w_p \qquad (2.4)$$

Weight of measuring pan is denoted as w_p, and the weight of measuring pan together with the sample is denoted as w_{ppks}, weight of char produced is $W_{char} = w_{pchar} - w_p$

Weight of Tar produced

The condensate receiver containing the tar was weighed and the weight of the tar was determined by subtracting the weight of the condensate receiver from the weight obtained. If the weight of the condensate receiver is represented as W_{Crtar}, then the weight of the tar W_{tar} produced was determined using the relation:

$$W_{tar} = W_{Crtar} - W_{CR} \qquad (2.5)$$

The project work was based on the assumption that there was no loss or any leakage, therefore, since the weight of char and weight of char and weight of tar is gotten as given in the expression above. Then weight of gas can be determined according to the relation:

$$W_{pks} = W_{char} + W_{tar} + W_{gas} \quad (2.6)$$

$$W_{gas} = W_{pks} - (W_{char} + W_{tar}) \quad (2.7)$$

2.3 Product yield

Product yield is the ratio of the weight of product to the sample in percentage. It was determined for each product by weighing each product of the pyrolysis, and the sample.

Char yield

Having determined the weight of char, W_{char} and the weight of the sample W_{pks} according with the relations given above. Then char yield Y_{char} was determined according to relation:

Char yield, $Y_{char} = \frac{W_{char}}{W_{pks}} \times 100$ (2.8)

Tar yield, $Y_{char} = \frac{W_{tar}}{W_{pks}} \times 100$ (2.9)

Gas yield

Gas yield Y_{gas} was determined with the known weight of the gas, W_{gas}, and weight of the sample, $W_{pks.}$ And it is given in the relation as:

Gas yield, $Y_{gas} = \frac{W_{gas}}{W_{pks}} \times 100$ (2.10)

Energy content in the sample before pyrolysis

The energy content is the product of the sample weight and the heating value of the sample. The energy content in the sample before pyrolysis is the input energy of the processes, while the energy content to the products (which includes the energy of the processes, while the energy content to the products (which includes the energy content in the char, tar and that of the gas) is the output energy of process, also the energy produced by the furnace is the input energy of the equipment.

Energy content in the sample before pyrolysis

The energy content is the product of the sample weight and the heating value of the sample. The weight of the sample (palm kernel shells), W_{pks} was determined as given above and the heating value of palm kernel shell H_{pks} was given as 21.10MJ/kg by Ojolo, and Ismail, (2012). Therefore, the energy content in the sample is given in the relation:

$$\epsilon pks = W_{pks} \times H_{pks} \quad (3.11)$$

However, a constant weight of 500g was used throughout the experiment and since the heating value of palm kernel shells has been known to be 21.1 MJ/kg.

Hence, the energy content in the shell is

$$\epsilon pks = \frac{500g}{1000} \times 21.1 \text{ MJ/kg} = 10.55 \text{ MJ} \quad (3.12)$$

3. EXPERIMENTAL PROCEDURE

The major pyrolysis components used in the pyrolysis of palm kernel shells biomass to fuel (char, tar and gas) are discussed below:

3.1 The Pyrolyzer

A pyrolyzer is a device used in converting biomass into useful fuels in the absence of oxygen. The components of the Pyrolyzer are: electrically operated furnace, heater band, clay, retort, pyrometer, contactor, galvanized iron pipe, rubber hose, rubber gasket, clips, thermostat, heating element, bolts and nuts, lagging.

Plate I: Pyrolysis furnace

4. RESULTS AND DISCUSSION

a. Pyrolysis of palm kernel shells

The result of the pyrolysis of palm kernel shells at a temperature range of 300 °C to 700 °C for 20 minutes is presented in table 2 below

Table 4.1: Result of the pyrolysis of palm kernel shells.

Temperature (°C)	Initial Weight (g)	Char Weight (g)	Tar Weight (g)	Gas Weight (g)
300	500	356.95	103.47	39.58
400	500	220.22	130.61	149.17
500	500	210.55	186.47	103.03
600	500	168.58	250.73	130.69
700	500	149.40	165.20	185.40

The result presented in the Table 4.1 above shows that a temperature of 300°C, there was a mixture of char and unpyrolysed shells, some amount of tar and very little gas, because it is still very low to generate more gas but as the temperature increased, there was increase in tar production and gas weight while the weight of char reduced. This means that the sample gets more pyrolyzed as the temperature increases for a constant time consideration.

4.2 **Cost Estimation of Constructing the Electric Furnace and its accessories**

The cost for the design and fabrication of the electrical furnace and its accessories are shown in the table 4.2

Table 4.2: Bill of engineering measurement and evaluation.

S/N	Component	Unit Price	Quantity	Price (₦)
1.	Cabinet with lagging materials	₦60,000	-	₦60,000
2.	Retort with double pipe	₦15,000	2	₦15,000
3.	Temperature control (range 0°c-1300°c)	₦15,000	1	₦15,000
4.	Heating element	₦25,000	1	₦25,000
5.	Thermocouple	₦3,000	1	₦3,000
6.	Wire, switch, connector	₦3,000	-	₦3000
7.	Contactor (40amps)	₦5000	1	₦5000
			Grand total	₦126,000

5. CONCLUSION

In this study, the pyrolytic conversion of palm kernel shells biomass to fuel has been carried out successfully. A lot of studies have been undertaken regarding the pyrolysis of biomass to fuel. The pyrolysis furnace assembly has been shown to be capable of converting agro biomass residue like palm kernel shells (PKS) to fuel (char, tar, and gas). This was accomplished by an electrically operated compact, fixed bed pyrolysis furnace.

The (40.5 × 40.5 × 38) cm^3 pyrolysis furnace with its 2500 watts (3MJ) electric heating element with retort diameter 16.1 cm and volume 3.56 litres which was expected to pyrolyse 500g of biomass, have been able to pyrolyse palm kernel shells (PKS) between temperature ranging from 300°C to 700°C for a constant temperature of 20 minutes, giving three types of fuels the solid (char), the liquid (tar), and the gaseous fuel. At pyrolysing temperature of 300°C a mixture of char and unpyrolysed shell are observed in the retort with some amount of tar and very little gas but as the temperature increases, there is increase in tar produced and gas weight while the weight of char reduces which means that the sample gets more pyrolysed as the temperature increased for a constant time consideration.

The efficiency of the process is calculated as 88.11%, and with energy content in the palm kernel shells (ϵ_{pks}) before pyrolysis calculated as 10.55MJ and total energy content (ϵ_T) in the product (which comprises the char, tar and gas) was calculated as 9.296MJ. Which authenticate that the conversion process is good and there was no much/leakage during the process of pyrolysis. The efficiency of the equipment is calculated as 68.67% which can be concluded that the equipment is good for the pyrolysis process.

5.1 Recommendations

The following recommendation are made;

(i) cement should not be used in the casting of the clay lagging material used for the furnace.
(ii) the gas cylinder should be placed at a lower datum level to be the gas collection unit so as to increase the pressure in the cylinder.
(iii) the gas collection unit should be increased in order to retain a large volume.

ACKNOWLEDGEMENT

My sincere gratitude goes to my project supervisor Engr. Dr. I. Bori, for his support and continuous guidance all through this project work. Also, my profound gratitude goes to the Renewable energy laboratory, LAUTECH, Ogbomoso for giving me the opportunity of fabricating the electric furnace (pyrolyser) within its centre.

REFERENCES

Ciubota-Rosie, C., Gavrilescu, M., & Macoveanu, M. (2008). Biomass - An important renewable source of energy in Romania. *Environmental Engineering and Management Journal*, *7*(5), 559–568. https://doi.org/10.30638/eemj.2008.079

Jahirul, M. I., Rasul, M. G., Chowdhury, A. A., & Ashwath, N. (2012). Biofuels production through biomass pyrolysis- A technological review. *Energies*, *5*(12), 4952–5001. https://doi.org/10.3390/en5124952

Jain, S., & Ph, D. (2015). *ENVIRONMENT IMPACTS OF ENERGY SECTOR (NON-RENEWABLE) Non-renewable energy sources*.

Kamimoto, M. (2006). The significance of liquid fuel production from woody biomass. *AIST Today (International Edition)*, *21*, 2–3.

Mafu, L. D. (2018). *Chemical and structural changes of biomass during pyrolysis and the influence on gasification reactivity in coal -biomass blends*. *October*, 11–46.

National Energy Education Development. (2008). Biomass Biomass at a Glance 2008. *The NEED Project*, 12–15.

Ojolo, S. J, Ismail, S.O, (2012). "Mathematical modelling of plastic waste pyrolysis kinematics"

Mechanical Engineering Department, University of Lagos, Lagos, Nigeria.

Okoroigwe, E. C., Enibe, S. O., & Onyegegbu, S. O. (2016). Determination of oxidation characteristics and decomposition kinetics of some Nigerian biomass. In *Journal of Energy in Southern Africa* • (Vol. 27, Issue 3).

Osueke, C., & Ezugwu, C. (2011). Study of Nigeria Energy resources and its consumption. *International Journal of Scientific & Engineering Research*, *2*(12), 121–130.

Oyedepo, S. O., Dunmade, I. S., Adekeye, T., Attabo, A. A., Olawole, O. C., Babalola, P. O., Oyebanji, J. A., Udo, M. O., Kilanko, O., & Leramo, R. O. (2019). Bioenergy technology development in Nigeria – Pathway to sustainable energy development. *International Journal of Environment and Sustainable Development*, *18*(2), 175–205. https://doi.org/10.1504/IJESD.2019.099513

Philander, S. G., & Winograd, C. (2012). International Energy Agency. In *Encyclopedia of Global Warming & Climate Change*. https://doi.org/10.4135/9781452218564.n379

Vigouroux, R. Z. (2001). *PYROLYSIS OF BIOMASS • Rapid Pyrolysis at High Temperature • Slow Pyrolysis for Active Carbon Preparation*. 113.